THE UNIVERSITY OF
WARWICK

Library Declaration and Deposit Agreement

1. **STUDENT DETAILS**

Full name: **Sepehr Vasheghani Farahani**.....

University ID number: **0859043**.....

2. **THESIS DEPOSIT**

2.1 I understand that under my registration at the University, I am required to deposit my thesis with the University in BOTH hard copy and in digital format. The digital version should normally be saved as a single pdf file.

2.2 The hard copy will be housed in the University Library. The digital version will be deposited in the University's Institutional Repository (WRAP). Unless otherwise indicated (see 2.3 below) this will be made openly accessible on the Internet and will be supplied to the British Library to be made available online via its Electronic Theses Online Service (EThOS) service. [At present, theses submitted for a Masters degree by Research (MA, MSc, LLM, MS or MMedSci) are not being deposited in WRAP and not being made available via EThOS. This may change in future.]

2.3 In exceptional circumstances, the Chair of the Board of Graduate Studies may grant permission for an embargo to be placed on public access to the hard copy thesis for a limited period. It is also possible to apply separately for an embargo on the digital version. (Further information is available in the Guide to Examinations for Higher Degrees by Research.)

2.4 *If you are depositing a thesis for a Masters degree by Research, please complete section (a) below. For all other research degrees, please complete both sections (a) and (b) below:*

(a) Hard Copy

I hereby deposit a hard copy of my thesis in the University Library to be made publicly available to readers (please delete as appropriate) EITHER immediately OR after an embargo period of ..... months/years as agreed by the Chair of the Board of Graduate Studies

I agree that my thesis may be photocopied. YES / NO (*Please delete as appropriate*)

(b) Digital Copy

I hereby deposit a digital copy of my thesis to be held in WRAP and made available via EThOS

Please choose one of the following options:

EITHER My thesis can be made publicly available online. YES / NO (*Please delete as appropriate*)

OR My thesis can be made publicly available only after..[date] (Please give date)
YES / NO (*Please delete as appropriate*)

OR My full thesis cannot be made publicly available online but I am submitting a separately identified additional, abridged version that can be made available online.
YES / NO (*Please delete as appropriate*)

OR My thesis cannot be made publicly available online. YES / NO (*Please delete as appropriate*)

3 **GRANTING OF NON-EXCLUSIVE RIGHTS**

Whether I deposit my Work personally or through an assistant or other agent, I agree to the following:

Rights granted to the University of Warwick and the British Library and the user of the thesis through this agreement are non-exclusive. I retain all rights in the thesis in its present version or future versions. I agree that the institutional repository administrators and the British Library or their agents may, without changing content, digitise and migrate the thesis to any medium or format for the purpose of future preservation and accessibility.

4 **DECLARATIONS**

(a) I DECLARE THAT:

- I am the author and owner of the copyright in the thesis and/or I have the authority of the authors and owners of the copyright in the thesis to make this agreement. Reproduction of any part of this thesis for teaching or in academic or other forms of publication is subject to the normal limitations on the use of copyrighted materials and to the proper and full acknowledgement of its source.
- The digital version of the thesis I am supplying is the same version as the final, hard-bound copy submitted in completion of my degree, once any minor corrections have been completed.
- I have exercised reasonable care to ensure that the thesis is original, and does not to the best of my knowledge break any UK law or other Intellectual Property Right, or contain any confidential material.
- I understand that, through the medium of the Internet, files will be available to automated agents, and may be searched and copied by, for example, text mining and plagiarism detection software.

(b) IF I HAVE AGREED (in Section 2 above) TO MAKE MY THESIS PUBLICLY AVAILABLE DIGITALLY, I ALSO DECLARE THAT:

- I grant the University of Warwick and the British Library a licence to make available on the Internet the thesis in digitised format through the Institutional Repository and through the British Library via the EThOS service.
- If my thesis does include any substantial subsidiary material owned by third-party copyright holders, I have sought and obtained permission to include it in any version of my thesis available in digital format and that this permission encompasses the rights that I have granted to the University of Warwick and to the British Library.

5 **LEGAL INFRINGEMENTS**

I understand that neither the University of Warwick nor the British Library have any obligation to take legal action on behalf of myself, or other rights holders, in the event of infringement of intellectual property rights, breach of contract or of any other right, in the thesis.

Please sign this agreement and return it to the Grade School Office when you submit your thesis.

Student's signature:..... Date:.....

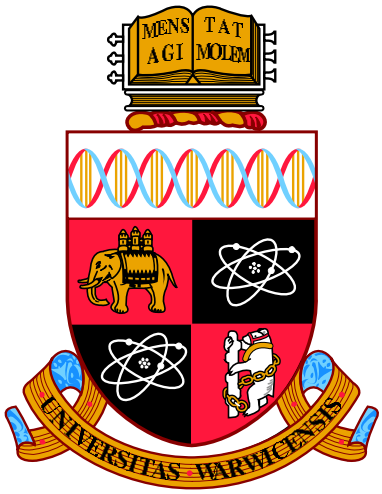

Optical and Electronic Properties of Defects and Dopants in Oxide Semiconductors

by

Sepehr Vasheghani Farahani

Thesis

Submitted to the University of Warwick

for the degree of

Doctor of Philosophy

Department of Physics

May 2013

THE UNIVERSITY OF WARWICK

Contents

Acknowledgements

I would first like to thank my supervisor Professor Chris McConville, for welcoming me into his group at the University of Warwick, for his encouragement and advice and helping me in the understanding of oxide semiconductors. I was fortunate enough to work with Dr Tim Veal. I am extremely grateful to Tim for his considered guidance, friendship, and invaluable views (not only in science). I would like to thank Dr Phil King for his great help at the start of my PhD. I am very grateful to Rob Johnston for his great technical help and immense technical expertise. Dr Sem Gorfman and Dr Ana Sanchez are acknowledged for XRD and TEM measurements.

Members of the Surface Physics group, a diverse and interesting group of people, many of whom I count as good friends, are thanked for miscellaneous assistance, advice and friendship. Drs. Jim Aldous, Chris Burrows, and Wojciech Linhart are particularly thanked for instructive discussions on the strange aspects of the English language as well as physics!

I would especially like to thank my parents and my brothers for the varied and extensive support and encouragement; I will forever be thankful.

Declarations

I declare that this thesis contains an account of my research work carried out at the Department of Physics, University of Warwick between March 2009 and May 2013 under the supervision of Prof. C. F. McConville. The research reported here has not been previously submitted, wholly or in part, at this or any other academic institution for admission to a higher degree.

The CdO samples were grown by Professor Vicente Muñoz-Sanjosé using MOVPE at the University of Valencia, Spain, while all of the SnO_2 samples were grown in Professor Jim Speck's group at the University of California, Santa Barbara, USA using PAMBE. Dr. Sem Gorfman is thanked for assistance with the XRD measurements presented in this thesis and Dr. Ana Sanchez produced the TEM images presented in chapter 6.

Sepehr Vasheghani Farahani

May 2013

Several articles based on this research have been published, are in press, or have been submitted for publication:

S. K. Vasheghani Farahani, T. D. Veal, P. D. C. King, J. Zúñiga-Pérez, V. Muñoz-Sanjosé, and C. F. McConville, *Electron mobility in CdO films*, J. Appl. Phys. **109**, 073712 (2011)

S. K. Vasheghani Farahani, T. D. Veal, A. M. Sanchez, O. Bierwagen, M. E. White, S. Gorfman, P. A. Thomas, J. S. Speck, and C. F. McConville, *Influence of charged-dislocation density variations on carrier mobility in heteroepitaxial semiconductors: The case of SnO2 on sapphire*, Phys. Rev. B **86**, 245315 (2012)

S. K. Vasheghani Farahani, V. Muñoz-Sanjosé, J. Zúñiga-Pérez, C. F. McConville, and T. D. Veal, *Temperature dependence of the direct bandgap and transport properties of CdO*, Appl. Phys. Lett. **102**, 022102 (2013)

S. K. Vasheghani Farahani, C. F. McConville, T. D. Veal, and A. Schleife, *Impact of degenerate n-doping on the optical absorption edge in transparent conducting cadmium oxide*, Proc. SPIE (invited paper) **8626**, 862604 (2013)

S. K. Vasheghani Farahani, T. D. Veal, O. Bierwagen, M. E. White, J. S. Speck, and C. F. McConville, *Surface electronic properties of single crystal SnO_2 grown by PAMBE* (in preparation)

The work presented in this thesis has been presented at the following national and international conferences.

Temperature Dependence of the Direct Band Gap and Transport Properties of CdO (oral presentation),
Materials Research Society (MRS), Fall Meeting, Boston, MA, USA (November 2012).

Electron Transport Properties of High-Quality MBE-Grown SnO2 (oral presentation), 39th conference on the Physics and Chemistry of Surfaces and Interfaces, Santa Fe, NM, USA (January 2012).

Surface Electron Accumulation and Bulk Transport Properties of MBE-Grown SnO2 Films (oral presentation), Materials Research Society (MRS), Fall Meeting, Boston, MA, USA (November 2011).

Optoelectronic Properties of epitaxial CdO (poster presentation), Photonex, The Enlighten Meeting, Coventry, UK (October 2011).

Surface and Bulk Properties of Post-Transition Metal-Oxide Semiconductors (oral presentation), DPG Meeting, Dresden, Germany (March 2011).

Optical Properties and Carrier Transport of CdO (poster presentation), Materials Research Society (MRS), Fall Meeting, Boston, MA, USA (November 2010).

Abstract

Interest in semiconductor materials has continually grown over the past 60 years due to their potential use in electronic and optoelectronic device structures. Oxide semiconductors are a particular class of materials that also combine conductivity with optical transparency, properties not usually found in the same material. These transparent conducting oxides (TCOs) have been among the first oxide materials to benefit from the availability of improved epitaxial growth techniques, although perovskite oxides and heterostructures have also proved to be opening a new era of high mobility structures based on oxide materials.

Optical and electronic properties of binary oxides, specifically, high quality CdO and SnO_2 epitaxial films have been investigated in this thesis. The main band structure quantities, the band gap and band edge effective mass of CdO has long been a subject of controversy due to the degeneracy of this material. The lowest carrier concentration for an as-grown CdO film is 1-2$\times 10^{19}$ cm^{-3}. This brings about further difficulties in determining the optoelectronic properties due to conduction band filling and many body effects. The effective mass value is of particular importance in carrier mobility studies. Simulation and analysis of data collected from Hall effect, mid- and near-infrared reflectance measurements together with optical absorption spectroscopy enabled the band gap and band edge effective mass values to be determined at room temperature. Variations of the band gap, band edge effective mass, high frequency dielectric constant and the Fermi level with temperature and carrier concentration, and taking into account the non-parabolicity of the conduction band, the Burstein-Moss shift and band gap renormalization, revealed the 0 K band gap and band edge effective mass values of 2.31 eV and $0.266m_0$ at the limit of zero carrier concentration in CdO.

With the emergence of sophisticated growth techniques (MBE), high quality growth has become a key property in semiconductor research as it enables further investigation into the intrinsic characteristics of these materials. Carrier mobilities in high quality SnO_2(101) films grown on *r*-plane sapphire by molecular beam epitaxy were studied. Transmission electron microscopy revealed a high density of dislocations at the interface due to the large lattice mismatch of -11.3%, along the $< 101 >$ direction, between the films and the substrate, with an exponential decrease towards the surface of the films. Carrier mobility modelling proved to be impossible if a constant density of threading dislocations was assumed, however, by introducing a layer-by-layer model for the simulation of the mobility as a function of carrier concentration, the donor nature of dislocations in epitaxial SnO_2 films was revealed. The deformation potential produced by the presence of these defects has been shown to be the dominant scattering mechanism for carrier concentrations above the Mott transition level of SnO_2.

Finally, the surface electronic structure of antimony-doped SnO_2 films has been studied by the Hall effect, infrared reflectance, X-ray photoemission spectroscopy and electrochemical capacitance-voltage measurements. The bulk Fermi level was determined by carrier statistics calculations and used to obtain the degree of surface band bending. Modelling the surface energy bands through the capacitance-voltage spectra, revealed that SnO_2 has downward band bending and surface electron accumulation. The respective variations were attained as a function of depth and composition of the samples.

Abbreviations and common symbols

ADP	Acoustic deformation potential
AFM	Atomic force microscopy
AP	Acoustic piezoelectric
ARE	Activated reactive evaporation
CB	Conduction band
CBM	Conduction band minimum
CNL	Charge neutrality level
CTO	Cadmium stannate
DCRMS	DC reactive magnetron sputtering
DDP	Dislocation deformation potential
DFT	Density functional theory
deg	Degenerate
ECV	Electrochemical capacitance-voltage
FB	Flat-band
FTIR	Fourier-transform infrared
FWHM	Full width at half maximum
HRXRD	High resolution X-ray diffraction
HSE	Heyd, Scuzeria, and Ernzerhof
IBS	Ion-beam sputtering
ID	Ionised defect
IMFP	Inelastic mean free path
IR	Infrared
ITO	Indium tin oxide
LDA	Local density approximation
LPO	Longitudinal polar-optical
LPP	Longitudinal optical phonon-plasmon
MOCVD	Metal-organic chemical vapor deposition
MOVPE	Metal-organic vapor-phase epitaxy

MTFA	Modified Thomas-Fermi approximation
NI	Neutral impurity
non-deg	Non-degenerate
PAMBE	Plasma-assisted moleacular beam epitaxy
PET	Polyethylene terephthalate
PLD	Pulsed laser deposition
RS	Reactive sputtering
RT	Room temperature
SG	Sol-gel
SGDC	Sol-gel dip coating
SIMS	Secondary ion mass spectrometry
SP	Spray pyrolysis
TFET	Transparent field-effect transistor
TMM	Transfer matrix method
UHV	Ultra-high vacuum
UiD	Unintentionally-doped
UV	Ultraviolet
VB	Valence band
VBM	Valence band maximum
XPS	X-ray photoemission spectroscopy

α	Absorption coefficient
α_{LO}	Polaron coupling constant
$\boldsymbol{B}$	Magnetic field
C	Capacitance
Δ_{so}	Spin-orbit splitting
δ	Kronecker delta function
$\boldsymbol{E}$	Electric field
E	Energy
E_{c}	Acoustic deformation potential
E_{D}	Dislocation deformation potential

E_{F}	Fermi level
E_f	Final state energy
E_{g}	Band gap
E_i	Initial state energy
E_{k}	Kinetic energy
E_P	Energy parameter of the momentum matrix element
E_{p}	Plasmon energy
E_p	Valence band eigenvalues
E_s	Conduction band eigenvalues
e	Electronic charge
eV	Electron volts (1.602×10^{-19} J)
ϵ_0	Permittivity of vacuum
$\epsilon(0)$	Static dielectric constant
$\epsilon(\infty)$	High frequency dielectric constant
f_{FD}	Fermi-Dirac distribution function
$\boldsymbol{G}$	Reciprocal lattice vector
$g(E)$	Density of states
Γ	Centre of the Brillouin zone
γ_{LO}	Longitudinal optical phonon damping
γ_{TO}	Transverse optical phonon damping
H	Hamiltonian
$\hbar$	$h/2\pi$
K	Dimensionless piezoelectric coupling coefficient
K_{B}	Boltzmann constant
$\boldsymbol{k}$	Wave vector
k	Angular Wave number
l	Intra-grain mean free path of electrons
M_{if}	Transition amplitude of perturbation
m_0	Free electron mass
m^*	Effective mass

m_0^*	Band edge effective mass
m_p	Polaron effective mass
n	Electron concentration
n'	Refractive index
n_ss	Surface sheet density
N_A^-	Ionised acceptor density
N_D^+	Ionised donor density
N_dis	Density of dislocations
N_i	Density of ionised defects
N_NI	Density of neutral impurities
Ω	Transition probability
ω_p	Plasma frequency
ω_LO	Longitudinal optical phonon frequency
ω_TO	Transverse optical phonon frequency
ψ, Φ, ϕ_x	Wave function
ϕ	Work function
P	Momentum matrix element
$\boldsymbol{p}$	Particle momentum
ρ	Density
$\boldsymbol{R}$, $\boldsymbol{r}$	Position vectors
T	Temperature
T_{if}	Transition rate
τ	Plasmon lifetime
V	Potential
V_BE	Binding energy
V_bb	Band bending
v_s	Velocity of sound
ν	Frequency
μ	Mobility
Z	Charge state

Chapter 1

Introduction

1.1 Overview

Most wide band gap materials are, by nature, insulating materials, while conducting materials such as metals tend to be opaque or very reflective. Oxide semiconductors are a class of materials that have shown concurrent transparency and conductivity, two often mutually exclusive properties, and as a result have found enormous device applications. Collectively, these materials are known as transparent conducting oxides or TCOs. Their properties include: enhancing the output optical power of light-emitting diodes [1,2]; enabling light to pass through as a back contact to an active layer in order to produce charge carriers with short carrier diffusion lengths in solar cells [3]; transparent contacts to LCD displays [4]; an anti-reflection window on the front surface of a silicon solar cell [5,6]; thermal mirrors to confine the heat within a closed space or in a solar collector [7–9]; functionalizing freestanding graphene [10]; conductance-type gas sensors [11,12], to name but a few applications. As an example, a number of TCO semiconductors have been used as contacts in CdTe solar cell, including, tin oxide (SnO_2) and indium tin oxide (ITO) [13, 14], Al-doped ZnO (AZO) [15], fluorine-doped SnO_2, and cadmium stannate [Cd_2SnO_4 (CTO)] [14].

CdO was among the first examples of a transparent conducting oxide when it was grown by the thermal oxidation of sputtered cadmium, a process which dates back to 1907 [16]. Over the past 50 years, there have been numerous efforts to grow high quality TCOs using chemical vapour deposition (CVD), molecular beam epitaxy (MBE), and pulsed laser deposition (PLD). Such sophisticated growth techniques enable a deeper understanding of the material and the intrinsic electronic and optical properties by improving the stoichiometry, the composition and reducing defect densities and impurities and unwanted dopants. However, post-growth

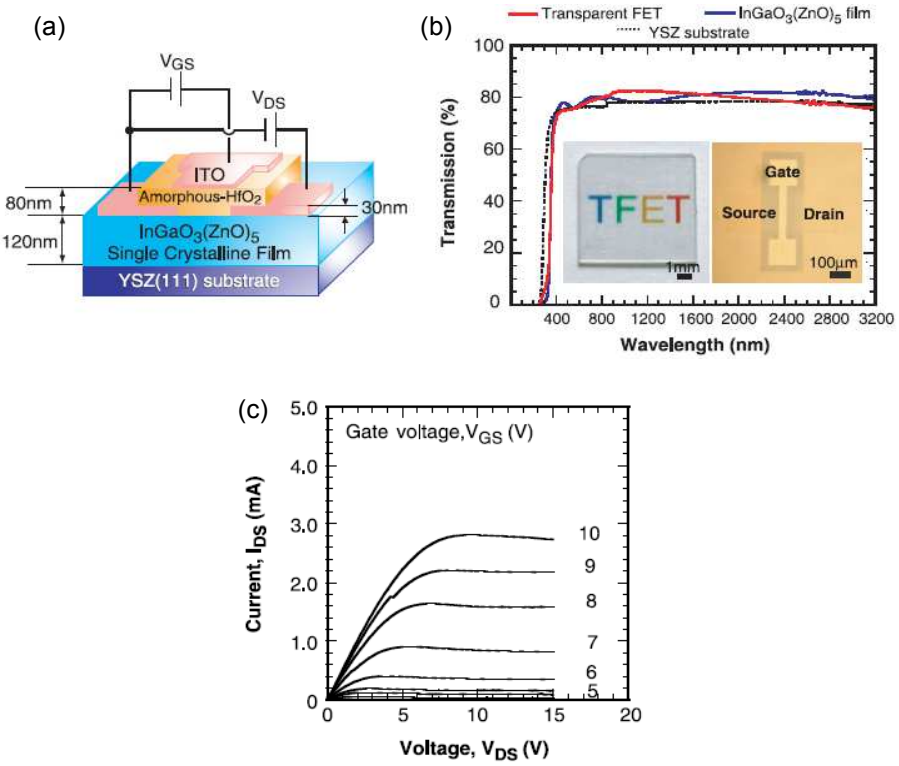

Figure 1.1: (a) Schematic representation of TFET structure with an ITO as the source, drain, and gate electrodes, and $InGaO_3(ZnO)_5$ as the channel layer; (b) the optical transmission spectra; and (c) the output $I-V$ characteristics of the TFET [18].

doping has in many respects been a necessity in many TCO and other semiconductor applications as a means to balance the level of conductivity and transparency or to achieve a single type of charged carrier with the required concentration.

As it is now apparent that silicon-based electronic devices are approaching their physical and electronic limits [17], there is a promise that TCOs may offer an alternative in a future generation of semiconductor electronic and optical devices [18–21]. Figure 1.1 shows how a single crystalline $InGaO_3(ZnO)_5$ film can be used as an oxide channel in a transparent field-effect transistor (TFET) with a high field-effect mobility. A growing motivation and demand for the fabrication of high quality TCO heterostructures arise from the fact that novel TCO applications require high crystallinity and minimum defect levels at their interfaces to achieve high performance devices [19], e.g. the observation of quantum Hall effect [22–24].

Oxides have also been shown to feature extremely high mobilities when combined to form heterostructures. Ohtomo and Hwang [25] demonstrated that the

interface of lanthanum aluminate ($LaAlO_3$) grown on strontium titanate ($SrTiO_3$) by PLD, forms a conducting 2D electron gas at the interface with an extremely high mobility exceeding 10,000 $cm^2V^{-1}s^{-1}$ in spite of the fact that both materials are individually band insulators. The functionality of the interface again depends on the precise crystallinity of the structures. This is because the internal electric field responsible for the creation of the interfacial electron gas can only drive the electrons to the junction when the appropriate atomic layers come into contact.

1.2 Defects in oxides

In oxide semiconductors where there is a large size mismatch between the anions and cations, oxygen vacancies have long been thought to be the major source of charge carriers as a point defect [26]. Recent improvements in growth techniques together with theoretical calculations within the frame work of density functional theory (DFT), have updated the insight into the sources of conductivity in oxide semiconductors. However, in spite of the DFT calculations providing valuable information about the formation energies of defects, the methodology still has its limitations. The calculations are performed at absolute zero, whereas high quality growth of oxide materials are carried out above room temperature. On the other hand, although many methods have been invoked to minimise the issue, the underestimation of the band gap in these materials due to the valence band *p-d* orbital repulsion still exists which introduces errors in comparison with experimental results [27–29].

Studies of the effect of hydrogen on the electronic properties of semiconductors date back to the 1950's. Hydrogen is a ubiquitous element and can be present under all growth conditions. Mollwo [30] observed that hydrogen would act as a reduction agent on the surface of ZnO causing Zn to diffuse into the bulk and act as an interstitial donor when ZnO crystals were annealed in H_2, while Thomas and Lander [31] showed that it is hydrogen which diffuses into the crystal and donates electrons. It was also believed that interstitial hydrogen counteracts the majority carriers and adopts an amphoteric behaviour, namely, featuring as a donor (H^+) in

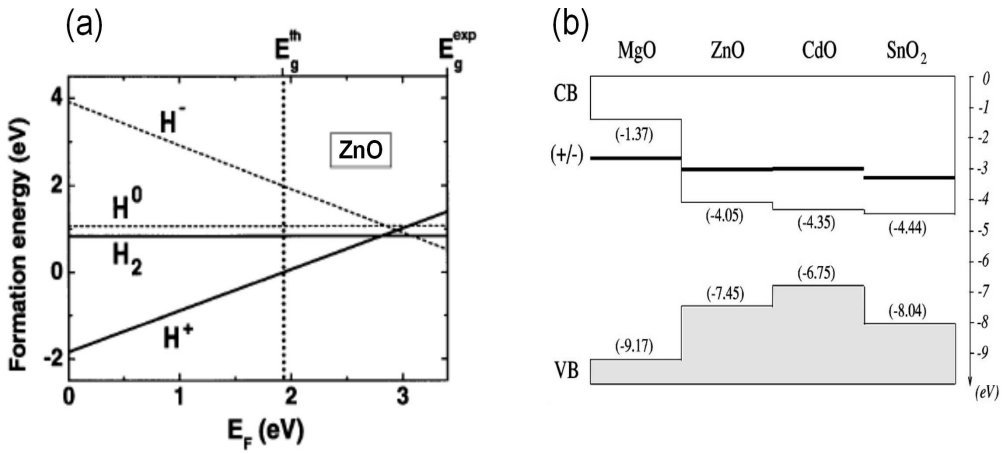

Figure 1.2: DFT calculation of (a) the formation energies of interstitial hydrogen as a function of the Fermi level position for ZnO (dashed lines are underestimated energies in the LDA calculations) [34], and (b) the position of the hydrogen transition level, H(+/−), for MgO, ZnO, CdO, and SnO_2 [36]. It is apparent that H(+/−) is located above the calculated conduction band minima for ZnO, CdO, and SnO_2, indicating that H is a source of donors in n-type semiconductors. (a) shows that H^+ has the lowest formation energy for Fermi level positions lower towards the valence band maximum suggestive of the same behaviour for p-type semiconductors.

p-type, and an acceptor (H^-) in n-type materials [32]. This could be understood in GaAs as a conventional semiconductor where it has been shown that H(+/−), the H charge-transition formation energy level, lies near the mid-band gap which indicates that for p-type conductivity (n-type conductivity), where the Fermi level is in the vicinity of the valence (conduction) band, H acts as compensating donor (acceptor) [33].

DFT calculations on ZnO show that the stable charge state of hydrogen is H^+ for all Fermi level positions in the entire band gap and therefore, always acts as a source of donors [34,35] [see Fig. 1.2(a)]. This opened the possibility of a similar behaviour in other oxide semiconductors. Fig. 1.2 compares the formation energy of H incorporated in some oxide materials with respect to its charge state. In Fig. 1.2(b), the position of H(+/−), the energy level where the formation energies of H^+ and H^- are equal, indicates that H is a shallow donor in ZnO, CdO, and SnO_2, but a deep donor in MgO. These results were substantiated by muon implantation in the muon spin rotation (μSR) technique [37,38] and electron-nuclear resonance and Hall measurements on nominally undoped n-type ZnO [39]. Furthermore, infrared

spectroscopy shed light on the microscopic structure involving H by the local vibrational modes of O-H bonds in defect complexes [40–43]. Interstitial H donors were later discovered in SnO_2 by a combined infrared spectroscopy on O-H vibrational modes and first principle DFT calculations [44] suggesting similar H behaviour in a range of transparent oxides. Van de Walle and Neugebauer [45] presented a generic band line up model against the H(+/−) with respect to the vacuum level for different compounds in which the donor and acceptor nature of H can be compared. With the decrease in the energy of the conduction band minimum (CBM) relative to the vacuum level, the H(+/−) level moves up and into the CB indicative of the occurence of H^+ state for even higher Fermi levels.

Other defects such as oxygen vacancies and cation interstitials as well as impurities become energetically comparable to H, depending on the material or anion-rich and cation-rich growth conditions, in respect of the Fermi level positions [46, 47]. As high quality semiconducting films are grown on a substrate, the lattice mismatch between them is another source of defects in semiconductors. Threading dislocations and planar defects are formed at the interface and extend throughout the film. These type of defects similar to point defects may or may not be charged, but they have one thing in common: they are carrier scattering centres.

1.3 Scattering theory

The response of free carriers to an external electric field depends on the strength of the field. When a weak electric field is applied, the behaviour of carriers follows Ohm's law, hence linear transport, and the scattering process can be described by an external pertubation in the one-particle Hamiltonian, provided that the deviation from the perfect crystalline potential is also small or infrequent. In the case of strong electric fields, the rate at which carriers gain energy from the external field is higher than the rate of energy loss to the lattice. Hence, the carriers are not at thermal equilibrium with the lattice. If the carriers are in thermal equilibrium within themselves and not with the lattice (phonons), the carriers are said to be in quasi thermal equilibrium. Although their distribution can still be described by

the Fermi-Dirac function, their temperature or average kinetic energy is higher than that of the lattice and are therefore called hot carriers. All scattering mechanisms in this work are based on linear transport.

Carrier transport is governed by the variation of the distribution function, $f_{\boldsymbol{k}}$, in the presence of an external pertubation by the Boltzmann equation:

$$\frac{df_{\boldsymbol{k}}}{dt} = \left(\frac{\partial f_{\boldsymbol{k}}}{\partial t}\right)_{\text{field}} + \left(\frac{\partial f_{\boldsymbol{k}}}{\partial t}\right)_{\text{diffusion}} + \left(\frac{\partial f_{\boldsymbol{k}}}{\partial t}\right)_{\text{scattering}}. \tag{1.1}$$

When a weak field is applied, $f_{\boldsymbol{k}}$ can be expanded about the no-field distribution function (the Fermi-Dirac statistics) which could be approximated by the Boltzmann statistics for non-degenerate semiconductors. Within the relaxation time approximation, the expansion function can be related to the scattering term on the right hand side of Eq. 1.1 through a quantity called the relaxation time. The relaxation time is energy dependent and is used to evaluate the strength of different scattering mechanisms.

A number of important scattering mechanisms in semiconducting materials are classified in Fig. 1.3. All scattering effects arise from the perturbation produced by the introduction of defects/impurities and phonon propagation in the crystal structure. Ionized defects/impurities introduce energy levels in the band gap which are occupied (empty) for donors (acceptors) at very low temperatures. Therefore, at low temperatures, the carriers collide with neutral defects or impurities. As the temperature increases, they become ionized and the respective scattering becomes significant. However, generally, as the charged centres are incapable of scattering high energy electrons, by further increase in temperature, the effect of this type of scattering decreases.

Lattice vibrations are intrinsic to any type of material at high enough temperatures. The vibrations perturb the periodic crystal potential disturbing the motion of the carriers. Lattice vibrations are divided into acoustic and optical phonons. Acoustic phonons affect the carriers by the induced deformation potential and/or the piezoelectric effect. The potential produced due to the variation of the electronic stucture, e.g. CBM and valence band maximum (VBM), from point to point as a

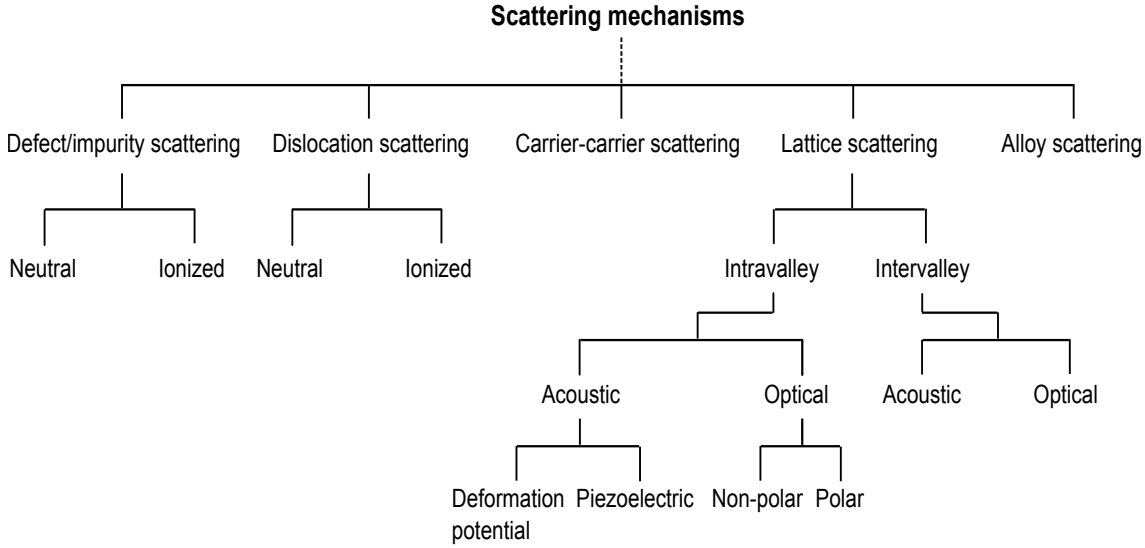

Figure 1.3: The classification of different scattering mechanisms in semiconductors based on Ref. [48].

result of the crystal deformation is called the deformation potential. The shift in the electronic states, $E_{n\boldsymbol{k}}$ is a measure of this potential and is proportional to the strain generated by the vibrations; the associated scattering mechanism is referred to as the *acoustic deformation potential scattering*. On the other hand, in non-centrosymmetric crystals where the atoms are partially ionized (e.g. in ionic crystals), their displacement due to acoustic vibrations induces a macroscopic electric polarization field. This phenomenon is called the piezoelectric effect; the associated scattering mechanism is referred to as the *acoustic piezoelectric scattering*. This type of scattering becomes more significant in crystals with lower symmetry.

Optical phonons can also change the energy bands through two different mechanisms quite similar to the acoustic phonons. In non-polar crystals, the propagation of an optical phonon changes the electronic structure by changing the bond lengths and/or bond angles introducing a deformation potential. The respective scattering mechanism is the *optical-phonon deformation potential scattering*. This mechanism is also dependent on the symmetry of the crystal and the band structure, consequently, the interaction is very weak for electrons at the Γ-point minima [49]. As in the acoustic vibrations, the deformation potential induced by the optical vibrations is proportional to the optical strain. The optical phonons involve the vibration of the neighbouring oppositely charged atoms against each other within the

compound. Such relative displacement results in a dipole moment which produces a macroscopic electric field. The carrier scattering arising from this phenomenon, which is similar to the piezoelectric field of the acoustic phonons, is the *polar-optical phonon scattering* which is often one of the most important scattering mechanisms above liquid nitrogen temperature. The electron-longitudinal polar-optical interaction is also called the Fröhlich interaction [50].

Many carrier transitions in semiconductors are phonon assisted. The conservation of energy and momentum gives rise to carrier transitions either within the same valley (*intravalley scattering*) or between different valleys (*intervalley scattering*). Zone-centre phonons having low wave vectors only take part in intravalley scattering in which the carriers remain in the same valley in E–$\boldsymbol{k}$ space. A zone-edge or near zone-edge phonon which possesses higher wave vectors can scatter electrons from the Γ-point (a band minimum) to a band minimum near or at the zone edge [51]. Intervalley scattering mediates the indirect optical transitions especially in indirect band gap semiconductors. However, zone-centre and zone-edge phonons interact somewhat differently with electrons. As the longitudinal component of the electric field produced by the acoustic and optical phonons is inversely proportional to the their wave vectors, zone-edge phonons cannot produce long-range electric fields. Hence, they do not involve Fröhlich or piezoelectric interactions [51]. The energy difference between the zone-edge acoustic and optical phonons is small as opposed to zone-centre phonons where the longitudinal phonons inflict larger deformation on the crystal lattice.

In semiconducting alloys, namely, alloys of different semiconducting compounds, a distortion in the band structure occurs where different compositions come into contact. The discontinuities in the electronic structure are basically similar to those generated by the acoustic phonons. Each of the hetero-boundary regions become scattering centres and the phenomenon is called *alloy scattering*.

Another type of scattering which mostly arises in heterostructures is *dislocation* or *grain boundary scattering*. As it has been shown that dislocations are either negatively or positively charged in some semiconductors [52–55], they possess a dual

scattering mechanism similar to ionized defect/impurity scattering, the scattering due to the deformation potential induced by their presence in the crystal lattice, and the scattering by the electric field generated by their charged nature. In cases where charged scattering centres are encountered, the electrical screening needs to be considered especially at higher carrier concentrations. At higher carrier concentrations, the carriers are more influenced by the Coulomb fields of other electrons. This is the *carrier-carrier scattering* and is negligible relative to other scattering mechanisms at lower carrier concentrations.

1.4 Organisation of the thesis

This thesis aims to determine the optical and electronic properties of a series of CdO and SnO_2 epitaxial thin films. The fundamental band structure quantities such as the band gap and band edge effective mass of CdO, as well as the temperature dependence of these quantities have been determined. The transport properties of CdO and SnO_2 together with a surface analysis of the SnO_2 thin films are also presented. The theoretical background and underlying methods for data modelling are introduced in chapter 2. The experimental techniques and the associated computational methods based on the theory of the experiments are described in chapter 3. In chapter 4, the conduction band effective mass in CdO is determined and is used for the understanding of the dramatic decrease of the transport mobility with respect to the "optical" mobility. This is followed by the study of the temperature variations of the band gap and electron mobility of the CdO films in chapter 5. Chapter 6 introduces a layer-by-layer analysis to show the depth dependence of dislocation scattering in SnO_2 heteroepitaxial films. Surface electronic properties of SnO_2 are presented in chapter 7. Finally, the main conclusions of this study together with the future work are summarised in chapter 8.

Chapter 2

Theoretical background and methods

In this thesis, the electronic and optical properties of semicondcutors are investigated through the modelling of some measurable quantities. The main theoretical back ground is a relevant knowledge of the band structures in question. The non-parabolicity of the conduction band, especially for low band gap semiconductors, is an important issue to be considered. This realization would have a direct impact on the Fermi level and consequently the calculation of the carrier concentration within the films. An introduction to some of the electronic configurations in materials, followed by the parabolic and non-parabolic band structures are presented in section 2.1. The theoretical surface analysis here has been performed by solving the Poisson equation within the surface layer of the films followed by complementary derivations which are given in section 2.2.

2.1 Electronic and band structure calculations

In structured materials, the arrangement of ions in a lattice forms a periodic potential which gives rise to energy bands due to Pauli's exclusion principle. The characteristics of the energy bands depend on the crystal structure via the shape of the first Brillouin zone and the component elements. Each electron in a many-body system experiences the potentials of the surrounding ions as well as the pair potentials of their own. Therefore, as in an exact treatment, electrons cannot be seen as independent single particles, respective simplifications have been performed to the solution of the N-body Schrödinger equation. For instance, an appropriate choice of the potential energy within the solid in the one-electron approximation can account reasonably well for the electron-electron interaction effects.

By considering the crystal structure as an assembly of atoms, and dividing the atoms into core ions and valence electrons, the crystal Hamiltonian, ignoring

magnetic effects within the system due to spin-orbit interaction, for the lattice and the electrons can be written as follows [51]:

$$H = H_L + H_e$$

$$= \sum_l \frac{\boldsymbol{P}_l^2}{2M_l} + \sum_{l,n} U(\boldsymbol{R}_l - \boldsymbol{R}_n) + \sum_i \frac{\boldsymbol{P}_i^2}{2m} + \sum_{i,l} V(\boldsymbol{r}_i - \boldsymbol{R}_l) + \frac{e^2}{4\pi\epsilon_0} \sum_{i,j} \frac{1}{|\boldsymbol{r}_i - \boldsymbol{r}_j|}, \tag{2.1}$$

where l and n label the ions, i and j label the electrons, $\boldsymbol{P}$, M, and m are the momentum operator, the ionic mass, and the electron mass, respectively. $U(\boldsymbol{R}_l - \boldsymbol{R}_n)$ is the interionic potential, and $V(\boldsymbol{r}_i - \boldsymbol{R}_l)$, the ion-valence electron potential. Solution of the time-independent Schrödinger equation gives the stationary states and energies of the system:

$$H\Psi = E\Psi, \tag{2.2}$$

where H is the Hamiltoninan of the system; E and Ψ are the eigen values and eigen functions of H, respectively. Here, some approximations and methods of solution to the equations above are presented.

2.1.1 Born-Oppenheimer (Adiabatic) approximation

As the ratio of the ionic and electronic mass, M/m, is very high, and the ratio of the frequencies of ionic vibrations and electronic motion (involving excitations from the valence band to the conduction band) is very low, the ions move much slower and can be regarded as a frame of reference from the point of view of the electrons. Therefore, electrons can instantaneously adjust their motion to that of the ions, seeing an overall time averaged adiabatic potential. As a result, the total wave function takes the form:

$$\Psi = \Phi_{\mathrm{e}}(\boldsymbol{r}, \boldsymbol{R})\Phi_{\mathrm{L}}(\boldsymbol{R}), \tag{2.3}$$

where $\Phi_{\mathrm{L}}(\boldsymbol{R})$ is the wave function of all the ions, and $\Phi_{\mathrm{e}}(\boldsymbol{r}, \boldsymbol{R})$ that of all the electrons being instantaneously dependent on the ionic position. Substituting Eqn. 2.3

in the Schrödinger equation leads to purely ionic and purely electronic relations:

$$H_{\mathrm{L}}\Phi_{\mathrm{L}}(\boldsymbol{R}) = E_{\mathrm{L}}\Phi_{\mathrm{L}}(\boldsymbol{R}) \tag{2.4}$$

$$H_{\mathrm{e}}\Phi_{\mathrm{e}}(\boldsymbol{r},\boldsymbol{R}) = E_{\mathrm{e}}\Phi_{\mathrm{e}}(\boldsymbol{r},\boldsymbol{R}) \tag{2.5}$$

2.1.2 The one-electron approximation

If an N-state wave function is considered as multiples of N states, the electron-electron interaction term in the Hamiltonian can be divided into an averaged repulsive component (constant) and a small perturbation term contributing any deviation from this average. Therefore, each electron with state functions, $\phi_i(\boldsymbol{r}_i,\boldsymbol{R})$, can be regarded as *independently* interacting with the lattice of ions. Subsequently, the one-electron Schrödinger equation becomes:

$$\left(\frac{\boldsymbol{P}_i^2}{2m} + \sum_l V(\boldsymbol{r}_i - \boldsymbol{R}_l)\right)\phi_i(\boldsymbol{r}_i,\boldsymbol{R}) = E_i\phi_i(\boldsymbol{r}_i,\boldsymbol{R}). \tag{2.6}$$

The N-electron wave function is the product of the one-electron wave functions.

2.1.3 The mean field approximation

The reduction of the Schrödinger equation obtained above still depends on the fluctuating position of the ions, so if the electron-ion interaction is treated as if the ions are in their equilibrium positions, followed by a perturbation arising from ionic vibrations, the potential term in Eqn. 2.6 can be modified to a function of ionic equilibrium positions, $\boldsymbol{R}_{l0}$. However, the explicit ionic equilibrium position dependence of the electron potential is neglected through the assumption that every electron is experiencing the same average potential $V(\boldsymbol{r})$, often known as the one-electron potential. This is the mean field approximation in which the Schrödinger equation describing the motion of each electron is identical and given by:

$$\left(\frac{\boldsymbol{P}^2}{2m} + V(\boldsymbol{r})\right)\phi_n(\boldsymbol{r}) = E_n\phi_n(\boldsymbol{r}), \tag{2.7}$$

where $\phi_n(\boldsymbol{r})$ and E_n denote the wave function and energy of an electron in an eigenstate labeled by n (two electrons with opposite spin can fill each eigenstate).

2.1.4 Bloch functions

The eigenstates of Eqn. 2.7, where $V(\boldsymbol{r} + \boldsymbol{R}) = V(\boldsymbol{r})$ for all translational vectors, $\boldsymbol{R}$, in a Bravais lattice, can have the form:

$$\phi_{n\boldsymbol{k}}(\boldsymbol{r}) = u_{n\boldsymbol{k}}(\boldsymbol{r})\exp(i\boldsymbol{k}.\boldsymbol{r}), \tag{2.8}$$

which is the product of a plane wave and a function with the same periodicity of the Bravais lattice:

$$u_{n\boldsymbol{k}}(\boldsymbol{r} + \boldsymbol{R}) = u_{n\boldsymbol{k}}(\boldsymbol{r}). \tag{2.9}$$

Hence, there is a wave vector associated with each wave function with the periodicity of the lattice:

$$\phi_{n\boldsymbol{k}}(\boldsymbol{r} + \boldsymbol{R}) = \exp(i\boldsymbol{k}.\boldsymbol{r})\phi_{n\boldsymbol{k}}(\boldsymbol{r}). \tag{2.10}$$

n labels the band and $\boldsymbol{k}$ is the wave vector of the electron in the first Brillouin zone. The state of the electron in this formalism is determined by the wave vector of the electron and the corresponding energy, $E(\boldsymbol{k})$. In general, the band structure or the dispersion relation, $E(\boldsymbol{k})$, near the band extrema has algebraic or geometrical properties which are referred to as parabolic and non-parabolic depending on the k-space region of interest and the energy gap of the semiconductor.

2.1.5 Parabolic band approximation

The solution of Eqn. 2.7 over the whole Brillouin zone is complicated. However, in many conditions, a complete picture of the band structure in semiconductors, can be approximated by regions close to the band extrema. This is because the transport theory and many band structure parameters, are associated with this region as these states are the first to be occupied and take part in conduction.

In many semiconductors, both valence and conduction band extrema occur at the Γ point. The dispersion relation in its simplest form for states very close to this point is:

$$E_{\mathrm{e,h}}(k) = E_{\mathrm{e,h}}(0) \pm \frac{\hbar^2 k^2}{2m^*}, \tag{2.11}$$

where $E_{\mathrm{e,h}}(0)$ is the zero energy, the plus and minus signs correspond to electrons and holes respectively, and m^* is the electron or hole effective mass. Here, the effective mass at the Γ point is a scalar quantity, therefore, the constant energy surface in the k-space is spherical and the band structure is said to be isotropic. The parabolic relation holding for regions very close to the zone centre can be understood by a Taylor expansion of $E(k)$ around the Γ point. The shape of the conduction band away from the extrema varies non-parabolically with k, especially in semiconductors with lower band gap energies.

2.1.6 k.p perturbation theory

In cases where interband transitions or excitation of defect levels take place, or when a high level of dopants or defects are present in the material, the carrier concentration in the conduction band increases. Therefore, the degree of interband interactions enhances leading to a non-parabolic conduction band. This effect is more pronounced in low band gap semiconductors. In such cases, the parabolic band approximation fails to describe the band structure in question. Hence, the energy dispersion within the one-electron approximation is introduced via considering the $\boldsymbol{k}.\boldsymbol{p}$ interactions. Since the cell periodic functions of the electrons at any given $\boldsymbol{k}$ but in different bands form a complete set, the electronic wave functions at any $\boldsymbol{k}$ can be expressed in terms of the sum of the cell periodic functions of the extrema, i.e., points with known eigenkets and eigenvalues [48]:

$$\phi_{n\boldsymbol{k}}(\boldsymbol{r}) = u_{n\boldsymbol{k}}(\boldsymbol{r})\exp(i\boldsymbol{k}.\boldsymbol{r}) = \left(\sum c_m u_{m\boldsymbol{k}_0}(\boldsymbol{r})\right)\exp(i\boldsymbol{k}.\boldsymbol{r}), \tag{2.12}$$

where $\boldsymbol{k}_0$ is the position of the extrema. The Hamiltonian within the $\boldsymbol{k}.\boldsymbol{p}$ model is introduced in the Schrödinger equation as [56]:

$$H_{\boldsymbol{k}}u_{n\boldsymbol{k}}(\boldsymbol{r}) = \left[-\left(\frac{\hbar^2}{2m_0}\right)\nabla^2 + V(\boldsymbol{r}) + H_1 + H_2 + H_{\mathrm{so}}\right]u_{n\boldsymbol{k}}(\boldsymbol{r}) = E_{n\boldsymbol{k}}u_{n\boldsymbol{k}}(\boldsymbol{r}), \tag{2.13}$$

$$H_1 = \left(\frac{\hbar}{m_0}\right)\boldsymbol{k}.\boldsymbol{p}, \tag{2.14}$$

$$H_2 = \frac{\hbar^2 k^2}{2m_0}, \tag{2.15}$$

where $\boldsymbol{k}$ is the lattice wave vector and $\boldsymbol{p}$ the particle momentum operator; $V(\boldsymbol{r})$ is the lattice periodic potential, and $H_{\rm so}$ accounts for $\boldsymbol{k}$-dependent and $\boldsymbol{k}$-independent spin-orbit interactions; H_1 and H_2 are the first and second order perturbation terms, respectively. Substituting the expansion of the cell periodic functions in Eqn. 2.12 for $u_{n\boldsymbol{k}}$ in Eqn. 2.13, and using the orthogonality of the basis functions, gives a set of homogeneous linear equations (disregarding spin-orbit interactions):

$$c_l \left(E_{n\boldsymbol{k}} - E_{l\boldsymbol{k}_0} - \frac{\hbar^2}{2m_0}(k^2 - k_0^2) \right) - \frac{\hbar}{m_0} \sum c_m(\boldsymbol{k} - \boldsymbol{k}_0).\boldsymbol{p}_{lm} = 0, \tag{2.16}$$

$$\boldsymbol{p}_{lm} = \int_C u^*_{l\boldsymbol{k}_0}(\boldsymbol{r}) \boldsymbol{p} u_{m\boldsymbol{k}_0}(\boldsymbol{r}) d\boldsymbol{r}, \tag{2.17}$$

where the integral is taken over the unit cell of the crystal. In general, the solution to the above set of equations is non-trivial. Considering only the $\boldsymbol{k}$-independent spin-orbit interaction (assuming the $\boldsymbol{k}$-dependent term is negligible) in the Hamiltonian, and that the extrema of the conduction and three valence bands are at the Γ point (each being doubly degenerate), the 8×8 interaction matrix can be separated into a simpler diagonal form containing two 4×4 matrices, one for each spin state [57]:

$$H = \begin{bmatrix} \tilde{H} & 0 \\ 0 & \tilde{H} \end{bmatrix}, \tag{2.18}$$

in which,

$$\tilde{H} = \begin{bmatrix} E_s & 0 & kP & 0 \\ 0 & E_p - \Delta_{so}/3 & \sqrt{2}\Delta_{so}/3 & 0 \\ kP & \sqrt{2}\Delta_{so}/3 & E_p & 0 \\ 0 & 0 & 0 & E_p + \Delta_{so}/3 \end{bmatrix}. \tag{2.19}$$

E_s and E_p are eigenvalues of $[-(\hbar^2/2m_0)\nabla^2 + V(\boldsymbol{r})]u_{m0}(\boldsymbol{r}) = E_{m0}u_{m0}(\boldsymbol{r})$ corresponding to the conduction and valence bands respectively, $\Delta_{\rm so}$ is the spin-orbit splitting of the valence band, and P is the momentum matrix element defined by ($\boldsymbol{k}$ has been assumed to be in the z direction for p-type functions):

$$P = -\frac{i\hbar}{m_0}\langle S|p_z|Z\rangle = -\frac{i\hbar}{m_0}\int Sp_z Z d(\boldsymbol{r}), \tag{2.20}$$

$$\Delta_{\rm so} = i\frac{3\hbar}{4m_0^2c^2}\langle X|\frac{\partial V(\boldsymbol{r})}{\partial x}p_y - \frac{\partial V(\boldsymbol{r})}{\partial y}p_x|Y\rangle, \tag{2.21}$$

where, $|S\rangle$ and $|X\rangle$, $|Y\rangle$, $|Z\rangle$ are the s-type and p-type basis functions corresponding to conduction and valence bands respectively. The solution of the full set of equations over the basis functions, gives the energy eigenvalues:

$$(E' - E_s)(E' - E_p)(E' - E_p + \Delta_{so}) - k^2P^2(E' - E_p + 2\Delta_{so}/3) = 0. \tag{2.22}$$

Expressing the momentum matrix element in terms of the band edge effective mass, m_0^*, and assuming that the energy eigenvalues are small compared to the band gap, E_g, the dispersion relation for the conduction band may be simplified to:

$$E(1 + \alpha E) = \frac{\hbar^2 k^2}{2m_0^*}, \tag{2.23}$$

where energy is measured from the conduction band minimum and:

$$\alpha = \frac{1}{E_\mathrm{g}}\left(1 - \frac{m_0^*}{m_0}\right)\left(1 - \frac{E_\mathrm{g}\Delta_\mathrm{so}}{3(E_\mathrm{g} + 2\Delta_\mathrm{so}/3)(E_\mathrm{g} + \Delta_\mathrm{so})}\right). \tag{2.24}$$

In cases where the spin-orbit splitting is not comparable to the band gap, namely, $\Delta \ll E_\mathrm{g}$ and $\Delta \gg E_\mathrm{g}$ and E, which is the case for many semiconductors, the dispersion relation can be reduced to:

$$E(1 + \alpha E + \beta E^2) = \frac{\hbar^2 k^2}{2m^*}, \tag{2.25}$$

where $\alpha = (1/E_g)(1 - m^*/m_0)^2$ and $\beta = -(2/E_g^2)(m^*/m_0)(1 - m^*/m_0)$. When $m^* \ll m_0$, the dispersion relation can take the form of Eqn. 2.23 with $\alpha = 1/E_\mathrm{g}$; this is known as the α-approximation. The effective mass is a tensor quantity in three dimensions and energy-dependent. The second derivative of the dispersion relation with respect to k is no longer the reciprocal of the effective mass in non-parabolic bands. Taking into account the connection between the lattice momentum and the particle momentum within a single band and Brillouin zone, a more fundamental definition of the energy-dependent effective mass can be derived:

$$(m^*)_{ij} = \hbar^2 k_i \left(\frac{\partial E}{\partial k_j}\right)^{-1}, \tag{2.26}$$

the subscripts refer to tensor elements. Assuming isotropic bands, the relation becomes $m^* = \hbar^2 k(dE/dk)^{-1}$. A comparison between the energy dispersion and density of states within the parabolic and non-parabolic conduction bands has been

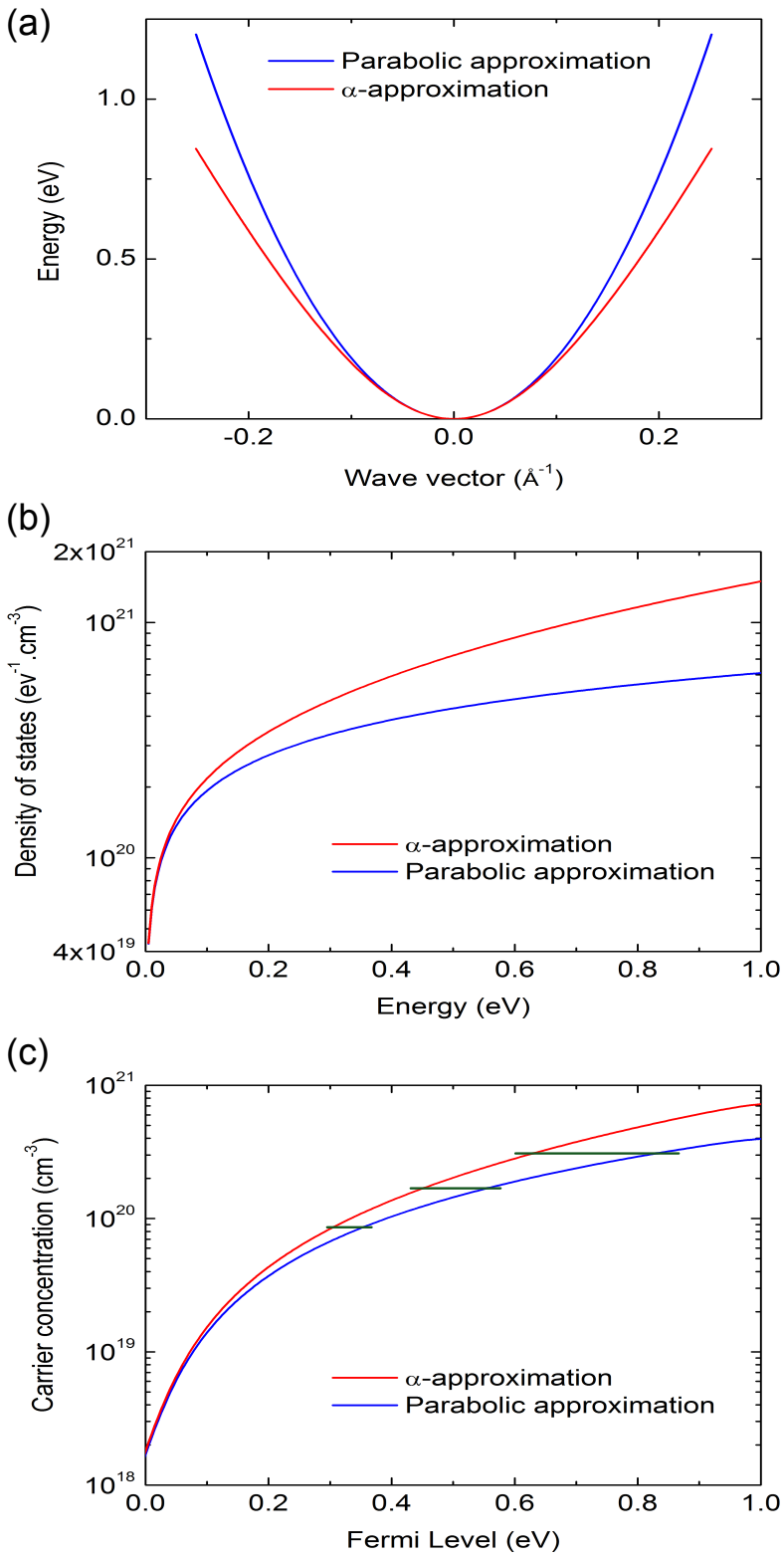

Figure 2.1: (a) Conduction band diagram for the parabolic and α-approximations. A higher slope (and in this case, a higher curvature) in the parabolic band indicates a lower density of states in the whole region which is apparent in (b). The Fermi level difference in the band filling process becomes significant at higher carrier concentrations as indicated in (c). The equivalence of the approximations at the zone centre is evident in all figures.

made in Fig. 2.1; typical values of 2 eV and $0.2m_0$ for the band gap and electron effective mass have been used, respectively [48, 51, 56–61].

2.1.7 Band gap renormalization

Pursuant to the band filling process, the many-body effects are enforced through the electron exchange and correlation energies and electron-ion interactions which lead to the narrowing of the band gap; this is called band gap renormalization (BGR). Within the one-electron approximation of the $\boldsymbol{k}.\boldsymbol{p}$ model, the effects of BGR are introduced into the energy eigenvalues via:

$$E_{\mathrm{g,BGR}}(E_{\mathrm{F}}) = E_{\mathrm{g}} + \Delta E_{e-e}(E_{\mathrm{F}}) + \Delta E_{e-i}(E_{\mathrm{F}}), \tag{2.27}$$

where [62],

$$\Delta E_{e-e}(E_{\mathrm{F}}) = -\frac{e^2 k_{\mathrm{F}}}{2\pi^2 \epsilon_0 \epsilon_{\mathrm{s}}} - \frac{e^2 k_{\mathrm{TF}}}{8\pi \epsilon_0 \epsilon_{\mathrm{s}}} \left[1 - \frac{4}{\pi} \tan^{-1}\left(\frac{k_{\mathrm{F}}}{k_{\mathrm{TF}}}\right)\right], \tag{2.28}$$

$$\Delta E_{e-i}(E_{\mathrm{F}}) = -\frac{e^2 n}{\epsilon_0 \epsilon_{\mathrm{s}} r_{\mathrm{B}}^* k_{\mathrm{TF}}^3}. \tag{2.29}$$

E_{F} and k_{F} are the Fermi energy and angular wave number, respectively; ϵ_0 is the permittivity of vacuum, and ϵ_{s} the static dielectric constant; the Thomas-Fermi screening angular wave number (k_{TF}), and the effective Bohr radius (r_{B}^*) are described by:

$$k_{\mathrm{TF}} = 2\left(\frac{k_{\mathrm{F}}}{\pi r_{\mathrm{B}}^*}\right)^{1/2}, \tag{2.30}$$

$$r_{\mathrm{B}}^* = \frac{4\pi \epsilon_0 \epsilon_{\mathrm{s}} \hbar^2}{e^2 < m^* >}, \tag{2.31}$$

where m^* is averaged over the density of states. Besides some other band structure quantities, the electron effective mass plays a decisive role in the transport properties of semiconductors.

2.2 Space charge calculations

When two materials are in intimate contact on an atomic scale, carriers from one side can diffuse into the other side leaving behing a region of ionized atoms

at the imediate vicinity of the contact. This region of immobile ions is called the space charge region. This surface charge occurs at the surface of semiconductors as a result of the broken symmetry at this region of the crystal structure. This introduces defects, or impurities such as hydrogen, which in case of ionization create a depletion or an accumulation layer at the surface.

2.2.1 Poisson's equation

Depending on the location of the Fermi level with respect to the charge neutrality level (CNL) in the bulk, depletion or accumulation of the majority carriers may take place at the surface of the semiconductor. The CNL is the level at which the Fermi level stabilization occurs for the majority carriers. As the space charge region is associated to free carriers for charge neutrality, this effect is analogous to the screening of a charged particle. Hence, the width of the space charge region is determined by the screening length of the semiconductor within which there exists a spacial band bending that is described by the Poisson equation [63]:

$$\frac{d^2V}{dz^2} = -\frac{e}{\epsilon_s \epsilon_0}\left[N_D^+ - N_A^- - n(z) + p(z)\right], \tag{2.32}$$

where, z is the distance from the surface into the bulk, ϵ_s is the static dielectric constant, N_D^+ (N_A^-) denotes the bulk ionized donor (acceptor) density, and $n(z)$ ($p(z)$) is the electron (hole) concentration in the space charge region.

The boundary conditions for Eqn. 2.32 are:

$$z \to \infty \Longrightarrow V(z) \to 0, \tag{2.33}$$

$$\left.\frac{dV}{dz}\right|_{z=0} = \frac{e}{\epsilon_s \epsilon_0} n_{ss}, \tag{2.34}$$

where n_{ss} is the surface sheet density of the semiconductor. Eqn. 2.34 is derived from Gauss' law. For an n-type semiconductor, if $V(z) < 0$, the bands bend downward, the space charge region is positively charged and there exists a surface electron accumulation. For a p-type material, the conditions above correspond to a surface depletion layer. If $V(z) > 0$, the bands bend upward, the space charge region becomes negatively charged leading to a surface accumulation (depletion) layer for a p-type

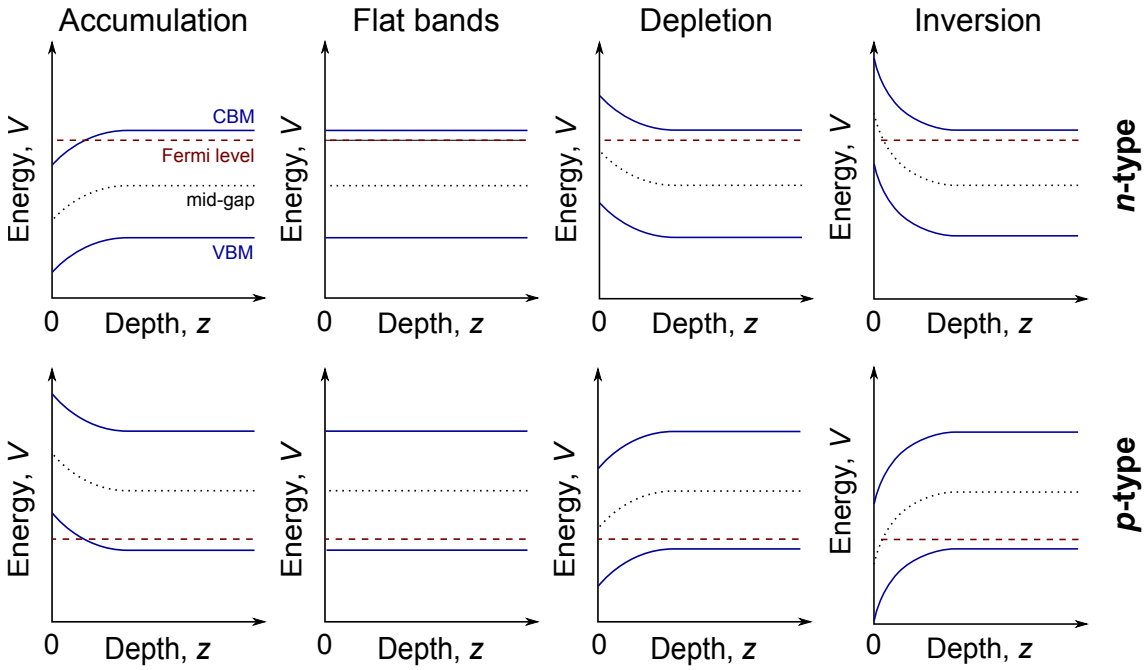

Figure 2.2: A schematic representation of different types of band bending in n- and p-type semiconductors. In an n-type semiconductor, surface electron accumulation (depletion) occurs when the Fermi level at the surface is higher (lower) than in the bulk with reference to the CBM; the condition is reversed in p-type semiconductors. In the case of inversion, the condition is similar to a depletion layer where the area is depleted of the majority carriers, apart from the very top surface layers where the type of carriers are inverted.

(n-type) semiconductor. Four different conditions of band bending at semiconductor surfaces are shown in Fig. 2.2.

2.2.2 Modified Thomas-Fermi approximation

The Modified Thomas-Fermi approximation (MTFA) [64] takes into account the boundary condition for the envelope wave function of the electrons at the surface of the semiconductor. The Poisson equation is solved by calculating the carrier concentrations via,

$$n(z) = \int_0^{\infty} g_{\mathrm{c}}(E) f'_{\mathrm{FD}}(E) f_{\mathrm{MTFA}}(z) dE, \tag{2.35}$$

$$p(z) = \int_{E_{\mathrm{V}}}^{-\infty} g_{\mathrm{v}}(E) f'_{\mathrm{FD}}(E) f_{\mathrm{MTFA}}(z) dE, \tag{2.36}$$

where $g(E)$ is the density of states; $f'_{\mathrm{FD}}(E)$ is the space-dependent Fermi-Dirac distribution function including the spatial variation of the potential, and $f_{\mathrm{MTFA}}(z)$

is the MTFA factor:

$$f'_{\mathrm{FD}}(E) = \frac{1}{1+\exp[\beta(E-\mu+V(z)]}, \tag{2.37}$$

$$f(z) = 1 - \mathrm{sinc}\left[\frac{2z}{L}\left(\frac{E}{K_{\mathrm{B}}T}\right)^{1/2}\left(1+\frac{E}{E_{\mathrm{g}}}\right)^{1/2}\right], \tag{2.38}$$

where $\mathrm{sinc}(x) = \frac{\sin(x)}{x}$. L is the thermal De Broglie wave length defined as the average De Broglie wave length of a particle at a specific temperature. If this value is much smaller than the interparticle distance, $(V/N)^{(1/3)}$ (V being the volume and N the number of particles), the medium obeys the Maxwell-Boltzmann statistics. In cases where this value is comparable or larger than the interparticle distance, the Fermi-Dirac statistics should be used for Fermions. For non-degenerate semiconductors,

$$L = \frac{\hbar}{(2m_0^* K_{\mathrm{B}}T)^{1/2}}. \tag{2.39}$$

For degenerate semiconductors, $L = 1/k_{\mathrm{F}}$ is used which is the Fermi length, and k_{F} is the Fermi wave number [65]. Since the carriers are confined in the z-direction within the space charge region, the boundary condition requires that the carrier concentration smoothly tends to zero at the boundaries as if the carriers are represented by standing wave functions (interfering incident and reflected waves). This condition is satified by the use of the MTFA factor, $f_{\mathrm{MTFA}}(z)$ [65, 66].

Using the relevant physical quantities and band parameter values of a semiconductor, a numerical modelling of the $C-V$ data is possible to obtain the spatial band bending and carrier concentration variation within the surface layer of the material. The method of interval bisection is used in the modelling of the boundary conditions expressed in 2.33 and 2.34 for the edge of the space charge region towards the bulk where the energy bands flatten out.

2.3 Summary

The theoretical band structure approach throughout this thesis is based on the non-parabolic band within the one-electron $\boldsymbol{k}.\boldsymbol{p}$ approximation. The many body effects resulting in the variation of the fundamental band gap are included as in-

troduced in section 2.1.7. Surface electronic properties of the SnO_2 films are dealt with through the solution of Poisson's equation described in section 2.2. The MTFA approximation, described in section 2.2.2, has been employed for the calculation of the surface electron accumulation to account for the boundary condition of the wave functions at the surface of the layers.

Chapter 3

Experimental techniques and computational methods

The experimental techniques throughout this thesis include optical reflection, transmission, and absorption spectroscopy, Hall effect and electrochemical capacitance-voltage measurements, X-ray photoemission and X-ray diffraction spectroscopy, and transmission electron microscopy. This chapter presents an introduction to the physics of these experimental techniques followed by the respective computational methods for data analysis.

3.1 Optical spectroscopy

3.1.1 Infrared reflectance

The mid-infrared (MIR) region of the optical spectrum is where low energy oscillations such as phonons and plasmons (collective carrier oscillations in the conduction band) take place in semiconductors. These oscillations are mainly phonons and plasmons. Metals and doped semiconductors can be treated as plasmas as they have equal numbers of ionic charge states and free electrons. In conditions where the energy of the plasma oscillations is higher than that of the phonons the effects of plasma reflection becomes apparent in the IR spectrum. When oscillating near the resonance frequency, the plasmons have taken on a maximal amount of energy from the radiation. As in any vibration, plasmons are damped mostly by the ionized centres present in the material. Plasmon damping lowers the reflectance for a given plasma frequency while broadening the spectrum as the plasma frequency increases.

The plasmon energy in a material within the free electron model is related to the free electron concentration, n, high frequency dielectric constant, $\epsilon(\infty)$, and

electron effective mass, m^*, and calculated via:

$$\omega_{\mathrm{p}}^2 = \frac{ne^2}{\epsilon_0 \epsilon(\infty)\langle m^* \rangle}, \tag{3.1}$$

$$E_{\mathrm{p}} = \hbar\omega_{\mathrm{p}}. \tag{3.2}$$

In cases where the conduction band is not parabolic, and due to the fact that plasma oscillations are collective intraband oscillations, the effective mass should be averaged over all the occupied states:

$$\langle m^*(E) \rangle = \frac{\int m^*(E) g(E) f(E, E_{\mathrm{F}}) dE}{\int g(E) f(E, E_{\mathrm{F}}) dE}, \tag{3.3}$$

where, $g(E)$ is the density of states and $f(E, E_{\mathrm{F}})$ is the Fermi-Dirac statistics. This equation could then be used in conjunction with the plasmon energy determined through MIR reflectance simulations.

3.1.1.1 Dielectric functions

The physical interaction of light with matter in respect of polarization and absorption properties is described by its dielectric function. Several functions have been used for simulation of the reflectance spectra based on different possible interactions. Some of them are briefly introduced below.

- **The two-oscillator model**

  This dielectric function only deals with two oscillations in the material, namely, one pertaining to the carriers and one to the phonons,

  $$\tilde{\epsilon}(\omega) = \tilde{n}^2(\omega) = \epsilon(\infty) + \frac{(\epsilon(0) - \epsilon(\infty))\omega_{\mathrm{TO}}^2}{\omega_{\mathrm{TO}}^2 - \omega^2 - i\omega\gamma_{\mathrm{TO}}} - \frac{\epsilon(\infty)\omega_{\mathrm{p}}^2}{\omega(\omega + i\gamma_{\mathrm{p}})} = \tilde{\epsilon}_{\mathrm{ion}}(\omega) + \tilde{\epsilon}_e(\omega), \tag{3.4}$$

  where $\tilde{n}$ is the refractive index, $\epsilon(\infty)$ and $\epsilon(0)$ are high frequency and static dielectric constants, respectively; ω_{TO} is a transverse optical phonon frequency and γ_{TO} is the respective phonon damping. ω_{p} and γ_p are the plasmon frequency and damping. The first and second term on the right-hand side denote the lattice and carrier contributions, respectively. This model is the simplest model to be used to obtain the refractive index of the semiconductor.

- **The three oscillator model**

  This model involves two phonons and one carrier oscillations [67],

$$\epsilon(\omega) = \epsilon(\infty)\left(\frac{\omega_{\mathrm{LO}}^2 - \omega^2 - i\omega\gamma}{\omega_{\mathrm{TO}}^2 - \omega^2 - i\omega\gamma} - \frac{\omega_{\mathrm{p}}^2}{\omega(\omega + i\gamma_{\mathrm{p}})}\right). \tag{3.5}$$

  In this model, two phonon oscillations, namely, one longitudinal and one transverse optical mode are used along with the classical Drude model for the carrier response. The phonon damping is assumed to have the same value for both optical modes.

- **The classical dispersion or damped harmonic (Lorentzian) model**

  This model is used for the lattice response and is combined with the Drude model for the carrier response [68],

$$\epsilon(\omega) = \epsilon(\infty) + \sum_{i=1}^{n} \frac{S_i\omega_{\mathrm{TO},i}^2}{\omega_{\mathrm{TO},i}^2 - \omega^2 - i\omega\gamma_{\mathrm{TO},i}}, \tag{3.6}$$

  where S is the oscillator strength.

- **The factorized model for the lattice response**

  This model includes all the IR-active phonons and the corresponding coupling of the LO and TO phonon modes [69],

$$\tilde{\epsilon}(\omega) = \epsilon(\infty)\prod_{i}^{l} \frac{\omega_{\mathrm{LO},i}^2 - \omega^2 - i\omega\gamma_{\mathrm{LO},i}}{\omega_{\mathrm{TO},i}^2 - \omega^2 - i\omega\gamma_{\mathrm{TO},i}}, \tag{3.7}$$

  in which, the broadening of the oscillators is Lorentzian. This model, in contrast to previous models where the anharmonic effect of phonon coupling is excluded, considers independent broadening of the LO and TO phonons.

- **The optical phonon-plasmon coupling model**

  When the plasmon energies are close to or in the range of the LO and TO phonon modes, they strongly interact with the LO phonon modes of the lattice. The dielectric function of a plasmon-phonon multi-mode system with m

plasmon and n phonon bands is [69]:

$$\epsilon_j(\omega) = \epsilon_j(\infty)\frac{\prod_{i=1}^{m+n}(\omega_{\mathrm{LPP},ij}^2 - i\gamma_{\mathrm{LPP},ij}\omega - \omega^2)}{\omega^m \prod_{i=1}^{m}(\omega + i\gamma_{\mathrm{p},ij}) \prod_{i=1}^{n}(\omega_{\mathrm{TO},ij}^2 - i\gamma_{\mathrm{TO},ij}\omega - \omega^2)}, \tag{3.8}$$

where, j denotes different optical branches. $\omega_{\mathrm{LPP},ij}$ and $\gamma_{\mathrm{LPP},ij}$ are the frequency and damping of the longitudinal optical phonon-plasmon (LPP) coupling modes and $\gamma_{\mathrm{p},ij}$ describes the plasmon damping in the limit of zero wave vector. For a single optical branch, considering two LPP coupling modes, Eqn. 3.8 yields:

$$\epsilon(\omega) = \epsilon(\infty)\frac{(\omega_{\mathrm{LPP},+}^2 - i\gamma_{\mathrm{LPP},+}\omega - \omega^2)(\omega_{\mathrm{LPP},-}^2 - i\gamma_{\mathrm{LPP},-}\omega - \omega^2)}{(\omega^2 + i\gamma_{\mathrm{p}}\omega)(\omega_{\mathrm{TO}}^2 - i\gamma_{\mathrm{TO}}\omega - \omega^2)}, \tag{3.9}$$

and,

$$\omega_{\mathrm{LPP},\pm} = \left\{\frac{1}{2}\left[\omega_{\mathrm{LO}}^2 + \omega_{\mathrm{p}}^2 \pm \sqrt{(\omega_{\mathrm{LO}}^2 + \omega_{\mathrm{p}}^2)^2 - 4\omega_{\mathrm{p}}^2\omega_{\mathrm{TO}}^2}\right]\right\}^{1/2}, \tag{3.10}$$

where, $\omega_{\mathrm{LPP},\pm}$ are the frequencies of the upper (+) and lower (-) LPP coupling mode.

The high frequency dielectric constant and the plasmon energy are the quantities common to the dielectric functions and Eqn. 3.1. Therefore, n/m^* could be determined directly from Eqn. 3.1, and $1/(\gamma_{\mathrm{p}}m^*)$ could give the "optical mobility" by knowing the effective mass. These will be discussed for cadmium oxide in chapter 4 and 6.

3.1.1.2 The transfer matrix method

A stratified medium consisting of several layers with different thicknesses and refractive index is considered. Hence, the system has a one-dimensional inhomogeneity. The transfer matrix method has been used for this purpose including coherent, incoherent and partially coherent interference. The schematic is shown in Fig. 3.1. The reflectivity and transmissivity at each interface is calculated based on the Fresnel equations [70]. By applying Snell's law, for a specular reflection we

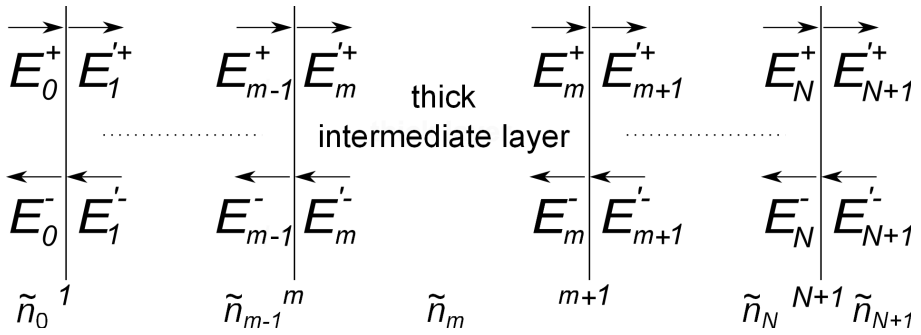

Figure 3.1: A schematic representation of a multi-layer system with the corresponding electric field amplitudes.

obtain:

$$\tilde{r}^p_{m,m+1} = \frac{\tilde{n}_{m+1}\cos\tilde{\theta}_m - \tilde{n}_m\cos\tilde{\theta}_{m+1}}{\tilde{n}_{m+1}\cos\tilde{\theta}_m + \tilde{n}_m\cos\tilde{\theta}_{m+1}} \tag{3.11a}$$

$$\tilde{t}^p_{m,m+1} = \frac{2\tilde{n}_m\cos\tilde{\theta}_m}{\tilde{n}_{m+1}\cos\tilde{\theta}_m + \tilde{n}_m\cos\tilde{\theta}_{m+1}} \tag{3.11b}$$

$$\tilde{r}^s_{m,m+1} = \frac{\tilde{n}_m\cos\tilde{\theta}_m - \tilde{n}_{m+1}\cos\tilde{\theta}_{m+1}}{\tilde{n}_m\cos\tilde{\theta}_m + \tilde{n}_{m+1}\cos\tilde{\theta}_{m+1}} \tag{3.11c}$$

$$\tilde{t}^s_{m,m+1} = \frac{2\tilde{n}_m\cos\tilde{\theta}_m}{\tilde{n}_m\cos\tilde{\theta}_m + \tilde{n}_{m+1}\cos\tilde{\theta}_{m+1}}, \tag{3.11d}$$

where, $\tilde{n}$ and θ are the complex refractive index and complex angles of propagation in each medium. Considering a coherent system as a starting point, the field amplitudes on the left-hand side of an interface are related to the corresponding field amplitudes on the right-hand side by the product of their dynamical matrices D_j [71]:

$$\begin{aligned}\begin{pmatrix} E^+_m \\ E^-_m \end{pmatrix} &= \mathbf{D}^{-1}_m \mathbf{D}_{m+1} \begin{pmatrix} E'^+_{m+1} \\ E'^-_{m+1} \end{pmatrix} \\ &= \frac{1}{\tilde{t}_{m,m+1}} \begin{bmatrix} 1 & \tilde{r}_{m,m+1} \\ \tilde{r}_{m,m+1} & 1 \end{bmatrix} \begin{pmatrix} E'^+_{m+1} \\ E'^-_{m+1} \end{pmatrix},\end{aligned} \tag{3.12}$$

the 2×2 matrix resulting from the product of dynamical matrices is called the refraction or transmission matrix of the interface, $\mathbf{D}_{j-1,j}$, which has the same form for both $s-$ and $p-$polarization when expressed in terms of the corresponding Fresnel equations.

The effect of the bulk of each layer on the field amplitudes is represented by

a propagation matrix, $\mathbf{P}$:

$$\begin{pmatrix} E'^{+}_{m+1} \\ E'^{-}_{m+1} \end{pmatrix} = \mathbf{P}_{m+1} \begin{pmatrix} E^{+}_{m+1} \\ E^{-}_{m+1} \end{pmatrix} = \begin{bmatrix} \exp(-i\tilde{\delta}_{m+1}) & 0 \\ 0 & \exp(i\tilde{\delta}_{m+1}) \end{bmatrix} \begin{pmatrix} E^{+}_{m+1} \\ E^{-}_{m+1} \end{pmatrix}, \tag{3.13}$$

in which,

$$\tilde{\delta}_j = 2\pi\bar{k}\tilde{n}_j d_j \cos\tilde{\theta}_j \tag{3.14}$$

is the phase change resulting from one traversal of light in the jth layer. $\bar{k}$ and d_j are the wave number of the incident light and the thickness of the jth layer respectively. The application of the above transformations by successive multiplications of the dynamical and propagation matrices leads to the product:

$$\begin{pmatrix} E^{+}_{0} \\ E^{-}_{0} \end{pmatrix} = \mathbf{D}_0^{-1} \left[\prod_{m=1}^{N} \mathbf{D}_m \mathbf{P}_m \mathbf{D}_m^{-1} \right] \mathbf{D}_{N+1} \begin{pmatrix} E'^{+}_{N+1} \\ E'^{-}_{N+1} \end{pmatrix} = \mathbf{T}_{0,N+1} \begin{pmatrix} E'^{+}_{N+1} \\ E'^{-}_{N+1} \end{pmatrix}, \tag{3.15}$$

where $\mathbf{T}_{0,N+1}$ is a 2×2 matrix referred to as the system transfer matrix from which the complex reflection and transmission coefficients of the system are obtained:

$$\tilde{r}_{0,N+1} = \left. \frac{E^{-}_{0}}{E^{+}_{0}} \right|_{E'^{-}_{N+1}=0} = \frac{T_{21}}{T_{11}} \tag{3.16a}$$

$$\tilde{t}_{0,N+1} = \left. \frac{E'^{+}_{N+1}}{E^{+}_{0}} \right|_{E'^{-}_{N+1}=0} = \frac{1}{T_{11}} \tag{3.16b}$$

$$\tilde{r}_{N+1,0} = \left. \frac{E^{-}_{N+1}}{E^{+}_{N+1}} \right|_{E^{+}_{0}=0} = -\frac{T_{12}}{T_{11}} \tag{3.16c}$$

$$\tilde{t}_{N+1,0} = \left. \frac{E^{-}_{0}}{E^{+}_{N+1}} \right|_{E^{+}_{0}=0} = \frac{\mathrm{Det}\, T}{T_{11}}. \tag{3.16d}$$

The system transfer matrix for a coherent system can be expressed in terms of complex reflection and transmission coefficients:

$$\mathbf{T}_{0,N+1} = \frac{1}{\tilde{t}_{0,N+1}} \begin{bmatrix} 1 & -\tilde{r}_{N+1,0} \\ \tilde{r}_{0,N+1} & \tilde{t}_{0,N+1}\tilde{t}_{N+1,0} - \tilde{r}_{0,N+1}\tilde{r}_{N+1,0} \end{bmatrix}. \tag{3.17}$$

The reflectance of the system can be evaluated by averaging that of the two perpendicular polarizations:

$$R = \frac{1}{2}(R^p + R^s) \tag{3.18}$$

$$= \frac{1}{2}(|\tilde{r}^p|^2 + |\tilde{r}^s|^2). \tag{3.19}$$

In the presence of a thick layer where the reflection and transmission of light within the system become incoherent, the system would be reduced to two representative interfaces pertaining to the m interfaces on the left-hand side and $(N+1)-m$ on the right with intensity components:

$$\mathbf{T}^{\text{int}}_{0,m} = \frac{1}{|\tilde{t}_{0,m}|^2} \begin{bmatrix} 1 & -|\tilde{r}_{m,0}|^2 \\ |\tilde{r}_{0,m}|^2 & (|\tilde{t}_{0,m}\tilde{t}_{m,0}|^2 - |\tilde{r}_{0,m}\tilde{r}_{m,0}|^2) \end{bmatrix} \tag{3.20}$$

The same format is for $\mathbf{T}^{\text{int}}_{m,N+1}$. The respective intensity propagation matrix will have the form:

$$\mathbf{P}^{\text{int}}_{l} = \begin{bmatrix} |\exp(-i\tilde{\delta}_l)|^2 & 0 \\ 0 & |\exp(i\tilde{\delta}_l)|^2 \end{bmatrix}. \tag{3.21}$$

Therefore, the intesity generic matrix takes the form:

$$\mathbf{T}^{\text{incoh}}_{0,N+1} = \mathbf{T}^{\text{int}}_{0,m}\mathbf{P}^{\text{int}}_{m}\mathbf{T}^{\text{int}}_{m,N+1}. \tag{3.22}$$

The reflectance and transmittance of the system are subsequently obtained:

$$R^{\text{incoh}}_{0,N+1} = \frac{T^{\text{incoh}}_{21}}{T^{\text{incoh}}_{11}}, \tag{3.23}$$

$$T^{\text{incoh}}_{0,N+1} = \frac{1}{T^{\text{incoh}}_{11}}. \tag{3.24}$$

The total reflectance of the system for an unpolarized light can be evaluated similarly using Eqn. 3.18. The treatment for a system with more than one incoherent layer could be performed correspondingly.

In cases where surfaces and interfaces in the stratified medium are not smooth, partial coherence takes place resulting from macroscopic roughness. The Fresnel equations are modified by an exponential term including the effect of these irregu-

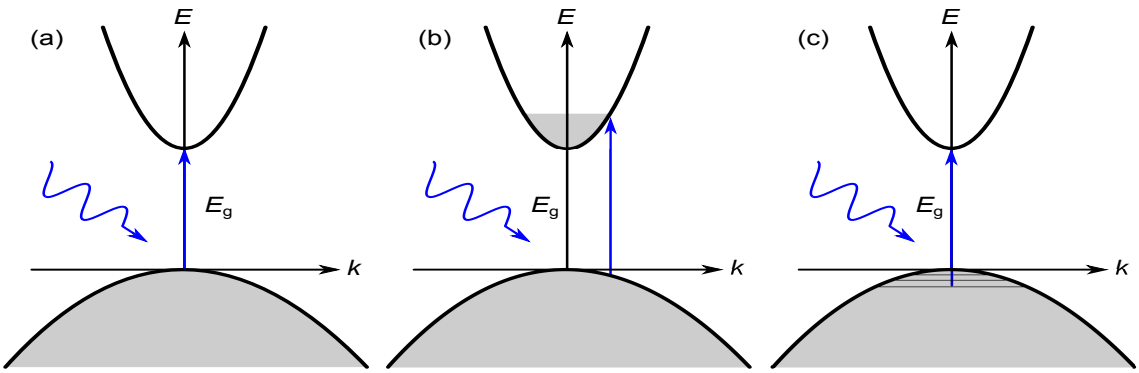

Figure 3.2: Schematic representation of direct interband excitations. (a) A direct allowed transition from the valence band maximum (VBM) to the conduction band minimum (CBM) at $k=0$; (b) the band filling effect (Burstein-Moss shift) which drives the transitions away from the zone centre; (c) transitions from lower bands when direct transitions are forbidden from the highest lying VBs due to band symmetry.

larities across surfaces and/or interfaces:

$$\tilde{r}'_{m-1,m} = \tilde{r}_{m-1,m} \exp(-2(2\pi\bar{k}\tilde{n}_{m-1}Z)^2) \tag{3.25a}$$

$$\tilde{r}'_{m,m-1} = \tilde{r}_{m,m-1} \exp(-2(2\pi\bar{k}\tilde{n}_{m}Z)^2) \tag{3.25b}$$

$$\tilde{t}'_{m-1,m} = \tilde{t}_{m-1,m} \exp(-(2\pi\bar{k}Z)^2(\tilde{n}_m - \tilde{n}_{m-1})^2/2) \tag{3.25c}$$

$$\tilde{t}'_{m,m-1} = \tilde{t}_{m,m-1} \exp(-(2\pi\bar{k}Z)^2(\tilde{n}_{m-1} - \tilde{n}_{m})^2/2), \tag{3.25d}$$

where Z is the root-mean-square height of the irregularities. The exponential coefficients (phase factors) correspond to a Gaussian distribution of irregularities. The effects of roughness in the reflectance is more pronounced at higher incident frequencies.

3.1.2 Interband absorption

In semiconductors, the optical interband transitions are a measure of their transparency. Optical absorption spectroscopy can provide information about the onset of these transitions. Figure 3.2 illustrates three possible conditions in direct interband excitations. In many cases, as in highly doped semiconductors [Fig. 3.2(b)] or when transitions could be dipole forbidden [Fig. 3.2(c)], the interband transitions do not take place between the band extrema. Hence, the data obtained by this technique can only give the minimum direct allowed band to band transitions,

namely, the optical gap. The determination of the electronic or fundamental band gap requires band structure modelling and simulation of these results.

The optical gap is determined through the absorption coefficient, α, which is calculated using the reflection and transmission data:

$$\alpha = \frac{1}{d\cos\theta}\ln\frac{2TR^2}{\sqrt{(1-R)^4+4T^2R^2}-(1-R)^2}, \tag{3.26}$$

where, d is the film thickness, θ is the angle of incidence, R and T are the reflection and transmission, respectively. The equation above holds for a single-layer system or a two-layer system with the second layer, e.g. the substrate, having an absorption edge well above the film. For normal incidences where the reflection data couldn't be collected, it is calculated via:

$$R(\omega) = \left|\frac{\tilde{n}(\omega)-1}{\tilde{n}(\omega)+1}\right|^2 = \frac{(n(\omega)-1)^2+k(\omega)^2}{(n(\omega)+1)^2+k(\omega)^2}, \tag{3.27}$$

where, $\tilde{n}$, is the complex refractive index. As the reflection in this process is measured in the transparent region, the extinction coefficient, $k(\omega)$, could be set to zero in Eqn. 3.27.

Theoretically, α is determined by summing up the rate of all possible transitions by photon absorption [72–74]:

$$T_{if}(h\nu) = \frac{2\pi}{\hbar}\left|M_{if}\right|^2 g_{if}(h\nu), \tag{3.28}$$

$$\alpha(h\nu) \propto \sum T_{if}(h\nu). \tag{3.29}$$

T_{if} is the transition rate between $|i>$ and $|f>$ eigenstates, M_{if} is the transition amplitude of the perturbation which defines the transition probability between the two states, and g_{if} is the joint density of states which describes the distribution of states within the bands. Equation 3.28 is called Fermi's golden rule. For parabolic valence and conduction bands,

$$\alpha(h\nu) \propto (h\nu - E_{\mathrm{g}})^{1/2}. \tag{3.30}$$

Therefore, plotting the measured α^2 as a function of energy, the optical gap can be determined by a linear extrapolation of the sharp onset to the base line which

pertains to the background absorption.

3.1.3 Fourier transform infrared (FTIR) spectrometer

Optical measurements have been performed using a Bruker vertex 70v FTIR spectrometer capable of producing polarized light and variable-angle measurements. The energy range for measurements lies between 420 and 22,000 cm^{-1} (52 to 2728 meV) which corresponds to the MIR and visible region of the electromagnetic spectrum.

Infrared light emitted from a source passes through the sample compartment after being modulated into an interferogram in a Michelson-type interferometer. The signal reaching the detector undergoes a Fourier transform by an FT computer and the outcome is the spectrum which is to be analyzed. An FTIR spectrometer layout is shown in Fig. 3.3. The interferometer is the heart of an FT-IR spectrometer. The collimated light from the infrared source impinges on a beam splitter which ideally transmits 50% of the light and reflects the remaining part. The reflected light having travelled the distance L hits a fixed mirror, M_1, where it reflects and hits the beamsplitter again. The transmitted part of the beam is directed onto a movable mirror, M_2. As M_2 moves back and forth with a constant speed about the corresponding position, L, by a distance Δx, the light returning from the two mirrors is recombined at the beamsplitter, with the two beams having a path length difference of $2\Delta x$. The beams are spatially coherent and interfere with each other when recombined. Depending on whether the optical path length is an even or odd multiple of half the wavelength, they undergo constructive or destructive interference, respectively. The complete functional relationship between $I(\Delta x)$ and Δx is given by the cosine function:

$$I(\Delta x) = S(\bar{k}) \cos(2\pi \bar{k} \Delta x), \tag{3.31}$$

where $S(\bar{k})$ is the intensity of a monochromatic spectral line at wave number $\bar{k}$. The spectrometers are equipped with a polychromatic light source and the interference mentioned above occurs at each wavelength. The interference pattern produced

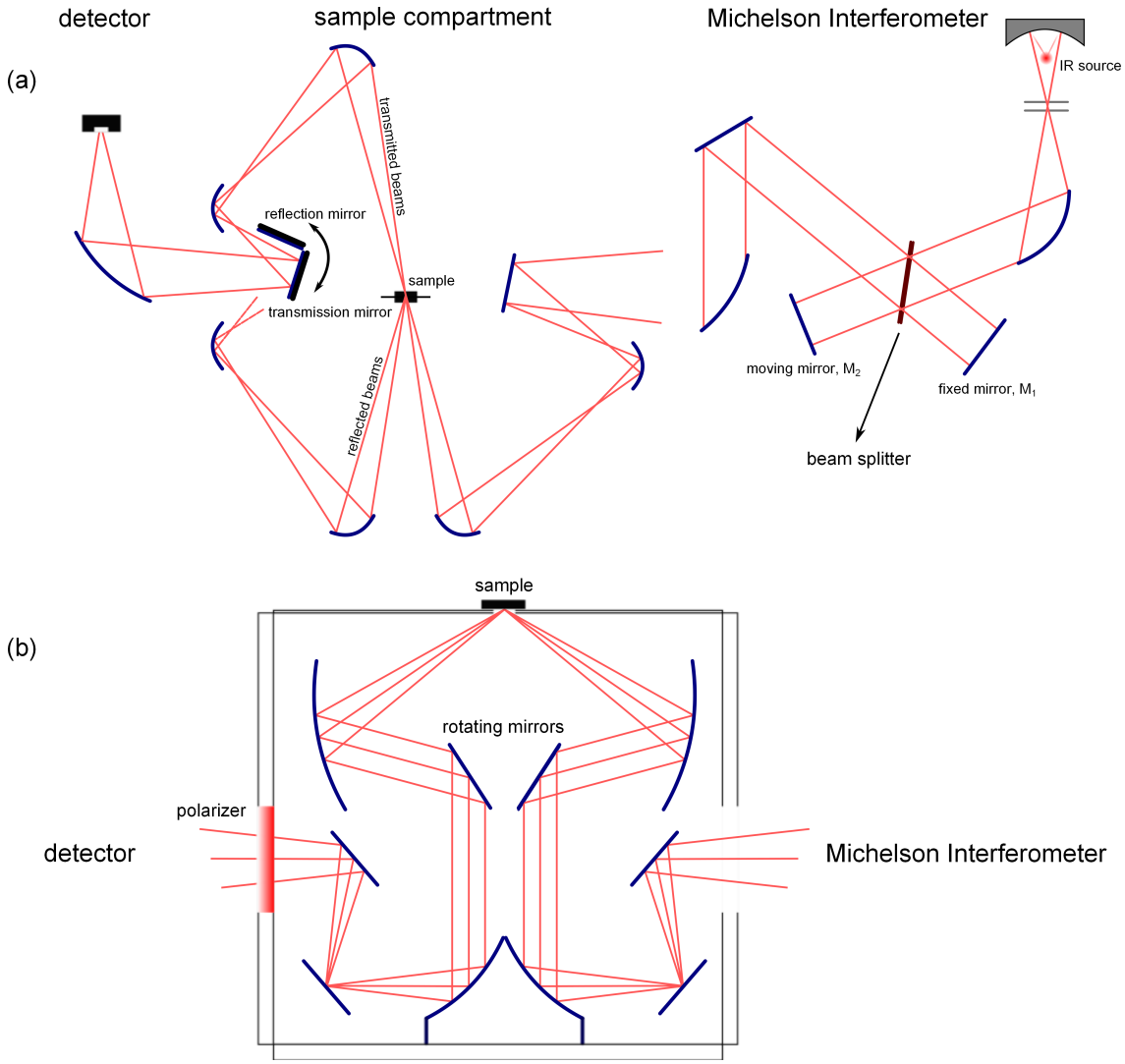

Figure 3.3: Schematic representation of the FTIR spectrometer: the interferometer, sample compartment, and detector. At the interferometer the polychromatic light from the source undergoes an interference of the constituent wavelenghts by the use of a beam splitter and a movable mirror which alters the optical path length of the transmitted light. This produces an interference pattern called the interferogram which peaks at a certain mirror position. This is ultimately Fourier transformed into its constituent frequencies having passed through the sample compartment and the detector. The geometry shown in the sample compartment (a) represents combined reflection and transmission at an incident angle of 11° while maintaining the same optical path length for both conditions. Coupled mirrors on a rotating motor enable switching between reflection and transmission measurements. (b) shows the geometry of a variable angle reflection measurement; The rotating mirrors are used to adjust the desired angle of incidence. An optional polarizer can also be attached in both configurations to be used for optically anisotropic crystals.

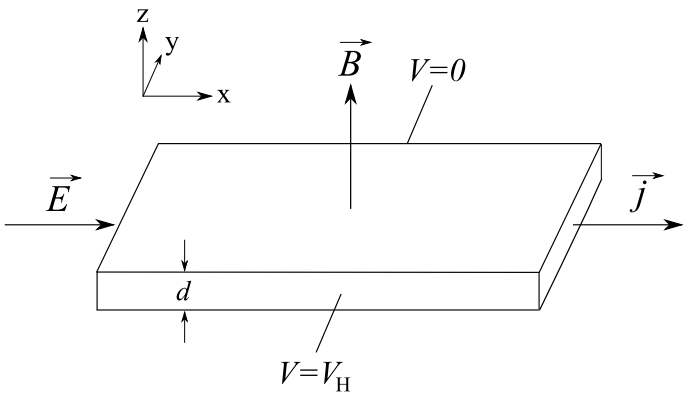

Figure 3.4: Schematic representation of the Hall effect.

by each wave length are summed to get the resulting interferogram as being the intensity as a function of optical retardation.

3.2 Hall effect

Hall effect measurements are capable of evaluating significant electronic quantities in semiconductors, namely, resistivity, sheet carrier concentration and carrier type (n- or p-type), and the mobility of the majority carriers. The experimental method of four probe contacts placed on the perimeter of the material was first propounded by Leo J. Van de Pauw [75]. This is the method used here and is illustrated in this section. The Hall effect is shown schematically in Fig. 3.4 where the charge carriers moving in an electric field are subjected to a perpendicular magnetic field. The Lorentz force, $\boldsymbol{F} = q(\boldsymbol{E} + \boldsymbol{v} \times \boldsymbol{B})$, acting on the carriers causes a transverse electric field called the Hall field. The Hall field direction for positive carriers will be opposite to that for negative carriers. Therefore, the Hall effect measurement is capable of determining the carrier type in a material. The magnitude of the Hall voltage, V_{H}, is related to the sheet carrier density, n_{s}, by:

$$n_s = \frac{IB}{e|V_{\mathrm{H}}|}, \tag{3.32}$$

where e is the elementary charge. From n_{s}, the bulk carrier density, n, can be determined by $n_{\mathrm{s}} = nd$, where d is the sample thickness. The sheet carrier density

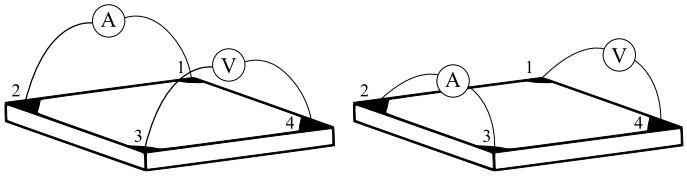

Figure 3.5: The Van der Pauw technique for resistance measurements.

and the Hall voltage are related to mobility via the sheet resistance, R_{s}:

$$\mu = \frac{|V_{\mathrm{H}}|}{R_{\mathrm{s}} I B} = \frac{1}{e n_{\mathrm{s}} R_{\mathrm{s}}}, \tag{3.33}$$

R_{s} is obtained via the Van der Pauw equation such that:

$$\exp(-\pi R_A/R_{\mathrm{s}}) + \exp(-\pi R_B/R_{\mathrm{s}}) = 1, \tag{3.34}$$

where R_A and R_B are characteristic resistances associated with the corresponding terminals of the sample in the Van der Pauw technique for resistance measurements. This is schematically shown in Fig. 3.5. The bulk resistance of a material can be obtained by $R = R_{\mathrm{s}} d$. For measuring the Hall voltage, where a constant magnetic field, $\boldsymbol{B}$, is applied perpendicular to the sample surface, the measurement configuration alters slightly as shown in Fig. 3.6. This configuration well simulates Fig. 3.4 as $V_{\mathrm{H}} = V_{24}$. Therefore, by obtaining R_{s} and V_{H} from resistance and Hall measurements, n_{s} and μ can be calculated.

For both the resistance and Hall measurements, a series of voltage measurements must be performed to make sure of the consistency and accuracy of the outcome. The typical measurement shown in figures 3.5 and 3.6, should be performed for all similar set of terminals and also repeated for the reverse direction of the current (and magnetic field for the Hall measurements).

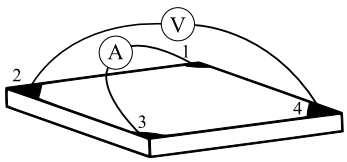

Figure 3.6: The Van der Pauw technique for Hall measurements.

3.2.1 Resistance and Hall measurements

A complete set of resistance measurements yield:

$$R_{12,43} = \frac{V_{43}}{I_{12}}, R_{21,34} = \frac{V_{34}}{I_{21}}, R_{34,21} = \frac{V_{21}}{I_{34}}, R_{43,12} = \frac{V_{12}}{I_{43}},$$
$$R_{23,14} = \frac{V_{14}}{I_{23}}, R_{32,41} = \frac{V_{41}}{I_{32}}, R_{41,32} = \frac{V_{32}}{I_{41}}, R_{14,23} = \frac{V_{23}}{I_{14}}. \quad (3.35)$$

For consistency upon current reversal, the reciprocity theorem requires:

$$R_{12,43} + R_{21,34} = R_{34,21} + R_{43,12},$$
$$R_{23,14} + R_{32,41} = R_{41,32} + R_{14,23}. \quad (3.36)$$

Hence,

$$R_{\mathrm{A}} = \frac{R_{12,43} + R_{21,34} + R_{34,21} + R_{43,12}}{4},$$
$$R_{\mathrm{B}} = \frac{R_{23,14} + R_{32,41} + R_{41,32} + R_{14,23}}{4}. \quad (3.37)$$

For Hall measurement, eight voltages are acquired for two diagonal sets. In that way, the Hall voltage, V_{H}, is calculated:

$$V_{\mathrm{H}} = \frac{V_{13}^{\mathrm{P}} - V_{13}^{\mathrm{N}} + V_{31}^{\mathrm{P}} - V_{31}^{\mathrm{N}} + V_{24}^{\mathrm{P}} - V_{24}^{\mathrm{N}} + V_{42}^{\mathrm{P}} - V_{42}^{\mathrm{N}}}{8} \quad (3.38)$$

The carrier-type of a film is determined from the above summation; if the sum is positive (negative), the sample is p-type (n-type).

Generally, it is worth noting that some primary practical aspects have to be considered when carrying out these measurements: 1. Ohmic contact quality and size; the size of the contacts and the sample thickness must be small compared to the sample lateral dimensions; 2. Sample uniformity; 3. Thermomagnetic effects due to non-uniform temperature; and 4. Measuring in a dark environment to minimize photoconductive and photovoltaic effects.

3.2.2 Hall effect apparatus

Resistance and Hall effect measurements are performed using an Ecopia HMS-3000 Hall effect measurement system. The measurements can be performed at room

temperature and at 77 K which for the latter, the sample is placed in a container capable of being filled with liquid nitrogen. The system forces a current up to 20 mA through the circuit and uses a 0.55 T magnet. The resistance measurements also provide an $I-V$ diagram to make sure of the Ohmic contacts. Variable temperature Hall effect measurements have been performed in a closed cycle He 4K cryostat with a minimum temperature reaching 10 K. These measurements operate with an AC current and Hall voltage of frequency f, and a DC magnetic field. In regular AC methods, the thermoelectric voltages do not interfere with the actual Hall voltages. Although, in DC measurements temperature gradients are a source of error, but they can be eliminated by reversing the current as thermoelectric voltages do not reverse with current. Hence, subtracting the Hall voltages pertaining to different current polarities and averaging the whole set of voltages eliminates this error. An AC Hall system employs a lock-in amplifier which selects the right frequency for determination of the Hall voltage. With a reference calibration, the sign of the Hall coefficient is obtained from the phase relation between the current flowing across the sample and the Hall voltage.

3.3 Electrochemical capacitance-voltage measurements

An electrochemical capacitance-voltage (ECV) system employs an electrode-electrolyte pair in which the semiconductor of interest is used as an electrode. This experiment is capable of measuring the carrier concentration of materials, and provides a continuous electrochemical etch-measure process for the determination of the electrical properties as a function of depth [76].

A schematic of the experimental setup is shown in Fig. 3.7. As the semiconductor is placed in contact with the electrolyte, the surface conduction carriers diffuse into the electrolyte as a result of the difference in their chemical potential leading to the formation of a Schottky barrier; this phenomenon was first understood at the semiconductor-metal interface. Hence, the semiconductor-electrolyte interface ideally becomes a parallel-plate capacitor. By the application of an external bias, the width of the respective depletion layer can change which changes the

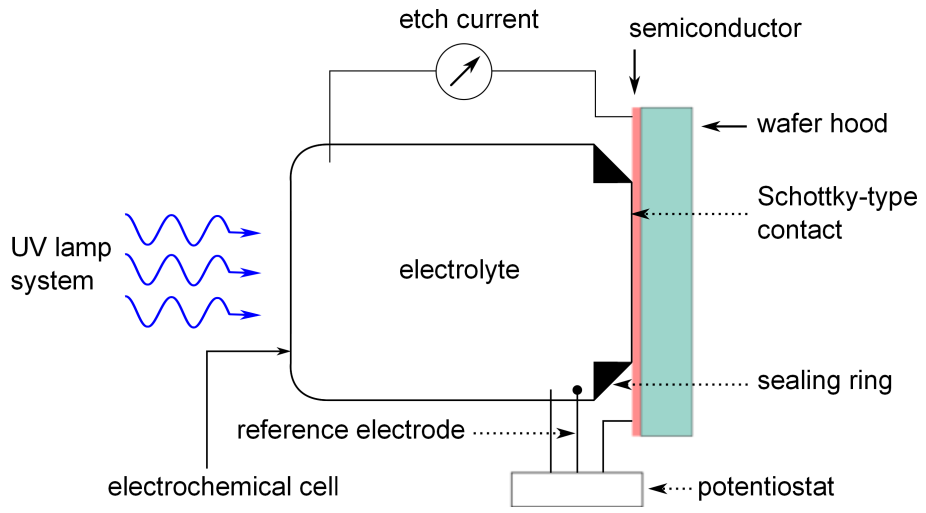

Figure 3.7: A schematic representation of the setup in an ECV measurement. The semiconductor electrode is in contact with the electrolyte forming an interface over a specific area. This interface acts as a Schottky-type contact when a reverse bias is applied. For n-type semiconductors, a UV light is used to create electron-hole pairs at the surface for etching purposes.

interface capacitance accordingly. A reverse bias increases the depletion width, and therefore, decreases the capacitance as it leads to a breakthrough, whereas a forward bias decreases the depletion width until current starts flowing, thus increases the capacitance. In ideal conditions where the depletion layer is assumed to be sharp and the semiconductor homogeneous, the applied voltage (V)-dependent interface capacitance and the carrier concentration, n, at the edge of the depletion region, could be calculated by the Mott-Schottky relations:

$$\frac{1}{C^2} = \frac{-2}{e\epsilon_0\epsilon_r A^2}\frac{V - V_{\mathrm{FB}}}{n}, \tag{3.39}$$

$$n = \frac{-2}{e\epsilon_0\epsilon_r A^2}\left[\frac{d(1/C^2)}{dV}\right]^{-1}, \tag{3.40}$$

where, e is the electronic charge, ϵ_0 and ϵ_r are the permittivity of free space and the dielectric constant of the semiconductor, respectively; A is the measurement area, and V_{FB} is the flat-band potential defined as the applied voltage at which there is no Schottky barrier in the semiconductor-electrolyte interface.

In order to etch samples, different methods are used for n- and p-type semiconductors. For an n-type film, it is illuminated by a UV source to generate electron-hole pairs in the semiconductor. The holes being subject to the intrinsic electric

field of the electrode (semiconductor)-electrolyte interface and concentration gradient, diffuse to the surface promoting recombination at the surface/interface which leads to the removal of the positively ionized atom into the electrolyte; the electrons are conducted to the interior towards the semiconductor contact. In p-type semiconductors, the already existing holes are driven from the semiconductor interior to the surface, releasing valence electrons of the semiconductor surface/interface atoms via recombination and causing the positively charged ion to dissolve into the electrolyte. An exhaustive description of the electrochemical cells and electrochemistry of such layers including the etching process can be found in Refs. [77–80]. In cases where there exists a surface electron accumulation, the holes generated by irradiation can not reach the interface as they are stopped by the surface barrier as a result of the downward band bending.

Commonly, the borders on the either side of the semiconductor-electrode interface are the points at which the chemical potential becomes equal to the values in the bulk. In a general case of metal-electrolyte contacts, the interface is known to have a *double layer* nature. The electrolyte side of the interface itself is electrochemically composed of three layers, the first two pertaining to the adsorbed and approaching solvated ions which are called the Helmholtz double layer, subdivided to the inner and outer Helmholtz layers, and the Guoy or diffuse layer which are distributed up to tens of ion diameters into the electrolyte. In the diffuse layer, the ions are not specifically adsorbed and because their concentration varies continually around and towards the bulk value, the width of this layer is an ill-defined quantity.

In semiconductor ECV measurements, the electrolyte reorders itself in the Helmholz layer to result in a clean wetting of the semiconductor surface. The thickness of this layer is usually within 1 nm and its capacitance is extremely high. This means that its contribution to the overall capacitance is negligible as it is connected in series to the Mott-Schottky and diffuse layers. The major contribution to the contact capacity comes from the Mott-Schottky layer; the diffuse layer does also have minor effects [81].

3.3.1 Simulation of the Mott-Schottky curves

By considering Eqn. 2.32, it is apparent that the first spatial derivative of the potential, $dV(z)/dz$, would appear in the solution of Poisson's equation which is related to the surface sheet density from Eqn. 2.34 as:

$$n_{\mathrm{ss}} = \frac{\epsilon_{\mathrm{s}}\epsilon_0}{e}\frac{dV(z)}{dz}\bigg|_{z=0}, \tag{3.41}$$

and the surface sheet density to the capacitance:

$$C = \frac{\Delta Q}{\Delta V} = \frac{eA\Delta n_{\mathrm{ss}}}{\Delta V}, \tag{3.42}$$

where A is the surface area of contact, and ΔV is the incremental spatial change in the band bending, V_{bb}. This method together with the model presented in section 2.2 enables the simulation of the ECV data in $C-V$ and $C^{-2}-V$ forms and deducing n and V_{bb} curves as a function of depth.

3.3.2 ECV system

The ECV measurements in this work were perfomed using a Dage Wafer Profiler CVP21 system. In order for the samples to be properly integrated into the circuit, GaIn eutectic was used to ensure ohmic contacts between the sample and the two terminals followed by an $I-V$ measurement across the sample. The electrolyte used for the SnO_2 samples was $SnCl_4$ 1M (1 mole per litre). Once the cell is filled up with the electrolyte and debubbled, an $I-V$ measurement is performed again, but this time across the electrochemical cell to ensure a Schottky-type contact. Then, the rest potential [the potential between the saturated calomel (mercury chloride) electrode (SCE) and the electrolyte interface] is measured by switching off the platinum current electrode.

The configuration is modelled by a built-in program which uses a 3-terminal equivalent AC circuit. The power dissipation, D, is calculated as:

$$D = \frac{\mathrm{Re}(Y)}{\mathrm{Im}(Y)}, \tag{3.43}$$

$$\frac{1}{Y} = R_{\mathrm{s}} + \frac{1}{G + i\omega C}, \tag{3.44}$$

where, G is the parallel conductance of the interface, and R_{s} is the serial resistance. This method calculates the capacitance per unit surface area as a function of the applied bias. This accords with the quantity derived from the simulation as can be seen in Eqn. 3.42.

3.4 X-ray photoemission spectroscopy

X-ray photoemission spectroscopy (XPS) is a technique used to investigate the chemical composition and electronic states at the surface levels of a material. XPS is based on the photoelectric effect discovered by Hertz in 1887, explained by Einstein in 1905, and developed by Siegbahn in the mid-1960's. A schematic of a photoemission process in an XPS system is shown in Fig. 3.8. As the monoenergetic X-ray photons of energy $h\nu$ release electrons from either the core or valence levels in an ionisation process, the electrons acquire a characteristic kinetic energy, E_{k}, after leaving the material:

$$E_{\mathrm{k}} = h\nu - E_{\mathrm{B}} - \phi, \tag{3.45}$$

where, E_{B} is the binding energy of the electron and ϕ is the work function of the analyser. The binding energy is the energy difference between the initial state and the Fermi level. In this work, the position of the Fermi edge of an argon ion bombarded silver (Ag) sample has been used as the binding energy reference.

Photoemission in solid-state materials is a three-stage process [82]. In the first stage, after absorbing the incident photon, the electron is excited from its initial state, ψ_i, to a final state, ψ_f, with a transition probability, Ω, described by the Fermi golden rule:

$$\Omega = | < \psi_f | H | \psi_i > |^2 \delta(E_f - E_i - h\nu), \tag{3.46}$$

where H is the Hamiltonian for the electron-photon interaction. The energy distribution of the optically excited electrons, $N(E)$, is given by:

$$N(E) = \sum_{f,i} | < \psi_f | H | \psi_i > |^2 f(E_i) \delta(E_f - E_i - h\nu) \delta(\boldsymbol{k}_i + \boldsymbol{G} - \boldsymbol{k}_f) \delta(E - (E_f - \phi)), \tag{3.47}$$

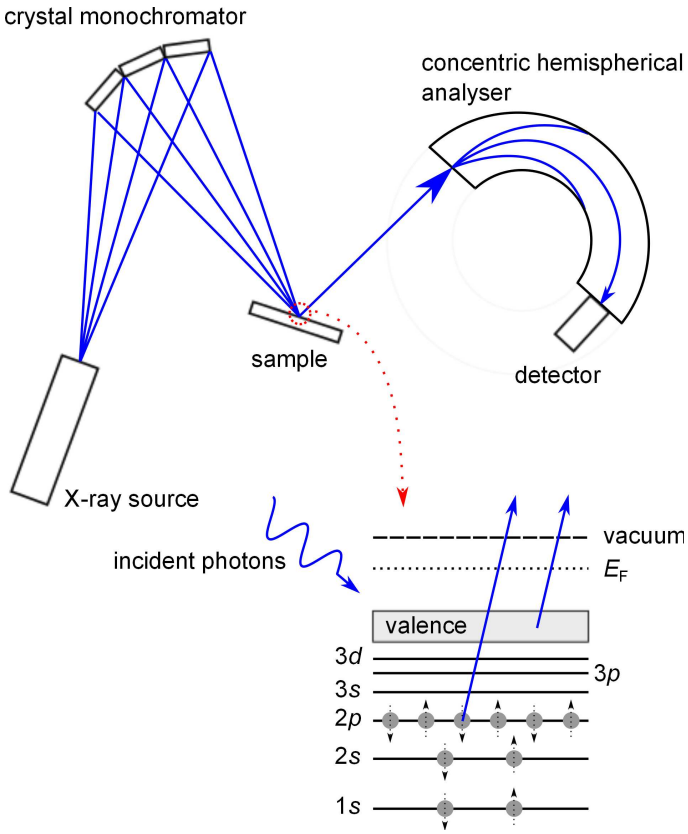

Figure 3.8: A schematic representation of a photoemission process and the electron trajectory through to the detector. Monochromated X-ray photons incident on the surface emit electrons from the core or valence levels. The energy distribution of the emitted electrons are set to be measured by the detector after making their way through the analyser.

where, $f(E_i)$ is the Fermi distribution function, and $\boldsymbol{G}$ is the reciprocal lattice vector. The conservation of energy and momentum in the transition is satified by the first and second δ-functions, respectively. The third δ-function ensures that the kinetic energy of the electron escaping the surface is the energy difference between the final state and the work function [83]. In the second stage, the photoelectron travels an energy distance until it reaches the surface of the solid. During this process, the electron may undergo inelastic scattering by other electrons, phonons, or ionized centres. This effect results in the electrons either not being able to escape the surface or not being emitted from a lower energy level than their expected initial states causing an increasing step-like background intensity towards the lower kinetic energy side (higher binding energy) of the measured spectra. The final stage is the escape of the electron from the surface provided that its kinetic energy is larger than

the surface potential barrier of the material.

The total intensity of the electrons coming from a distance, L, below the surface is described by the Beer-Lambert law:

$$I(E) = I_0(E)\exp(-L/(\lambda\sin\theta)), \tag{3.48}$$

in which, λ is the inelastic mean free path (IMFP) of the electrons, θ is the photoemission angle, and $I_0(E)$ is the initial intensity of the electrons with energy E. The IMFP can be estimated by a predictive IMFP formula, TPP-2M, for a series of materials [84].

Since the electronic configuration and bonding environment of every element are unique, the chemical composition of a sample can be determined by an XPS measurement. The intensity of the peaks also provides the relative abundance of the component elements of the material. Additionally, the position of the peaks is characteristic of the binding energies of electrons in orbitals. However, different bonding environment to an element shall cause different spectral shifts which is called a chemical shift.

3.4.1 Spectral analysis

A typical XPS scan of an SnO_2 sample is shown in Fig. 3.9. The spectrum shows many peaks pertaining to the component elements of the material which is called a survey scan. The energy position of the peaks corresponds to the collected core electrons in the elements with particular energy levels. The notation of each peak has the form, $X\,nl_j$, where X denotes the element, $n = 1, 2, 3, ...$ is the principle quantum number, $l\,(s : l = 0, p : l = 1, d : l = 2, ...)$ is the orbital angular momentum number, and $j = l \pm 1/2$ (for electrons) denotes the total angular momentum quantum number. Due to the spherical symmetry of the s-orbital ($l = 0$), no spin-orbit coupling takes place, thus the corresponding states are characterized by a single peak in the spectrum. The spin-orbit coupling causes a shift in the energy spectrum within each energy level by:

$$\Delta E_{\text{so}} \propto \xi(nl)[j(j+1) - l(l+1) - s(s+1)], \tag{3.49}$$

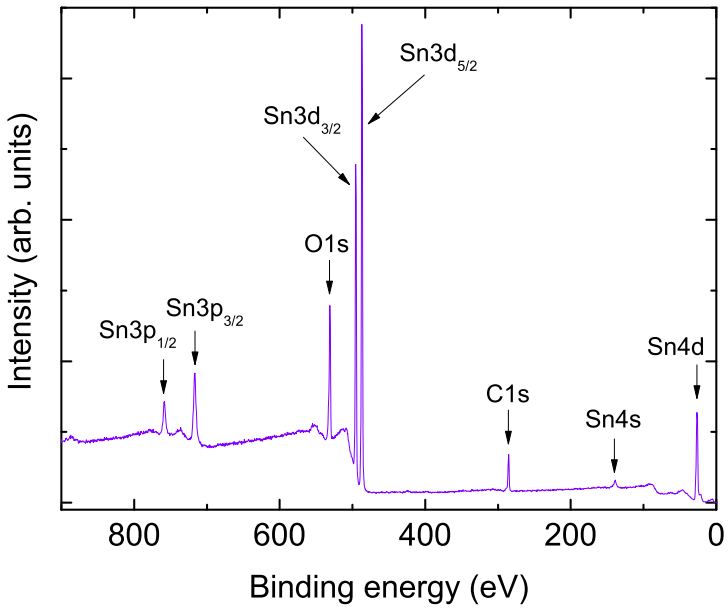

Figure 3.9: XPS wide survey scan of SnO_2 by an X-ray source with $h\nu = 1486.6$ eV. The energy peaks signify the emitted electrons belonging to the core states of the elements. The step-like background for higher binding energies is a result the inelastic scattering of the emitted electrons. The Fermi level is defined as the zero of the binding energy scale.

where $\xi(nl)$ is the spin-orbit coupling constant. The higher the total angular momentum, e.g. as that of Sn $3d_{5/2}$ relative to Sn $3d_{3/2}$ in Fig. 3.9, the lower the respective binding energy. The excitation of the conduction band surface plasmons has a marked impact on the peak shapes. The line width of the core-levels, arising from the many-body interactions and the orbital lifetimes from which the electrons recombine with the holes left behind, is Lorentzian while the instrumental broadening, arising from the finite resolution of the analyser, natural width of the light beam, and thermal broadening is described by a Gaussian function. Hence, the overall XPS core-level peaks tend to be the convolution of the Gaussian/Lorentzian profiles, namely, a Voigt lineshape. In addition to the core-electrons, the emission of the valence band photoelectrons allows the evaluation of the surface band bending of the semiconductor as it provides the energy difference between the VBM and the position of the Fermi level.

3.4.2 XPS apparatus

The XPS data used in chapter 7 was collected in an Omicron SPHERA 125 spectrometer. The samples were probed using a monochromated Al-K_α X-ray beam (1486.6 eV) of linewidth 0.25 eV. The emitted photoelectrons travel through an electrostatic hemispherical deflection analyser with a mean radius of 125 mm. The spectrometer has a large slit with a dimension, 5 mm, and two sets of 3 mm and 1 mm slits belonging to each of the 7 channeltrons. The combined experimental resolution made up of contributions from the source linewidth, analyser resolution ($\sim$0.1 eV), and thermal broadening ($\sim$0.1 eV), including electronics noise, was 0.33 and 0.47 eV for pass energies of 5 and 10 eV, respectively.

In order for the Fermi level to be set at zero for the binding energy scale, the samples were fixed on a sample plate either by using carbon tapes or via spot-welding tantalum straps over them. The prepared samples were placed in the load-lock and pumped down to $\sim 1\times10^{-8}$ mbar. Then, they were transferred to the preparation chamber where the pressure could be as low as $\sim 2\times10^{-10}$ mbar using a turbo-molecular pump (sample anealling takes place in this chamber). After preparation, the sample is transferred to the analyser chamber and mounted on a manipulator with 5 degrees of freedom which allowed measurements perfomed for different electron take-off angles. The analyser could reach a base pressure of $\sim 3\times10^{-11}$ mbar which is achieved by using a combined titanium sublimation pump (TSP) and an ion pump.

3.5 X-ray diffraction

A monochromatic X-ray beam, λ, incident on a crystal with different sets of parallel planes (atomic arrays), at an angle, θ, can give rise to constructive or destructive interference resulting from the specularly reflected rays within the crystal. Constructive interference occurs if the Bragg condition is observed, $n\lambda = 2d_{hkl}\sin\theta$. d_{hkl} is the spacing between consecutive (hkl) Miller planes, and the integer, n, is known as the order of the corresponding reflection.

In this work, X-ray diffraction is used to gauge the quality of the CdO sam-

ples [see Fig 4.3(a)], and to find the orientation of the thin SnO_2 films relative to the thick Al_2O_3 substrate. For the latter, the measurements were followed by reciprocal lattice calculations to obtain the desired lattice directions. The basis vectors, a, b, c, form the crystallographic coordinate system. Knowing the orientation of the crystal enables the reconstruction of the lengths and directions of these vectors relative to the macroscopic shape of the crystal. As the lattice vectors, a, b, c, cannot be directly accessible from an X-ray diffraction experiment, the reciprocal lattice vectors, a^*, b^*, c^* (basis vectors of the reciprocal lattice), are reconstructed first. a, b, c, and hence the orientation of the crystal can be derived using the reciprocal lattice vectors.

The monochromatic X-ray beam is scattered/diffracted by the crystal and in different directions. The theory of X-ray diffraction says that the intensities are non-zero if the condition described by the Laue equation is fulfilled, $k_1 - k_0 = 2\pi B$, where k_1 and k_0 are the wave vectors of the primary and diffracted beam, respectively, and B is the reciprocal lattice vector. Hence, by obtaining the reciprocal lattice vectors, the lattice is recognized and the basis vectors of the lattice, a, b, c, are determined.

In experiments on twinned crystals such as SnO_2/sapphire, the detected intensity is composed of that of the two crystals. A sophisticated built-in algorithm is able to recognize and separate the two reciprocal lattices in the single diffraction pattern. In some conditions where the signal from one of the crystals is very weak, the program should be informed of the expected direct lattice constants.

3.6 Transmission electron microscopy (TEM)

Ordinary optical microscopes have a fundamental limit over the image resolution due to the wave length of the optical region. The smallest distance between two points that can be resolved according to Rayleigh criterion for visible light microscopy is:

$$\delta = \frac{0.61\lambda}{n\sin\theta}, \tag{3.50}$$

where, λ is the wavelength of light, n is the refractive index of the viewing medium, and θ is the semi-angle subtended by the objective lens. $n\sin\theta$, which is often called

the numerical apperture, can be approximated to unity. Therefore, the resolution, δ, is half the wavelength of radiation. The visible wavelength ranging between $\sim$400 and $\sim$700 nm, gives a resolution limit of $\sim$200 nm which is unavailing in resolving features comparable to inter-atomic distances. In TEM, the resolution can be approximately calculated by,

$$\delta = \frac{1.22\lambda}{\theta}, \tag{3.51}$$

$$\lambda = \frac{1.22}{E^{1/2}}, \tag{3.52}$$

in which, λ and E are the wavelength and energy of the electrons, respectively. Hence, for a 100 keV electron, $\lambda \sim 0.004$ nm which is much smaller than the diameter of an atom. TEM can be used to measure the layer thicknesses, strain variations, and defect morphology in crystalline materials.

For semiconductor materials, sample preparation is the key step in TEM measurements. The thickness of semiconductor materials must be of the order of a few hundred nanometres when placed in a TEM in order to allow for sufficient electron transparency for image formation. However, the electrons may get scattered once or several times during their passage across the sample. A schematic representation of the sample preparation process is shown in Fig. 3.10. First of all, the sample should be cut into two pieces in the desired directions. The pieces are glued face to face and rubbed against each other to ensure a uniform distribution of the glue and that no bubbles are present within the added glue layer. Two silicon support blocks are attached to both sides of the sample sandwich and the whole piece is baked on a hot plate or in an oven at $\sim$200°C for one hour and then allowed to cool down. To make a flat surface on a glass slide for grinding and reduce the amount of material to be ground away in time, the specimen is cut into half along its length. The sample was ground down to several tens of microns and polished by finer grinding pads. The specimens are once again mounted on a glass slide with the other face down and ground to $\sim$15 nm followed by polishing to create a mirror finish. The final stage was to thin down the sample to attain electron transparecy by ion milling in a precision ion polisher system (PIPS). The Ar^+ ion beam is accelerated at 6 keV onto

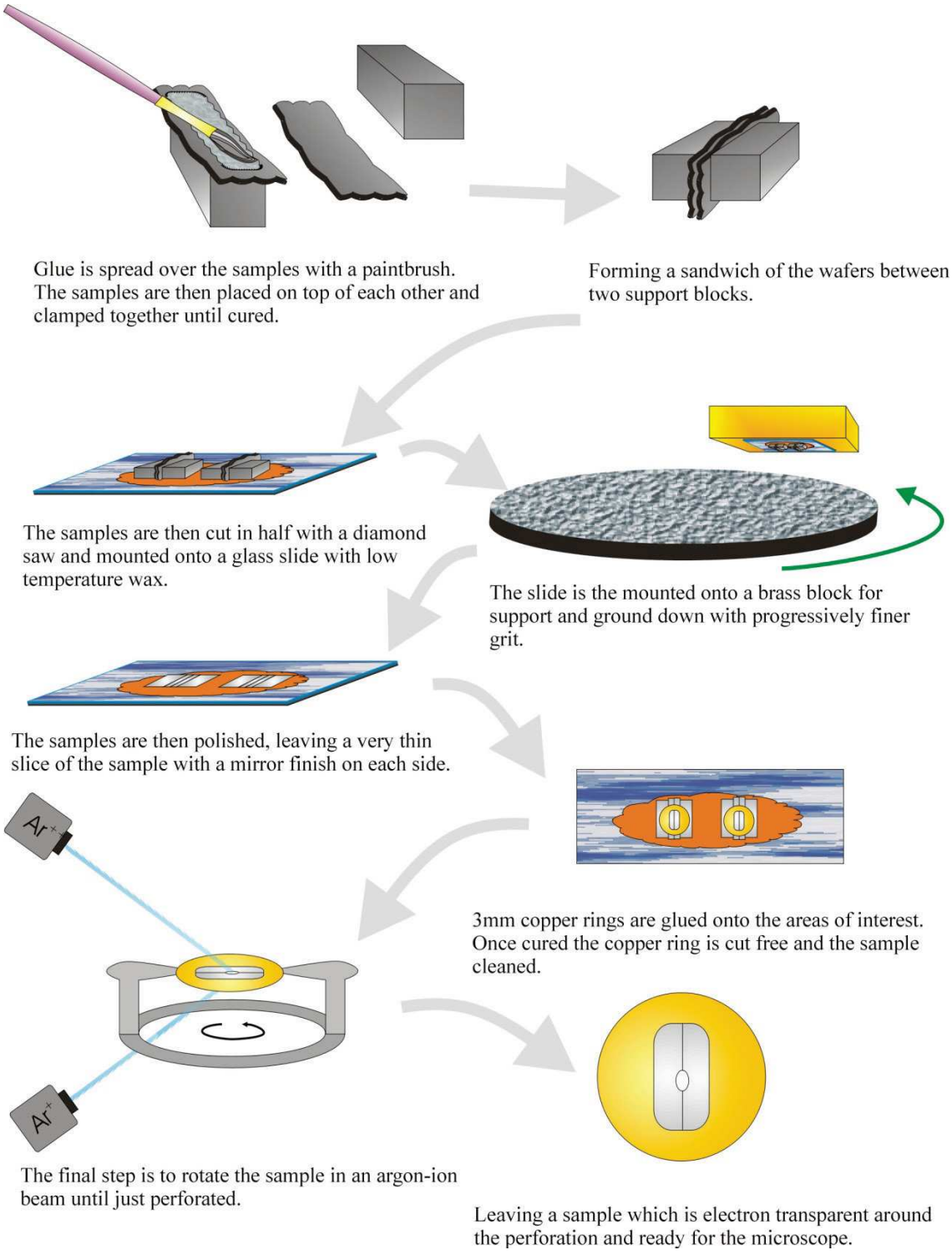

Figure 3.10: Typical steps of a sample preparation process for a cross-sectional TEM measurement [85]. This process forms one of the important stages in any semiconductor TEM measurements.

the interface of two sample pieces to perforate the specimen with an incident angle of 3° (the specimen is continuously rotated during this process). A final low-energy beam incidence at 3 keV is performed to minimize amorphous surface layers.

TEM measurements here were performed in a JEOL 2000FX system. In a TEM, electrons are produced from a heated tungsten filament and accelerated at 200 keV onto a grounded anode at the bottom of the electron gun. The column is kept under ultra high vacuum (UHV). Using condenser lenses which are magnetic pole pieces, the beam is reduced in width and intensity and collimated by a condenser aperture and directed towards the sample. After the collimated beam has passed through the sample, it undergoes an objective stage. The objective lens expands the beam to produce a magnified image. An objective lens aperture is used for choosing certain diffraction conditions; its size alters the intensity of the beam and the contrast in the image. Further lenses are employed to correct aberrations and orientate the image with respect to the sample. The image formed can be manually displaced to focus on different regions. For further information on TEM operation see Ref. [86].

Electrons that pass through the sample are partially diffracted by different crystal planes under the Bragg condition creating a diffraction pattern. Within diffraction mode, the electron beams coming from different reflections are focused onto the screen so that diffraction spots are formed representing different crystallographic planes. Tilting the sample allows diffraction from certain crystal planes. The best contrast is achieved when the correct two beam diffraction condition is acquired, the 000 spot representing the main electron beam passing straight through the sample, and only one other *hkl* spot corresponding to the desired crystallographic plane. Contrast is achieved when one of these spots is selected to produce the final image while the electrons pertaining to the other are blocked. This results in the corresponding area appearing dark in the image. In *bright field imaging*, the electrons of 000 spot are let through by the objective aperture, whereas for *dark field imaging*, those of the *hkl* diffracted spot are selected.

Dislocation contrast occurs when the displaced planes as a result of disloca-

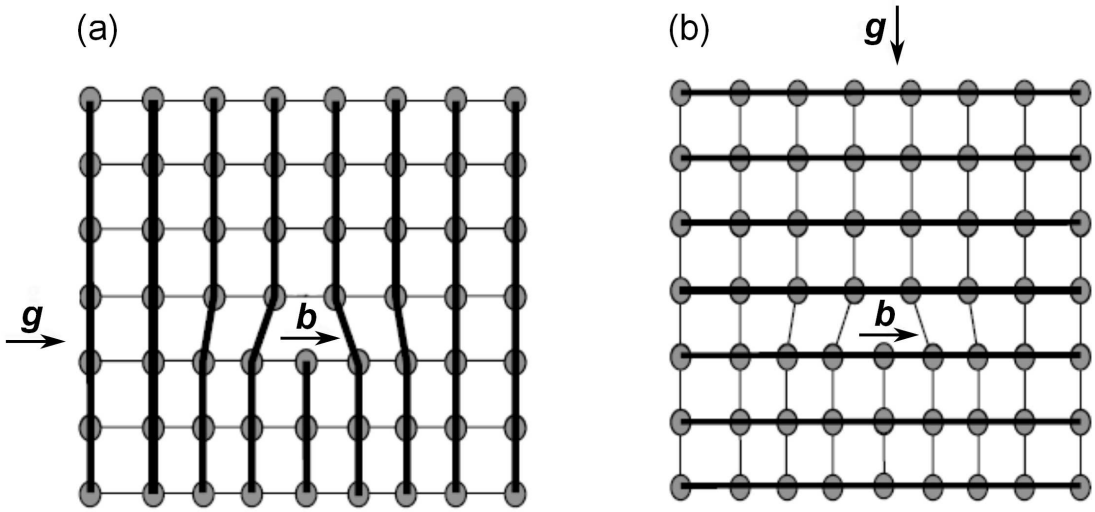

Figure 3.11: A representation of the $\boldsymbol{g}.\boldsymbol{b}$ invisibility criterion. (a) When $\boldsymbol{g}.\boldsymbol{b}=0$, the lattice distortion caused by an edge dislocation could not be visible. (b) The distortion becomes effective when $\boldsymbol{g}.\boldsymbol{b}\neq 0$ and the dislocation becomes observable.

tion occurence cause diffraction of the electron beam. Figure 3.11 illustrates this by the distortion of planes caused by dislocations as viewed along different orientations. The respective contrast is determined by the Burgers vector, $\boldsymbol{b}$, and the diffraction vector, $\boldsymbol{g}$. $\boldsymbol{g}=hkl$ is the reciprical lattice vector which refers to the hkl spot in the diffraction pattern that identifies the orientation and spacing of (hkl) planes in the crystal. The orientation of the planes or the sample and the type of dislocations determine the position of reflections. When $\boldsymbol{g}$ is perpendicular to $\boldsymbol{b}$ $(\boldsymbol{g}.\boldsymbol{b}=0)$, the dislocations are invisible; this is called the invisibility criterion. Dislocations are often formed of mixed screw and edge type, and the Burgers vector of the screw component will be at an angle to the line direction, $\boldsymbol{u}$, of the dislocation $(0^\circ \leq \theta \leq 90^\circ)$. Hence, the invisibility criterion is modified such that the dislocations are only invisible (not in contrast) if $\boldsymbol{g}.(\boldsymbol{b}\times\boldsymbol{u})=0$ and $\boldsymbol{g}.\boldsymbol{b}=0$. As these conditions cannot be satisfied simultaneously, a dislocation is considered invisible if $\boldsymbol{g}.(\boldsymbol{b}\times\boldsymbol{u})\leq 0.5$ and $\boldsymbol{g}.\boldsymbol{b}\leq 0.5$.

Chapter 4

Conduction band effective mass and electron mobility in CdO films

4.1 Introduction

Cadmium oxide (CdO) is a group II-VI semiconductor which crystallises in the rocksalt structure (space group Fm3m) as two interpenetrating face-centred cubic (fcc) lattices of cadmium and oxygen ions as shown in Fig. 4.1(a). The lattice parameter, a, is 4.695 Å [87] and each type of ion is separated from the other by $a/2$ along the <100> axes. A DFT calculated band structure for CdO using screened hybrid density functionals (HSE06) [47] is shown in Fig. 4.2. Because of the symmetry-forbidden hybridisation of the Cd 4d orbital (the manifold around -8 eV) with the O 2p orbital (the three top most valence bands) at the Γ-point (due to the high octahedral point symmetry in rocksalt CdO), the upper valence bands are repelled upward away from the Γ-point [27, 88]. Hence, the occurence of two valence band maxima at the L point and along the Γ→K (Σ) direction introduces two indirect band gaps in the band structure. The respective values range from 0.8 to 1.2 eV for the L and Γ→K (Σ) regions of the Brillouin zone [47, 89–93].

Studying carrier transport in semiconductors is of great importance, both from a fundamental level to investigate their physical phenomena, to their application in optical and electronic devices. The operation of a TCO and various other groups of semiconductors is based on the band structure-related physical quantities such as the band gap, E_g, and band edge effective mass, m_0^*, as well as the carrier collisions within the material represented by the corresponding carrier lifetimes for elastic scattering. CdO is a group II-VI TCO possessing a relatively low band gap and high bulk conductivity relative to other TCOs. Koffyberg [95] studied the Hall mobility of CdO and suggested that scattering by ionized donors may be the dom-

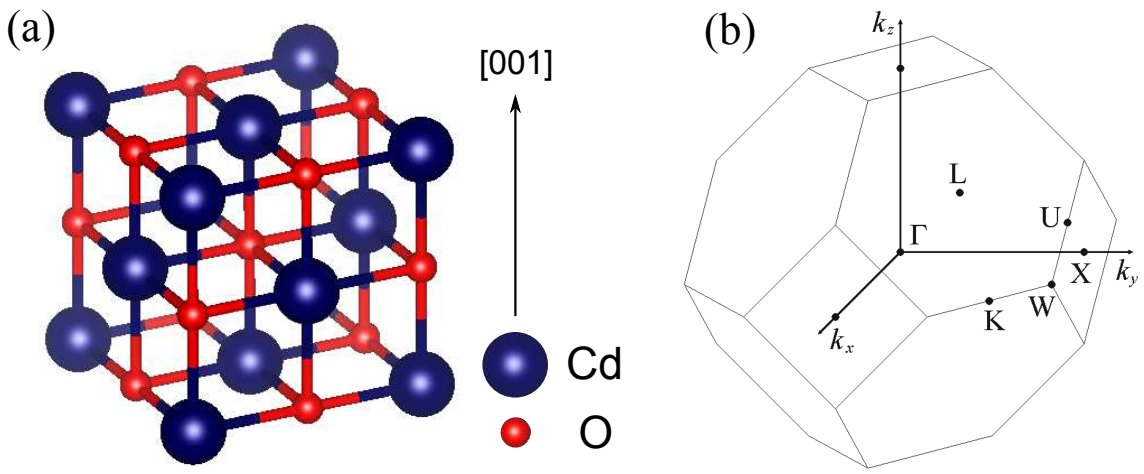

Figure 4.1: (a) Unit cell of the rocksalt structure of CdO; (b) the corresponding first Brillouin zone in a rocksalt structure.

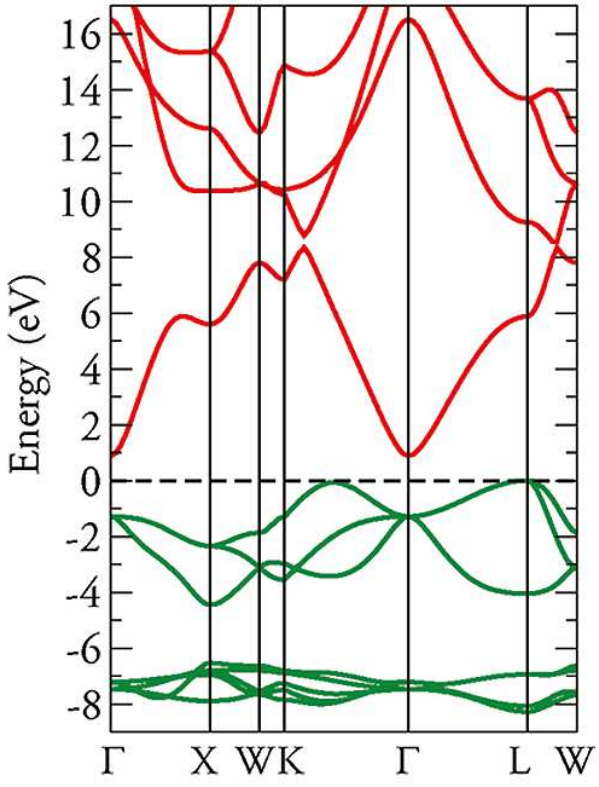

Figure 4.2: DFT-HSE06 calculated band structure for CdO [47], published after our results on the band gap and band edge effective mass of CdO [94]. The fundamental band gap across the Brillouin zone is the energy separation between the adjacent green and red bands. The valence band maxima are designated by the dashed line. This *ab-initio* analysis obtained a direct band gap of 2.18 eV for CdO which overcomes the common underestimation of the band gap within standard DFT functionals. This value agrees well with our experimental value of 2.20 eV.

inant process in limiting the mobility. Indeed, it can be deduced from the recent work by Speaks *et al.* [96] that, for carrier concentrations $\ll 5 \times 10^{20}$ cm^{-3} which corresponds to the Fermi level stabilization of CdO, donor defects are dominant.

Yan *et al.* [97] investigated the mobility of CdO samples with different Sn-doping levels (up to 11.4% of Sn) in which the effect of ionized impurity and grain boundary scattering was suggested to play the major role in electron transport. On the other hand, several authors [98–100] have studied the transport mobility by taking into account the grain boundary scattering for non-degenerate and degenerate [101] semiconductors based on Seto's model [102]. In this model, a depletion layer exists at the grain boundaries. CdO, having donor-type surface states and an electron accumulation layer [103] at the surface of grain boundaries, cannot be analysed by the approach based on Seto's model.

In this chapter, both the Fuchs-Sondheimer (FS) [104, 105] and Mayadas-Shatzkes (MS) [106] models have been applied to understand the nature of the scattering mechanisms in degenerate CdO samples. To calculate the mobility of carriers with regard to different scattering effects, the conduction band effective mass has been determined from infrared reflectance and optical absorption measurements and simulations. It is demonstrated that the ionised defect scattering dominates in the intra-grain regions and grain boundary scattering is the prevailing scattering mechanism in limiting the electron transport mobility in the CdO films. Consequently, a small increase in the grain size, especially on scales close to the mean free path in the intra-grain domains, leads to a considerable increase of the transport mobility and conductivity in epitaxial CdO.

4.2 Experimental details

In this work, CdO layers with (001) orientation were used. These were all grown on *r*-plane sapphire at close-to atmospheric pressure and growth temperatures between 308 and 405°C by metal-organic vapour-phase epitaxy (MOVPE). The precursors for oxygen and cadmium were tertiary butanol (tert-butanol) and dimethylcadmium (DMCd), respectively. The flux ratio of tert-butanol to DMCd

was kept at 10 and the precursors were transported into the reaction chamber by a purified nitrogen carrier gas [87, 107]. The optoelectronic properties of degenerate CdO have been studied for as-grown samples and after reducing the carrier concentration by prolonged annealing in vacuum at 400 and 600°C for 2 to 24 hrs. The carrier concentration of the films ranges between 2.6×10^{19} and 2.5×10^{20} cm^{-3} corresponding to a sample annealed at 600°C for 2 hrs and an as-grown sample, respectively.

Optical measurements were performed using a Bruker Vertex 70v Fourier-transform infrared spectrometer over the energy range 0.1 to 2.7 eV by the configuration illustrated in Fig. 3.3(a). Both the transmittance and reflectance of the samples were measured using an incident angle of 11 degrees with respect to the surface normal while maintaining the same optical path length. This allowed the conversion of transmission in the visible region, to absorption spectra without requiring assumptions concerning the energy dependence of the optical reflectance, as is commonly the case. Hall effect measurements, based on the standard Van der Pauw configuration, was used to obtain the sheet density, n_s, and transport mobility of the CdO samples. Both the optical and Hall effect measurements were carried out at room temperature (RT).

X-ray diffraction (XRD) and atomic force microscopy (AFM) measurements were performed, both before and after annealing, for structural characterization. Figure 4.3(a) shows a typical XRD scan of the CdO films grown on r-plane $(01\bar{1}2)$. The scan is dominated by the CdO$(00l)$ reflections showing the high crystallinity of the films. The full width at half maximum (FWHM) of the CdO 002 rocking curve was in the range of $0.27 - 0.29^\circ$ for the investigated samples, indicating a threading dislocation density of the order of $2-4\times10^9$ cm^{-2} [108,109] as described on p. 67, section 4.3.3. This indicates that the density of dislocations in the CdO samples is independent of the annealing treatment performed after growth. In the AFM images [e.g. Fig. 4.3(b)], grains several hundreds of nanometers in size were observed [87].

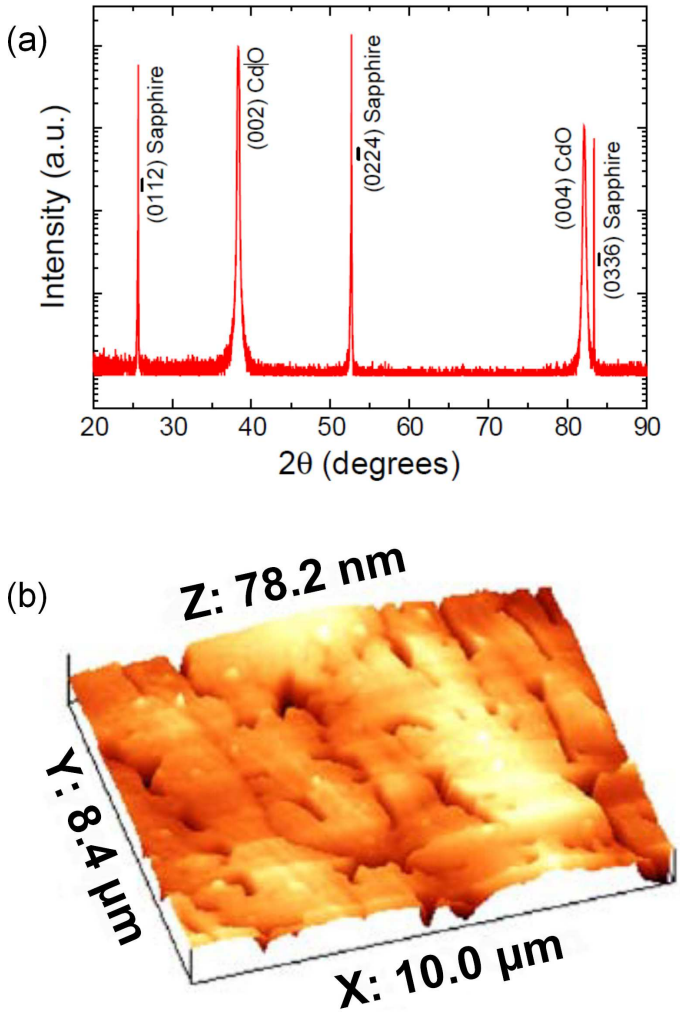

Figure 4.3: (a) XRD θ-2θ scan of a CdO(001) film grown on r-sapphire at 308°C by MOVPE [87]. The CdO 00l reflections signify the high crystallinity of the films. (b) AFM image of a CdO(001) film grown on r-sapphire at 383°C [87]. Boundary areas several hundred nanometers apart are apparent at the surface.

4.3 Data, simulation and analysis

4.3.1 Band gap and band edge effective mass

Infrared (IR) reflectance data of epitaxial CdO on r-plane sapphire within an energy range of 100 to 900 meV for three different carrier concentrations is shown in Fig. 4.4. The energy corresponding to minimum reflectance, which is related to the conduction band plasma resonant energy, increases with carrier concentration. In order to model the spectra, a three layer stratified medium (vacuum/CdO/sapphire) with coherent interference has been considered as shown in Fig. 4.5. The two os-

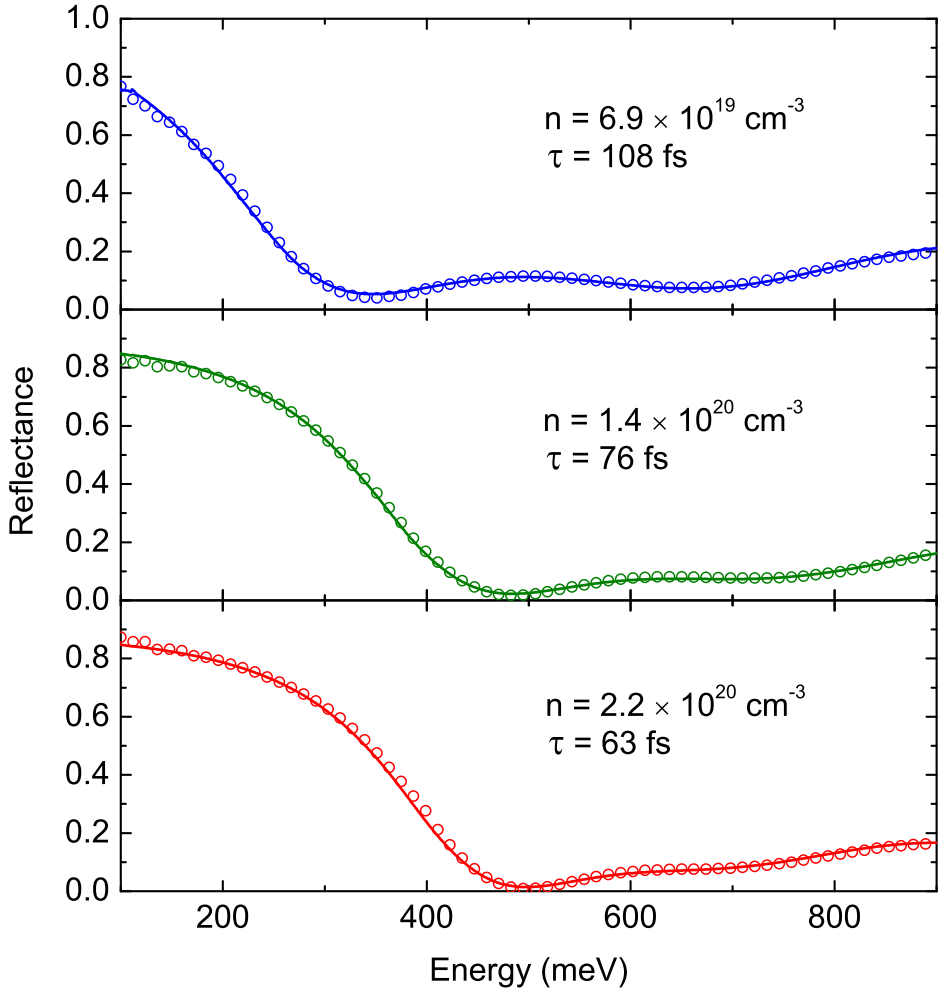

Figure 4.4: Mid-IR reflectance spectra (open circles) and respective simulations (solid lines) of three CdO samples with different carrier concentration. The optical lifetime, as the reciprocal of plasmon damping, decreases with carrier concentration and this is apparent in the broadening of the plasma edge.

cillator model has been used for the complex dispersive dielectric function for CdO layers:

$$\tilde{\epsilon}(\omega) = \tilde{n}^2(\omega) = \epsilon(\infty) + \frac{(\epsilon(0) - \epsilon(\infty))\omega_{\mathrm{TO}}^2}{\omega_{\mathrm{TO}}^2 - \omega^2 - i\omega\gamma_{\mathrm{TO}}} - \frac{\epsilon(\infty)\omega_{\mathrm{p}}^2}{\omega(\omega + i\gamma_{\mathrm{p}})} = \tilde{\epsilon}_{\mathrm{ph}}(\omega) + \tilde{\epsilon}_{\mathrm{e}}(\omega), \quad (4.1)$$

where $\tilde{n}$ is the index of refraction, $\epsilon(\infty)$ and $\epsilon(0)$ are high frequency and static dielectric constants respectively; ω_{TO} and γ_{TO} are the transverse optical phonon frequency (energy) and damping, respectively; ω_{p} is the plasma frequency (energy) and γ_{p} is the plasmon damping being the inverse of carrier lifetime. For the optical response of the sapphire substrate, the factorized model with Lorentzian broadening

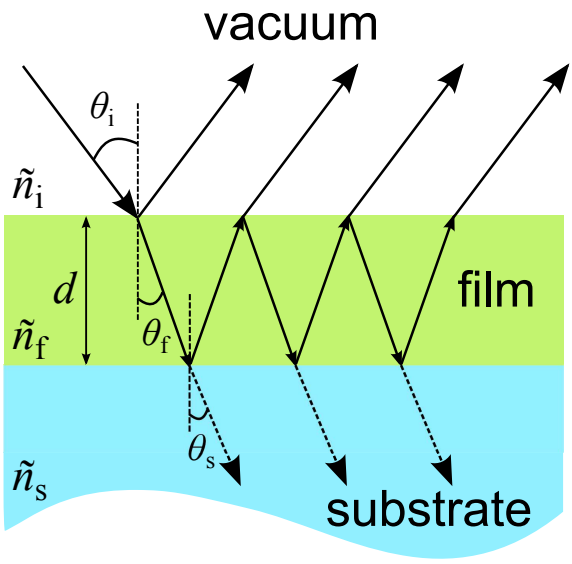

Figure 4.5: Reflection in a three layer stratified medium (vacuum/CdO/sapphire substrate) with coherent interference. The sapphire substrate is taken as a semi-infinite bulk.

has been applied [110]:

$$\tilde{\epsilon}(\omega) = \epsilon(\infty) \prod_{i}^{l} \frac{\omega_{\mathrm{LO},i}^2 - \omega^2 - i\omega\gamma_{\mathrm{LO},i}}{\omega_{\mathrm{TO},i}^2 - \omega^2 - i\omega\gamma_{\mathrm{TO},i}}, \tag{4.2}$$

where ω_{LO} and γ_{LO} are the longitudinal polar optical phonon mode and damping, respectively. The high frequency dielectric constant, $\epsilon(\infty)$, for CdO was set to 5.3 [111] which is consistent with a recent investigation of optical constants of CdO over a range of energies [112]. The high frequency dielectric constant of 3.06 was used for sapphire [113]. Simulation of the data, as shown in Fig. 4.4, allowed the determination of the plasma resonant energy and broadening, and the film thickness, d. The carrier concentration of the samples was calculated via, $n = n_s/d$, which varies between 2.6×10^{19} and 2.5×10^{20} cm^{-3}.

The plasmon energy values plotted as a function of carrier concentration for as-grown and post-growth annealed CdO samples are shown in Fig. 4.6 along with respective model curves for three different values of the band edge effective mass using the following equation:

$$\omega_p^2 = \frac{ne^2}{\epsilon_0\epsilon(\infty)\langle m^*\rangle}, \tag{4.3}$$

where n is the free carrier concentration; $\epsilon(\infty)$ and ϵ_0 are the high frequency dielec-

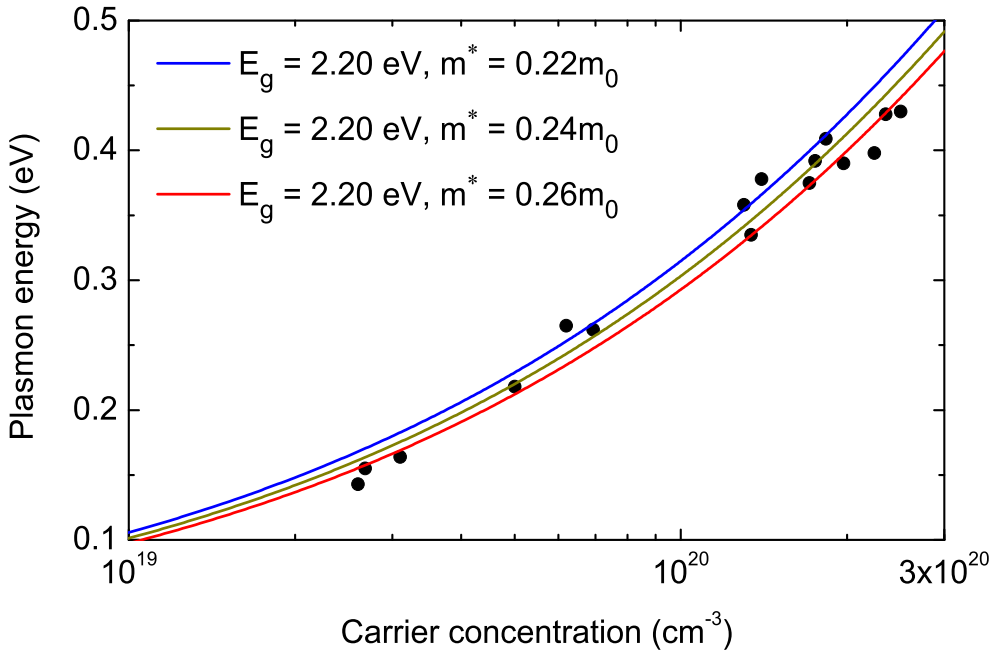

Figure 4.6: Plasmon energy as a function of carrier concentration for as-grown and post-growth annealed CdO films. The points are obtained through mid-IR reflectance simulations and the solid lines from model calculations using a band gap of 2.20 eV and three different band edge effective mass values, $0.22m_0$, $0.24m_0$, and $0.26m_0$.

tric constant and the permittivity of free space, respectively, and $\langle m^* \rangle$ is the average electronic effective mass. As the CdO films are degenerate (the Fermi level lies in the conduction band), the non-parabolicity of the conduction band has been taken into account within a 2-band $\boldsymbol{k}.\boldsymbol{p}$ model. The effective mass of the electrons becomes dispersive and energy dependent. Hence, the effective mass has been density-of-states averaged over the occupied states:

$$\langle m^*(E_\mathrm{F}) \rangle = \frac{\int m^*(E) g(E) f(E, E_\mathrm{F}) dE}{n(E_\mathrm{F})}, \tag{4.4}$$

where

$$m^*(E) = \frac{m_0^*}{E_\mathrm{g}}(2E + E_\mathrm{g}), \tag{4.5}$$

$$n(E_\mathrm{F}) = \int g(E) f_\mathrm{FD}(E, E_\mathrm{F}) dE, \tag{4.6}$$

$g(E)$ and $f_\mathrm{FD}(E, E_\mathrm{F})$ are the density of states and Fermi-Dirac functions, respectively.

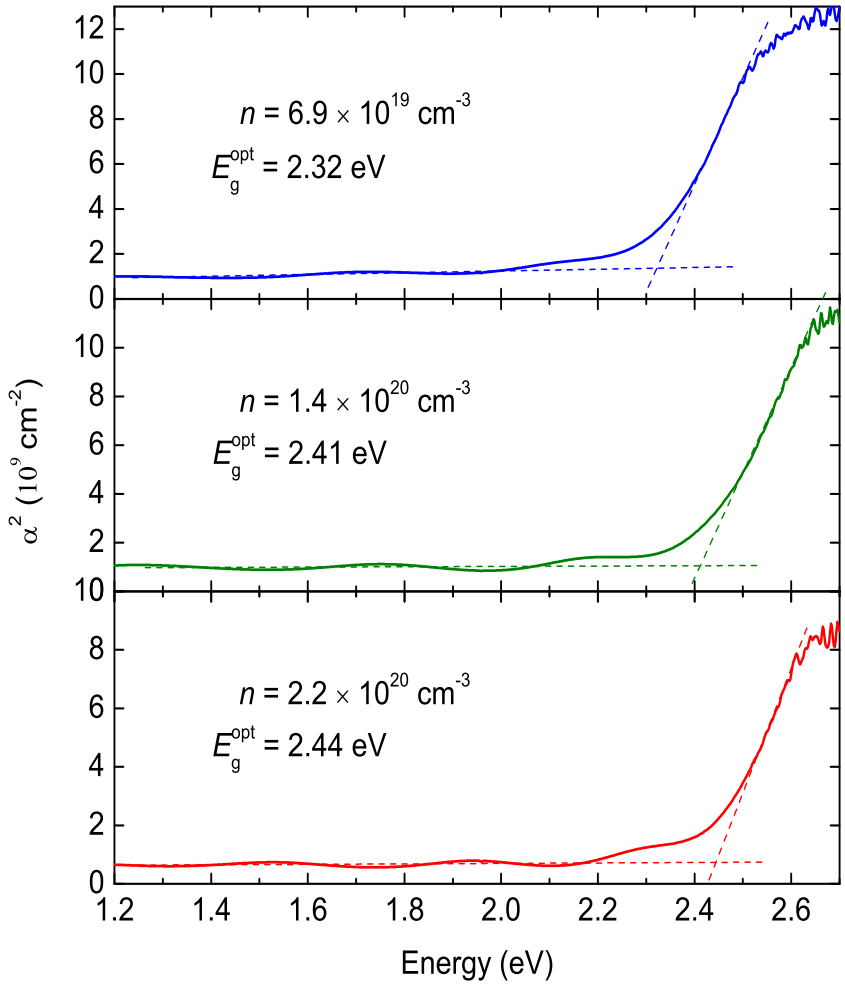

Figure 4.7: Optical absorption in the visible/ultraviolet region for three CdO films. The absorption edge is determined through the extrapolation of the sharp optical absorption onset and baseline of the spectra. It is apparent that the sharp transitions from the valence band to the Fermi level occurs at higher energies for films with higher carrier concentrations.

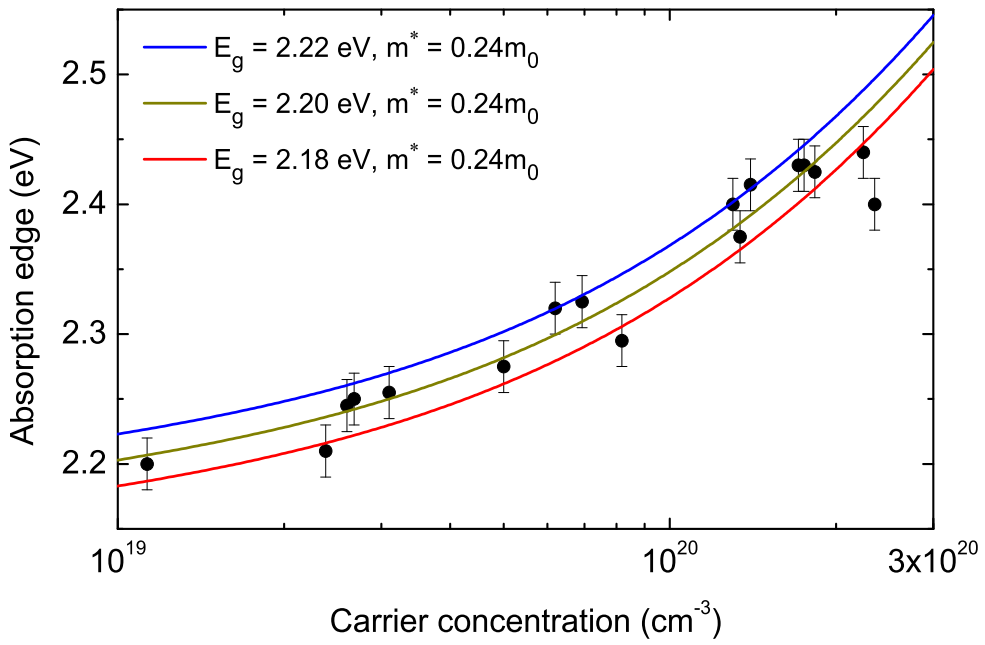

Figure 4.8: Optical band gap in the visible/ultraviolet region for as-grown and post-growth annealed CdO films. The data points are determined by calculating the absorption coefficient using measured reflection and transmission spectra, and the solid lines are model curves taking into account the non-parabolicity of the conduction band, Burstein-Moss shift, and band gap renormalization. Three band gap values have been used with a single value of the band edge effective mass.

As the band gap is an input parameter for obtaining the model curves in Fig. 4.6, absorption measurements have been performed to obtain the optical gap values for each film with different carrier concentration. The results are shown in Fig. 4.7 for the same three samples as in Fig. 4.4. The absorption edge is determined by the interception of the line extrapolated along the sharp absorption onset with the baseline (background absorption) of the spectra. As can be seen in the figure, the interband transition energy increases with carrier concentration.

The optical band gap plotted as a function of carrier concentration is shown in Fig. 4.8. Model calculations represented by the solid lines have been performed interactively with those pertaining to plasmon energy versus carrier concentration as represented in Fig. 4.6. The band filling effect (Burstein-Moss shift) and band gap renormalization have been accounted for in the absorption edge simulations, assuming a non-dispersive valence band near the Γ-point as the energy dispersion

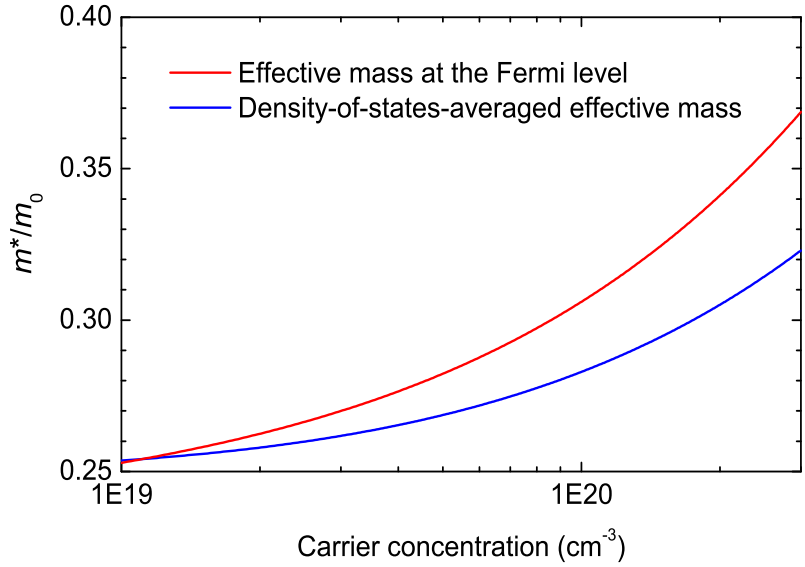

Figure 4.9: The conduction band electron effective mass to free electron mass ratio calculated as a function of carrier concentration in CdO. It shows the increasing trend of the energy-dependent effective mass at the Fermi level relative to the density-of-states-averaged value for a non-parabolic conduction band in CdO with a band gap and band edge effective mass values of 2.20 eV and $0.24m_0$, respectively.

within the k-space region of interest is negligible [114]:

$$E_{\mathrm{g}}^{\mathrm{opt}} = E_{\mathrm{g}} + \Delta E_{\mathrm{BM}} + \Delta E_{\mathrm{BGR}}, \tag{4.7}$$

where, E_{g} is the fundamental band gap at RT, ΔE_{BM} is the Burstein-Moss shift, and ΔE_{BGR} is the band gap renormalization composed of the effects of electron-electron and electron-ion interactions in the lattice; the latter has been introduced in section 2.1.7. Three model curves have been obtained in Fig. 4.8 using band gap values of 2.18, 2.20, and 2.22 eV and a value of $0.24m_0$ for the band edge effective mass.

By analysing the evolution of the plasmon energy and optical absorption edge with carrier density, the fundamental band gap and band edge effective mass at RT were found to be 2.20±0.02 eV and $0.24\pm0.02m_0$, respectively. These values are similar to the results of an earlier investigation by Jefferson *et al.* [115] which included some of the same samples investigated here. The small differences are attributed to the larger range of bulk carrier densities and the more accurate determination of

the absorption coefficient utilized in this study. Using the band gap and band edge effective mass of CdO obtained above, the electron effective mass in the conduction band is plotted as a function of carrier concentration in Fig. 4.9. The figure shows the variation of the electron effective mass at the Fermi level as compared to the density-of-states-averaged value in a non-parabolic conduction band of CdO.

4.3.2 Optical mobility

The optical mobility of each sample has been calculated using optical carrier lifetime and the density-of-states-averaged effective mass for the conduction electrons, $\langle m^* \rangle$, according to the equation, $\mu_{opt} = e\tau/\langle m^* \rangle$. The broadening of the plasma edge obtained from mid-IR reflectance simulations has been used to determine the optical carrier lifetime, τ. The results for optical mobility as a function of carrier concentration are plotted in Fig. 4.10 which show that the optical mobility varies between ~ 209 cm^{2}V^{-1}s^{-1} for the highest and ~ 1116 cm^{2}V^{-1}s^{-1} for the lowest carrier concentrations. With increasing carrier concentration, the broadening of the plasma edge increases as seen in Fig. 4.4 which corresponds to the reduction of the optical carrier lifetime. This phenomenon causes the optical mobility to decrease with carrier concentration as shown in Fig. 4.10.

The degenerate form of the Brooks-Herring formula [116–118] has been used to simulate the ionized defect scattering-limited mobility of the samples as a function of carrier concentration [119]:

$$\mu_{\text{ion,deg}} = \frac{24\pi^3(\epsilon_s\epsilon_0)^2\hbar^3 n}{e^4 <m^*>^2 \; Z^2 N_i \left[\ln[1+y(n)] - \dfrac{y(n)}{1+y(n)}\right]}, \tag{4.8}$$

where

$$y(n) = \frac{2(3n\pi^8)^{1/3}\hbar^2\epsilon_s\epsilon_0}{e^2 <m^*>},$$

where $<m^*>$ is the density-of-states-averaged effective mass, and N_i is the density of ionized defects. The highest Fermi energy of the samples investigated is ~ 0.48 eV above the CBM while the Fermi level stabilization energy or charge neutrality level (CNL) of CdO lies 1 eV above the CBM [96]; this is schematically shown in Fig. 4.11. Therefore, N_i in Eqn. 4.8 has been approximated by the density of ionized donors.

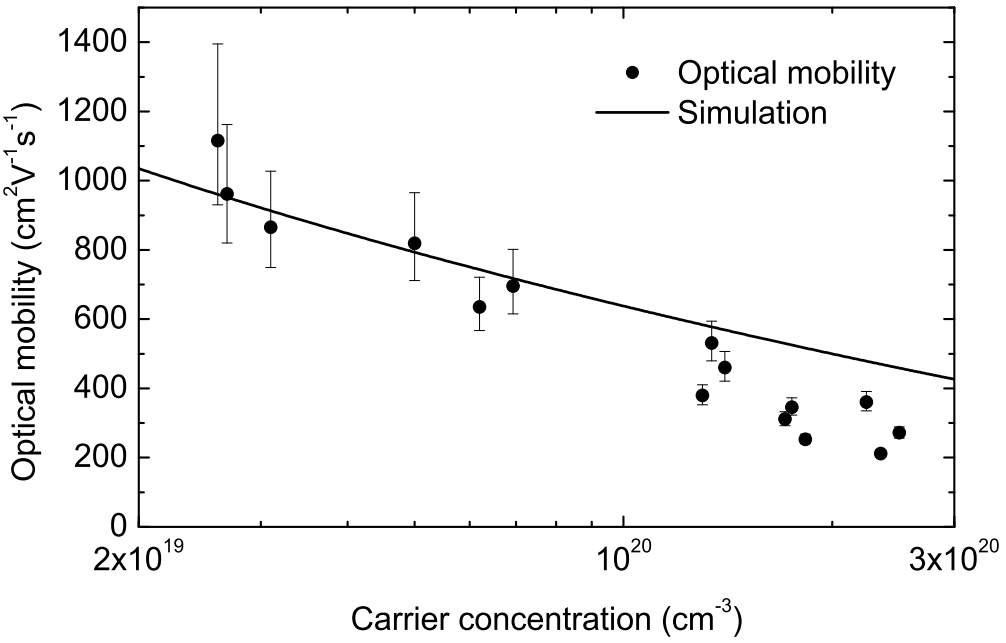

Figure 4.10: Optical mobility of CdO and simulation of the ionized defect scattering-limited mobility. The increase in the density of ionized defects results in an increase of the scattering centres as well as the carrier concentration. Therefore, the optical mobility is expected to decrease with carrier concentration in the intra-grain regions as is apparent in the graph.

The ionized donors have been assumed to be singly charged [47]. The simulation of the optical mobility data points is represented in Fig. 4.10. The results show that ionized defect scattering is the dominant scattering mechanism reducing the optical mobility in degenerate CdO at RT. The effect of lattice scattering on the mobility was found to be negligible. The ionized defect scattering-limited mobility curve in the case of doubly charged donors would not reproduce the data points as it decreases the mobility curve to well below the data points.

4.3.3 Transport mobility

The transport mobility of degenerate CdO samples measured by the Hall effect varies between $\sim$ 20 and 125 $cm^2V^{-1}s^{-1}$ for carrier concentrations in the range of 2.5×10^{20} and 2.6×10^{19} cm^{-3}. Figure 4.12 compares the optical mobility to the transport mobility of the electrons in CdO films. It is apparent that the transport mobility is significantly lower than the optical mobility of the electrons for all the

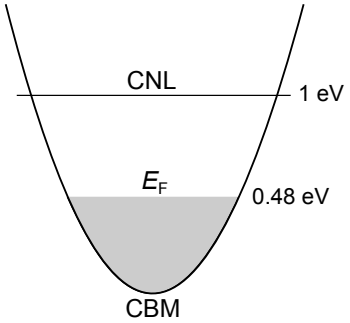

Figure 4.11: Relative positions of the Fermi level and the charge neutrality level with respect to the conduction band minimum in CdO. The CNL still lies well above the Fermi level of the film with the highest carrier concentration, indicating that the possibility of acceptor formation in the samples is negligible.

samples. Therefore, during Hall effect measurements of the transport mobility, the conduction electrons must experience one or more additional scattering mechanisms. While during transport measurements the electrons traverse the film in response to the applied bias, optical excitation during IR reflectance results in no such phenomenon. This suggests that grain boundary scattering and/or surface scattering are responsible for the transport mobility being much lower than the optical mobility. This interpretation is justified by the following quantitative modelling of these electron scattering mechanisms.

Commonly, the effect of grain boundaries on carrier transport mobility has been studied based on inter-grain barriers resulting from boundary trap states which are indicative of depletion layers at the boundaries. Simulation of the transport mobility under such conditions is based on the model proposed by Seto [102] for non-degenerate semiconductors. Under the same boundary conditions with degenerate intra-grain characteristics, the modified expression for grain boundary scattering-limited mobility incorporating Fermi-Dirac statistics has been used [101]. This predicts that the transport and optical mobility will merge as the barrier becomes surmountable by increasing the carrier concentration and therefore the Fermi level [120]. However, as can be seen in Fig 4.12, the two sets of data points do not merge at higher carrier concentrations. This suggests that the approach to grain boundary scattering is not appropriate for use here.

Indeed, previous investigations have shown that CdO has a significant surface

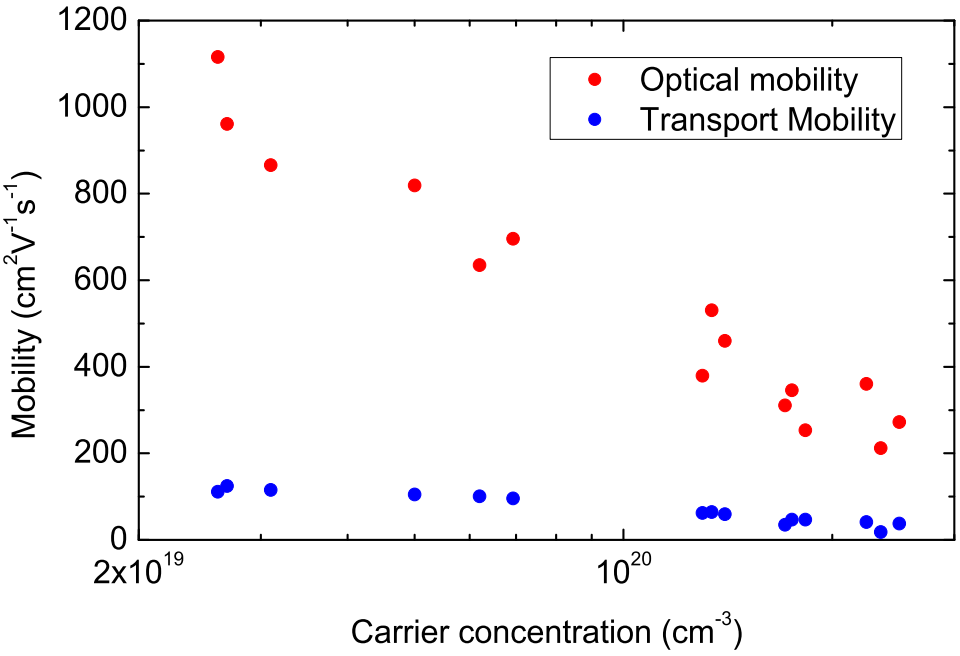

Figure 4.12: Experimental optical mobility compared to transport mobility as a function of carrier concentration. A significant lowering of the mobility is observed for each sample in the case of transport where electrons traverse the film. Optical excitations produce collective oscillations within the intra-grain regions, where the scattering effect of grain boundaries, the surface and interface are not inflicted on the electronic motion.

electron accumulation layer [103]. Therefore, we expect that there exists an electron accumulation at the grain boundaries and dislocation lines within the films. This has been implemented in the modelling of the grain boundary scattering. In order to simulate the transport mobility of the CdO samples, additional scattering mechanisms, namely, grain boundary and surface scattering have been considered by making use of the MS model [106] together with the FS theory of scattering at surfaces which apply to a degenerate electron gas [104, 105]. It is worthy of mention that from the analysis of the optical absorption and mid-IR reflectance data, it is apparent that there exists a B-M shift for all the CdO samples investigated, indicating the relevance of considering the conduction electrons as a degenerate electron gas. This feature and the aforementioned electron accumulation make these models applicable to simulate the data.

Firstly, the effect of surface scattering has been modelled according to the

equation [105]:

$$\mu_{ss} = \mu_0 \left(1 - \frac{3}{2k}(1-p)\int_1^\infty \left(\frac{1}{t^3} - \frac{1}{t^5}\right)\frac{1-e^{-kt}}{1-pe^{-kt}}dt\right), \tag{4.9}$$

where μ_0 is the bulk mobility, k is the ratio of film thickness, d, to the mean free path of the electrons in the intra-grain domains, l, and p is the fraction of the electrons being scattered specularly from the surfaces. The bulk mobility has been taken to be the ionized defect scattering-limited mobility as deduced from the optical mobility analyses. The average film thickness has been determined to be $\sim$ 480 nm from mid-IR simulations. The mean free path in the bulk for each sample has been calculated according to the equations:

$$< l(E) > = < v(E) >< \tau(E) >, \tag{4.10}$$

$$< v(E) > = \frac{\int v(E)g(E)f(E, E_F)dE}{\int g(E)f(E, E_F)},$$

$$v(E) = \frac{\hbar k(E)}{m^*(E)},$$

where $< v(E) >$ is the density-of-states-averaged energy-dependent electron velocity, and $< \tau(E) >$ is the energy-averaged relaxation time obtained from mid-IR simulations. The average mean free path over the samples has been determined to be $\sim$ 35 nm. The respective model curves, in which the limiting effect of diffuse collisions at the surfaces, $p = 0$, is compared to that of 50% specular reflection, are shown in Fig. 4.14. The result implies that collisions at the surfaces, either diffuse or specular, would not result in a considerable change to the optical mobility. This is because the average mean free path within the grains is much smaller than the thickness of the films.

Figure 4.13 represents the grain boundaries as N parallel planes oriented perpendicular to the electric field and the surface of the film. In the MS model, a Gaussian distribution of planar grain boundaries as δ-function potentials is used with an average spacing. Boltzmann's equation is solved for this configuration including a relaxation time, τ, corresponding to the intra-grain scattering mechanisms. Surface scattering is included by applying the surface boundary conditions on the electron

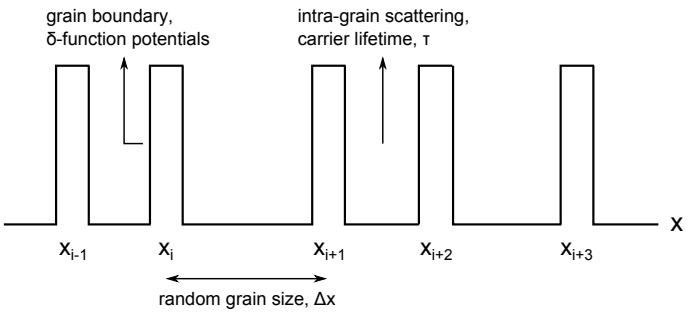

Figure 4.13: A schematic of randomly spaced grain boundaries or dislocations in one direction, x, parallel to the surface of the film in the Mayadas-Shatzkes model [106]. Each boundary is represented as a δ-function potential with strength, S. τ is the carrier lifetime in the intra-grain region refering to scattering effects other than those coming from grain, surface, and interface boundaries.

distribution function [104]. Thus, the following relation has been computed to model the transport mobility which takes into account the intra-grain, surface, and grain boundary scattering [106]:

$$\mu_{\rm tr} = \mu_{\rm gs} - \frac{6\mu_0}{\pi k}(1-p)\int_0^{\pi/2} d\phi \int_1^{\infty} \frac{\cos^2\phi}{G^2(t,\phi)} \times \left(\frac{1}{t^3} - \frac{1}{t^5}\right) \frac{1-e^{-ktG(t,\phi)}}{1-pe^{-ktG(t,\phi)}} dt, \quad (4.11)$$

in which,

$$\mu_{\rm gs} = \mu_0 \left[1 - 1.5\alpha + 3\alpha^2 - 3\alpha^3 \ln\left(1+\alpha^{-1}\right)\right], \quad (4.12)$$

$$G(t,\phi) = 1 + \alpha/[\cos\phi(1-t^{-2})^{1/2}],$$

$$\alpha = (l/g)[R/(1-R)],$$

where $\mu_{\rm gs}$ is the grain boundary scattering-limited mobility, g is the average lateral grain size, R is the fraction of the electrons being reflected from grain boundaries.

From XRD data, the FWHM of the CdO 002 rocking curve was in the range of $0.27 - 0.29^\circ$ for the investigated samples. The threading dislocation density has been calculated to be of the order of $2 - 4 \times 10^9$ cm^{-2} [108, 109, 121] according to:

$$\Gamma^2 = K_{\rm dis} + K_{\rm str}\tan^2\theta, \quad (4.13)$$

$$N_{\rm dis} = \frac{K_{\rm dis}}{4.35b^2}, \quad (4.14)$$

where Γ is the average FWHM of the 002 rocking curves in radians, $K_{\rm dis}$ and $K_{\rm str}$

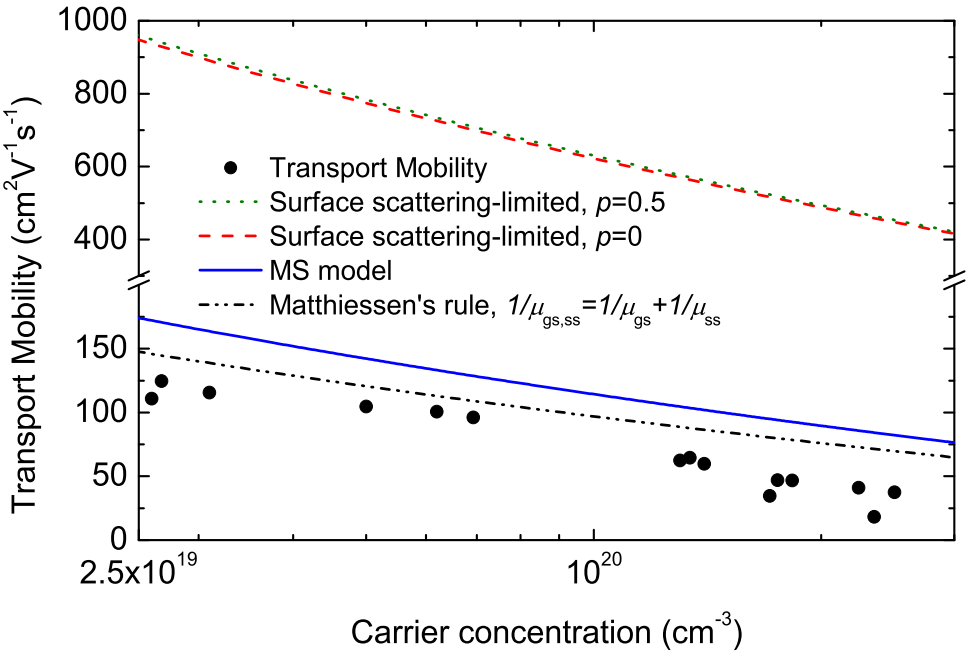

Figure 4.14: Transport mobility of CdO and simulation via the MS model along with the application of Matthiessen's rule to grain boundary and surface scattering-limited mobilities; the effect of surface scattering alone using FS theory is represented which shows the minor influence of surface scattering on the transport mobility. The error bars of the data lie within the solid points.

are parameters related to the dislocation density and strain, respectively, N_{dis} is the dislocation density, and b is the length of Burger's vector approximated by the lattice parameter. As the thickness of the samples is $\sim$0.5 μm, the effects of strain have been neglected. Assuming a homogeneous and isotropic dislocation distribution, this density results in a dislocation every 200 nm along the two perpendicular in-plane $\langle 100 \rangle$ directions using the relation $h = 1/\sqrt{N_{\text{dis}}}$ where h is the dislocation occurence with dimension L. Furthermore, this typical length is consistent with the AFM images, in which grains several hundreds of nanometers in size are observed [see Fig. 4.3(b)]. Therefore, a length of 200 nm has been used as the average separation of the δ-function potential barriers considered as the lateral grain dimension within the MS model. Simulation of the transport mobility using the combined three scattering mechanisms in the MS model, Eqn. 4.11, are shown in Fig. 4.14. A high reflection coefficient of $R \sim 0.95$ at the boundaries is required to obtain a model curve consistent with the measured mobilities. The negligible contribution of surface

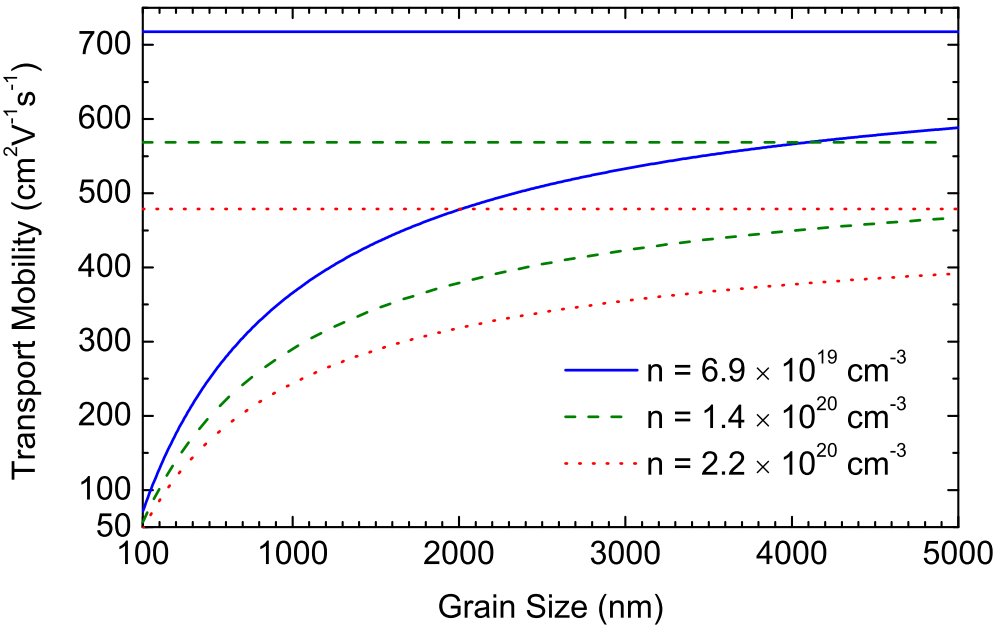

Figure 4.15: Modelling of the transport mobility as a function of grain size for three CdO samples with different carrier concentrations and a reflection coefficient, $R = 0.95$. Intra-grain (optical) mobilities for respective carrier concentrations are represented by horizontal lines. As the grain size increases, the influence of grain boundary scattering decreases, therefore, the transport mobility approaches the optical mobility.

scattering on the transport mobility is apparent in the figure.

The result of applying Matthiessen's rule to separately calculated both the surface and grain boundary scattering-limited mobilities, via Eqns. 4.9 and 4.12, is represented in Fig. 4.14. The curve shows a slight deviation from that of the MS model which is caused by the fact that the bulk scattering mechanism is incorporated within the calculations of the FS and MS models. In any case, it is apparent from the modelling results that grain boundary scattering is the dominant mechanism in limiting the transport mobility.

The variation of the transport mobility with grain size, predicted from the modeling, is represented in Fig. 4.15 for three different carrier concentrations. It is apparent that, as the grain size increases, the transport mobility tends to the bulk mobility within the grain. The mobility rises more steeply with increasing grain size when the grain size is low and closer to the bulk mean free path. So a large improvement of transport mobility is expected for a slight increase from the current

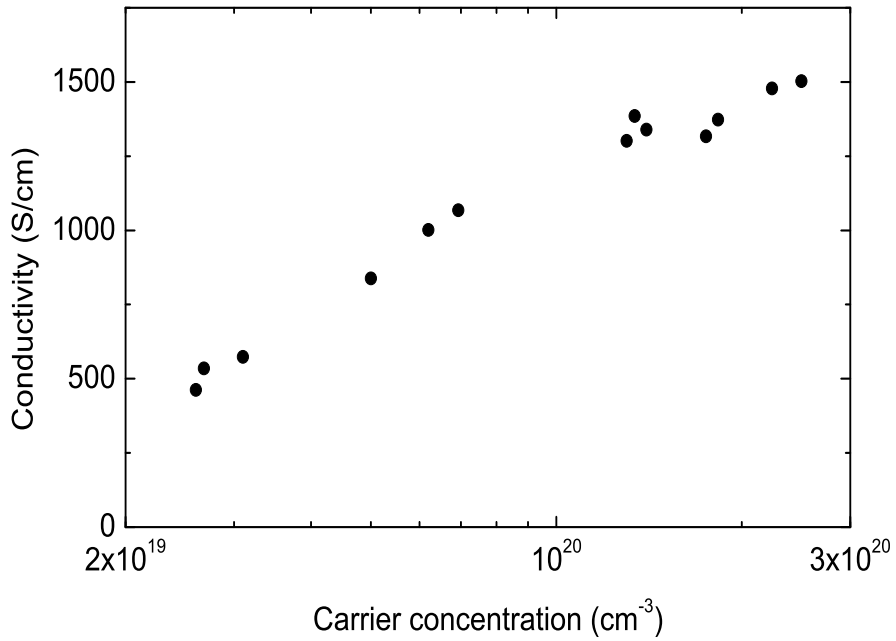

Figure 4.16: Conductivity data as a function of carrier concentration. This data is for CdO films grown by MOVPE with an average grain size of 200 nm. The conductivity increases by a factor of 3 for an order of magnitude increase in the carrier concentration for this grain size.

grain size, with the rate of improvement diminishing as the grain size becomes much greater than the mean free path. This indicates that small improvements in the growth will have a relatively large effect on the mobility of the CdO films.

Finally, it should be noted that for higher carrier concentrations, the measured mobilities deviate somewhat from the model curves, as can be seen in Figs 4.10 and 4.14 for optical and transport mobilities, respectively. As the formation energy of acceptors decreases and that of donors increases as the Fermi level increases towards the charge neutrality level [96, 103], the density of acceptors may no longer be negligible. Therefore, at high carrier densities, in addition to the ionized donors reducing the mobility, there may also be ionized acceptors acting as scattering centers. This partial compensation behaviour, as previously observed for InN [122], would account for the deviation at high carrier density from the model curves in which only donors have been taken into account.

The conductivity of the CdO films has been plotted in Fig. 4.16, ranging between 462 and 1503 S/cm for carrier concentrations between 2.6×10^{19} and

Table 4.1: Comparison of the transport properties of undoped and doped CdO films grown by different growth techniques.

Growth method	substrate	dopant	n (cm^{-3})	μ ($cm^2V^{-1}s^{-1}$)	σ (S/cm)	g (nm)	d (nm)
MOVPE*	r-sapphire	U/D	2.5×10^{20}	38	1520	200	~ 480
IBS[1] & SP[2] [123]	glass	U/D	$\sim 10^{20}$	12-15	200-500	$\times 10$	500
DCRMS[3] [124]	PET	U/D	6.21×10^{20}	19.2	1838	–	120-164
ARE[4] [125]	glass	U/D	2×10^{20}	125	2500	200	100
DCRMS [126]	glass & Si	U/D	2.35×10^{20}	100.48	3773	22(CS)	177.5
PLD[5] [97]	glass	Sn	3.2×10^{20}	27	1460	200-500?	>500
	MgO(100)	Sn	2.7×10^{20}	330	15000	200-500?	>500
	MgO(111)	Sn	4.7×10^{20}	609	42000	200-500?	>500
MOCVD[6] [127]	glass	Sn	3.34×10^{21}	11.3	7143	–	–
RS[7] [128]	glass	Cu	$\sim 10^{20}$	3.2	106	–	243
	glass	In	$\sim 10^{20}$	2.3	189	–	281
MOCVD [129]	glass	Y	$\sim 5.5 \times 10^{20}$	~ 105	~ 8540	200	–
	MgO(100)	Y	$\sim 8 \times 10^{20}$	~ 130	~ 17800	200	–
	glass	Sc	$\sim 4.5 \times 10^{20}$	~ 80	~ 6000	–	–
	MgO(100)	Sc	$\sim 7 \times 10^{20}$	~ 175	~ 18000	–	–
	glass	In	$\sim 9.5 \times 10^{20}$	~ 70	~ 10500	–	–
	MgO(100)	In	$\sim 1.5 \times 10^{21}$	~ 125	~ 20000	–	–
SG[8] [130]	glass	Al	3.2×10^{20}	54	2810	500	1700
MOCVD [131]	MgO(100)	Ga	$\sim 8 \times 10^{20}$	~ 85	11500	–	~ 200
SG [132]	glass	F	–	–	2222	~ 310	190
SGDC[9] [133]	glass & Si	F	1.13×10^{21}	60.41	10880	500	1500

*This study; [1]Ion-Beam Sputtering; [2]Spray Pyrolysis; [3]DC Reactive Magnetron Sputtering; [4]Activated Reactive Evaporation; [5]Pulsed Laser Deposition; [6]Metal-Organic Chemical Vapour Deposition; [7]Reactive Sputtering; [8]Sol-Gel; [9]Sol-Gel Dip Coating; U/D stands for undoped, and CS for crytallite size.

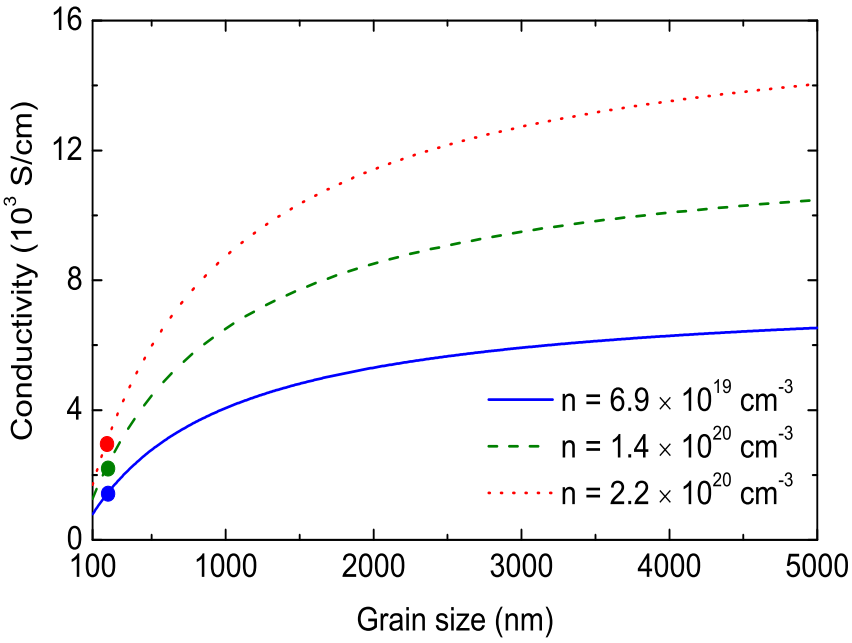

Figure 4.17: Conductivity model curves as a function of grain size calculated for three CdO films with different carrier concentrations. The filled circles on each curve denote the grain size of the films investigated, namely, 200 nm. The increase in conductivity with grain size is more pronounced for higher carrier concentrations.

2.5×10^{20} cm^{-3}. The average grain dimension is 200 nm as obtained from the analyses above. The variation of the conductivity of the films as a function of grain size is plotted in Fig. 4.17 for three films with different carrier concentration based on the calculated carrier mobility model curves and using $\sigma = ne\mu$. The points on the curves specify the current grain size of the films, i.e., 200 nm. The figure shows that the conductivity significantly improves with increasing grain size and being more appreciable for higher carrier concentrations.

A comparison between some of the effective physical quantities in carrier transport for different growth mechanisms of CdO films have been shown in table 4.1. The lowest and highest conductivity values of the films are obtained by Cu and Sn doping, respectively. The lowest and highest values for an undoped sample are 200 and 3773 S/cm corresponding to carrier concentrations $\sim10^{20}$ and 2.35×10^{20} cm^{-3}, respectively. The investigated samples in this study (grown by MOVPE) range between the reported values for undoped CdO; the grain size of the

reported values has not been explicitly specified. Studies of ZnO [134–136] (both *p*- and *n*-type) and SnO_2 [55] films show that the highest undoped conductivities achieved for these films are still well below the lowest value for CdO. For example, In_2O_3 [137] could have an undoped conductivity relatively comparable to that of CdO; a conductivity of 500 S/cm is reported for a carrier concentration of 1.3×10^{20} cm^{-3}. Hence, undoped degenerate CdO films would prove to be well suitable for highly-conductive transparent materials applications.

4.4 Summary and conclusions

Electron mobility in degenerate CdO thin films grown on *r*-sapphire has been studied as a function of carrier concentration. MIR reflectance together with Hall effect measurements have been used to determine the carrier concentration, plasmon energy and lifetime in the CdO films. The results from optical absorption and plasmon energy as a function of carrier concentration were simulated by applying carrier statistics calculations to determine the band gap and the conduction band edge effective mass. The band gap and band edge effective mass of the conduction electrons in the degenerate CdO films have been determined to be 2.20 eV and $0.24m_0$ at RT, respectively.

The"optical" mobility has been calculated from the conduction band plasmon lifetime. The values range from ∼209 to 1116 $cm^2V^{-1}s^{-1}$ for carrier concentrations ranging between 2.5×10^{20} and 2.6×10^{19} cm^{-3}. Ionized defect scattering has been observed to be the dominant mechanism limiting the intra-grain mobility of CdO layers at RT. The transport mobilities obtained from the Hall effect measurements range between ∼20 and 125 $cm^2V^{-1}s^{-1}$ which are significantly lower than the optical mobilities. Since the optical scattering of electrons is confined within the intra-grain regions of the films, the dramatic decrease in the transport mobility was studied in terms of surface and grain boundary scattering as the additional mechanisms experienced by the electrons when traversing the film. Surface scattering was modelled by considering both specular and diffuse scattering at the top and bottom surfaces of the CdO films. The commonly used models of grain boundary scattering for

simulation of the transport mobility were not applicable to CdO as they assume a depletion layer at the grain boundaries. Given that CdO has a surface accumulation layer, which implies that electron accumulation is expected to take place at dislocations and grain boundaries, the effect of grain boundary scattering was simulated by a model which determines the fraction of the electrons being reflected at the grain boundaries.

As the calculated bulk mean free path of the electrons was small compared to the film thickness, surface scattering was not a significant mobility reducing mechanism. Instead, scattering at grain boundaries was shown to be the prevailing mechanism reducing the electron transport mobility. The simulation results of the transport mobility shows that transport scattering takes place with $\sim$95% reflection of the electrons at the grain boundaries. The extracted plots of mobility and conductivity show that, if the grain size of the CdO layers could be increased, electron transport would be significantly improved, leading to better conduction in transparent electrode applications.

Chapter 5

Temperature dependence of direct band gap and transport properties of CdO

5.1 Introduction

Binary metal oxides such as SnO_2, In_2O_3, ZnO, Ga_2O_3, and CdO are well known for exhibiting concurrent transparency and conductivity, making them suitable for use as transparent electrodes in a variety of applications. Among these compounds, CdO has a fairly low direct band gap with a tendency for being degenerately n-type which enhances its transparency and gives it a high conductivity. It has recently been recognised as a potentially ideal transparent conductor for use in photovoltaics [138]. However, there has been no investigation of the temperature-dependence of the direct band gap of CdO or determination of the 0 K fundamental direct band gap and band edge effective mass of CdO, in spite of many reports of these quantities at RT.

In some of the earliest investigations of CdO, the direct band gap at RT was reported to be $\sim$ 2.3 eV [90] and electron effective mass in the range 0.1–$0.3m_0$ [89, 90, 139]. Another highly cited band gap value of 2.28 eV which was measured at 100 K [93] is often compared with RT absorption edge or optical gap data [129, 140]. More recently, RT values of 2.16 eV and $0.21m_0$ for the zero-carrier-density direct band gap and band edge effective mass, respectively, have been reported from analysis of transmission, infrared reflectance and Hall effect data from MOVPE-grown CdO, taking into account the non-parabolicity of the conduction band and band gap renormalization [115]. When the visible reflectance was also measured and used in the calculation of the absorption spectra, these values were subsequently revised, in chapter 4 of this thesis, to 2.20 eV and $0.24m_0$ [94], very close to the zero carrier density, RT values of 2.22 eV and 2.23 eV previously

derived from measurements of CdO films grown by sputtering [141] and pulsed laser depostion (PLD) [142]. Slightly higher RT band gap values of 2.3 eV and 2.4 eV have also been reported recently for CdO thin films also grown by PLD [138, 143].

The experimental uncertainty over the true value of the RT band gap is caused mostly by the degeneracy of the CdO films, with nominally undoped samples typically having carrier densities in excess of 10^{19} cm^{-3} and the associated band filling-induced Burstein-Moss shift of the absorption edge. In addition, the fact that the band edge effective mass and high frequency dielectric constant vary with carrier concentration, due to band gap renormalization, complicates the analysis of optical and transport data. These latter effects have not been considered in the previous RT studies.

In contrast to the experimental studies, theoretical studies of the band gap of CdO have attempted to determine the 0 K value. Due to the well-known band gap problem of density functional theory, the majority of theoretical reports significantly underestimate the direct band gap of CdO, with values as low as 1.04 eV having been reported [144]. However, more recent studies using hybrid functional methods obtained larger values of 1.81 eV [27] and 2.18 eV [47].

Here, an experimental study is presented to determine the fundamental direct band gap and band edge effective mass of CdO, taking into account the variations with carrier concentration as well as temperature by an analysis of the plasma resonant energy and optical energy gap. This analysis enables the Varshni parameters and Bose-Einstein oscillator model parameters to be determined for these single crystal films of CdO and to describe the variation of the band gap with temperature.

5.2 Experimental details

Single crystalline CdO(001) films were grown on *r*-sapphire by MOVPE as described in chapter 4 (Refs. [87, 107]). Samples were annealed in ultrahigh vacuum at 400 or 600°C for between 30 and 60 minutes to obtain samples with a range of carrier concentrations. Variable-temperature Hall effect measurements were performed

Table 5.1: RT carrier concentration results for three particular CdO samples.

sample	carrier concentration (cm^{-3})
A	1.13×10^{19}
B	2.38×10^{19}
C	8.19×10^{19}

in the Van der Pauw configuration. Variable temperature mid-infrared and visible reflectance and transmittance measurements at an incident angle of 11° relative to the surface normal were performed using a Bruker Vertex 70v Fourier-transform infrared (FTIR) spectrometer. The carrier concentration obtained for three samples at RT are shown in table 5.1.

5.3 Data, simulation, and analysis

The evolution of the absorption spectra with temperature for sample B is shown in Fig. 5.1. A shift of the absorption edge to lower energy with increasing temperature is apparent. The absorption spectra were calculated from the measured transmission and reflectance data. The inset in Fig. 5.1 compares the absorption spectra for the three samples all with different carrier concentrations at 100 K. The absorption edge shifts to higher energies and more band tailing is seen as the carrier concentration increases. Fig. 5.2 shows the absorption edge energy or optical gap of the three CdO films as a function of temperature. The data points were obtained by linear extrapolation of the sharp absorption onset to the base line portion of the α^2 versus energy curve.

The solid lines in Fig. 5.2 are model curves obtained by self-consistent simulations of the optical gap as a function of temperature. The simulations have been performed by model carrier statistics calculations within the $\boldsymbol{k}.\boldsymbol{p}$ model taking into account the non-parabolicity of the conduction band [57], the B-M shift, the effects of band gap renormalization, band gap shrinkage with temperature [145], and temperature variations of the Fermi level. A flat valence band has been assumed as the dispersion within the k-space region of interest is negligible [114]. A schematic

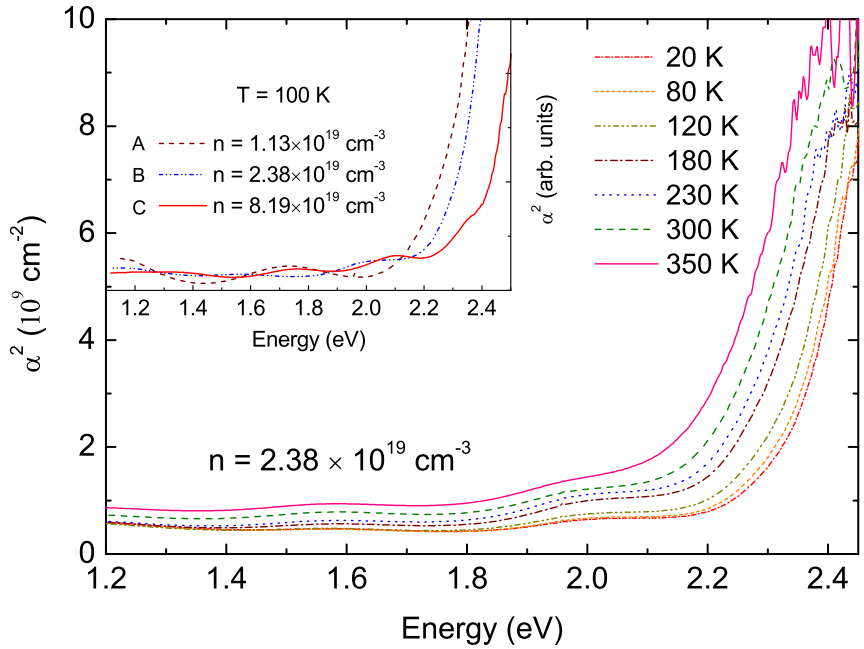

Figure 5.1: Absorption spectra as a function of temperature for sample B, a CdO film with n=2.38×10^{19} cm^{-3}. Inset: absorption spectra for samples A, B and C at 100 K.

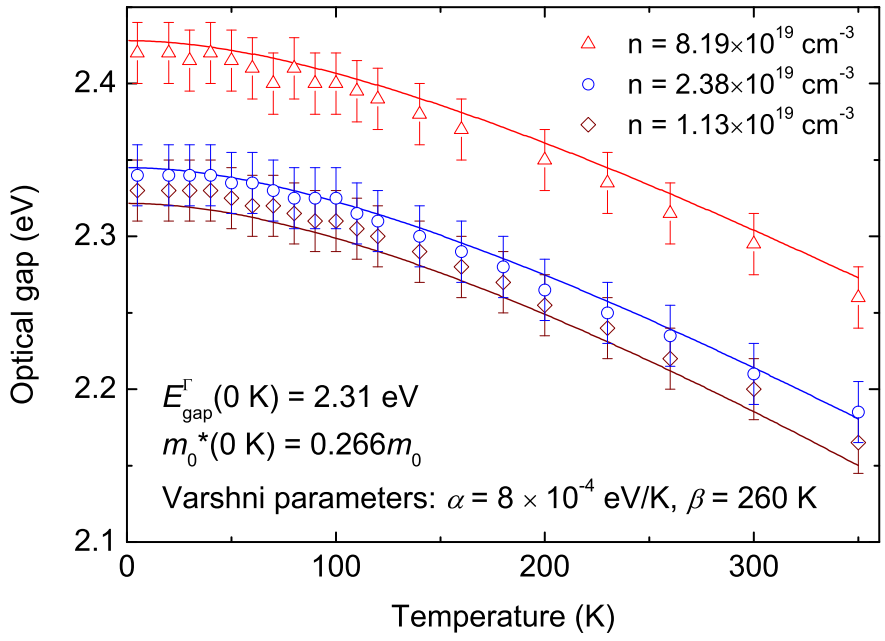

Figure 5.2: Absorption edge energy or 'optical gap' as a function of temperature for the three CdO films with different carrier concentrations. The points are experimental data and the lines are model calculations. The optical gap decreases with temperature with Varshni parameters, α=8×10^{-4} eV/K and β=260 K. The 0 K fundamental band gap and band edge effective mass used in the model in the limit of zero carrier density are 2.31 eV and 0.266m_0, respectively.

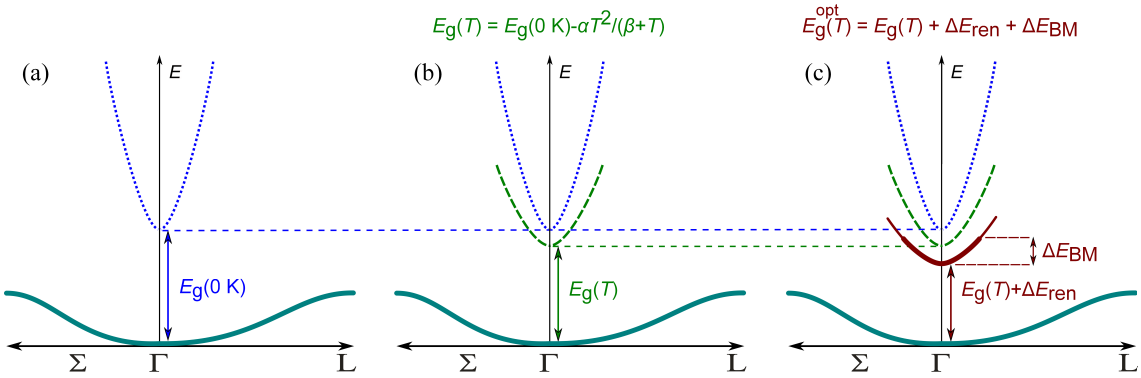

Figure 5.3: Schematic representation of the band structure close to the Γ-point in CdO, illustrating the phenomena that influence the band gap and band edge effective mass: (a) an empty conduction band at 0 K; (b) an empty conduction band undergoing a band gap reduction due to temperature effects; and (c) the effects of conduction band filling (ΔE_{BM}) and band gap renormalization (ΔE_{ren}). The former directly influences the latter with the high free electron densities leading to increased B-M shift of the band edge and larger reduction of the band gap due to many body interactions. The resulting gap for allowed interband transitions defines the temperature-dependent optical edge, $E_{\mathrm{g}}^{\mathrm{opt}}(T)$, at non-zero wavevectors.

representation of the various physical effects involved in the band structure and considered in our model is shown in Fig. 5.3. Fig. 5.3(a) shows the Γ-point band structure for zero carrier concentration at 0 K. The fundamental direct band gap and band edge effective mass for this situation is what is being determined from modelling of data from real CdO samples as a function of temperature with different carrier densities. Fig. 5.3(b) shows the band gap reduction due to the increase of temperature and the resultant effects of lattice expansion and electron-phonon coupling. This is most commonly parameterized by the equation [145],

$$E_{\mathrm{g}}(T) = E_{\mathrm{g}}(0) - \frac{\alpha T^2}{\beta + T} \tag{5.1}$$

where α and β are the Varshni parameters. The additional effects of band filling (B-M shift) and band gap renormalization are illustrated in Fig. 5.3(c). Hence, the difference between the fundamental band gap and optical gap is clearly apparent in this figure.

In order to incorporate the Fermi level variations with temperature in the model, variable-temperature Hall effect measurements were performed to determine the carrier density in the CdO films. Fig. 5.4 shows the carrier concentration and

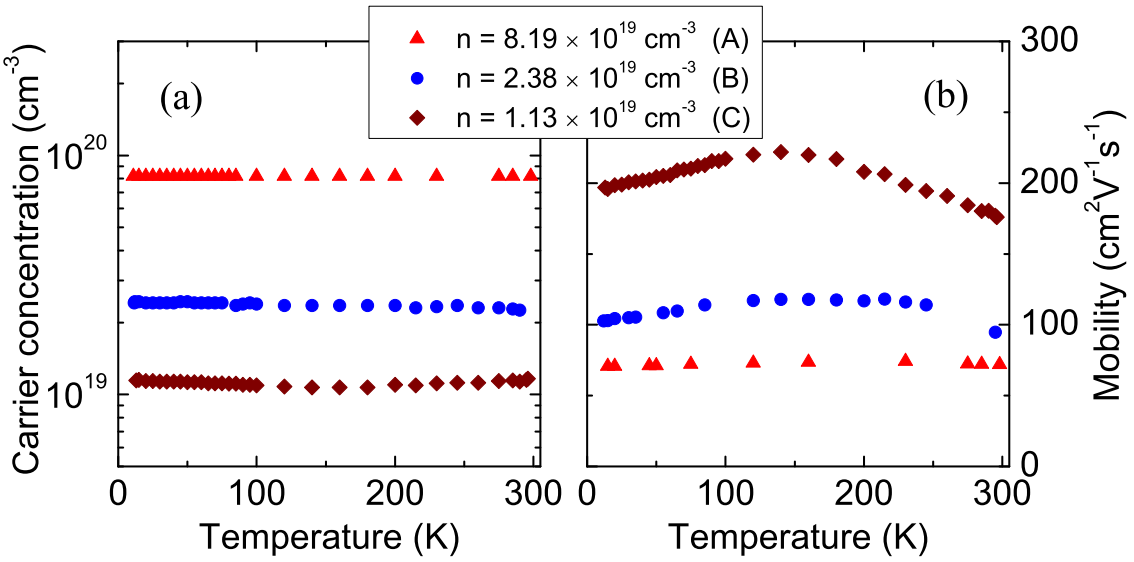

Figure 5.4: (Color online) Carrier concentration (a) and mobility (b) as a function of temperature for three CdO samples.

mobility of the three samples from 10 to 300 K. As is apparent in Fig. 5.4(a), the carrier concentration is unchanged with temperature for the different samples, as expected for the case of a degenerately doped semiconductor. Hence, applying the degeneracy of the conduction band to the model, the Varshni parameters [145] governing the temperature variations of the band gap of CdO are extracted to be α=8×10^{-4} eV/K and β=260 K; β is a parameter proportional to the Debye temperature.

While the carrier concentration is temperature-independent, Fig. 5.4(b) shows that the mobility varies as a function of temperature. For lower carrier concentrations, the mobility follows the well-known bell-shape with respect to temperature, while it flattens out as the carrier concentration of the films increases. For lower carrier concentrations, the initial increase in the mobility on heating to 150 K comes from a decrease in scattering by dislocations (grain boundaries) [94], $\mu_{\mathrm{disl}} \propto T$, and the decrease in mobility above about 150 K is due to the well-known phonon scattering.

The zero-carrier-concentration at 0 K band edge effective mass and its variations with temperature and carrier concentration were input parameters in the optical gap modelling. Hence, a parallel simulation was conducted containing re-

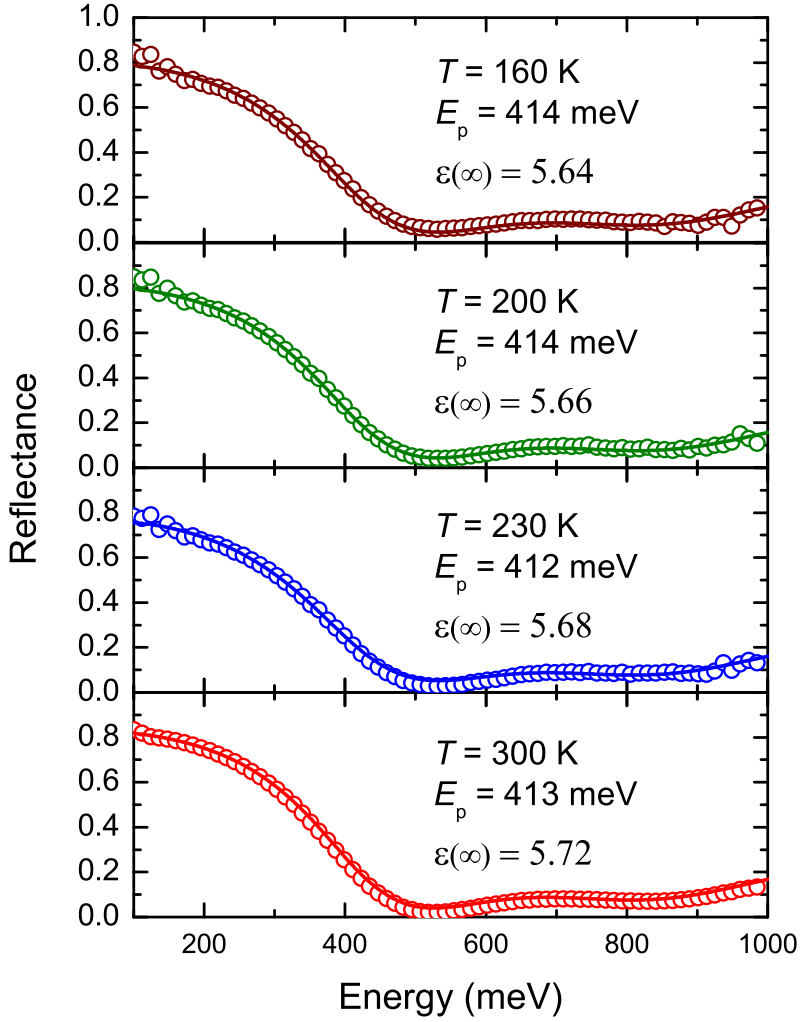

Figure 5.5: Mid-IR reflectance spectra (open circles) and respective simulations (solid lines) of a CdO samples with a thickness of 375±5 nm and a carrier concentration of 2.17×10^{20} cm^{-3} at four different temperatures. The variation of the high frequency dielectric constant is apparent from the simulation while the plasmon energy shows no significant change with temperature. The thickness of the films were determined from the interference pattern above the plasmon energy.

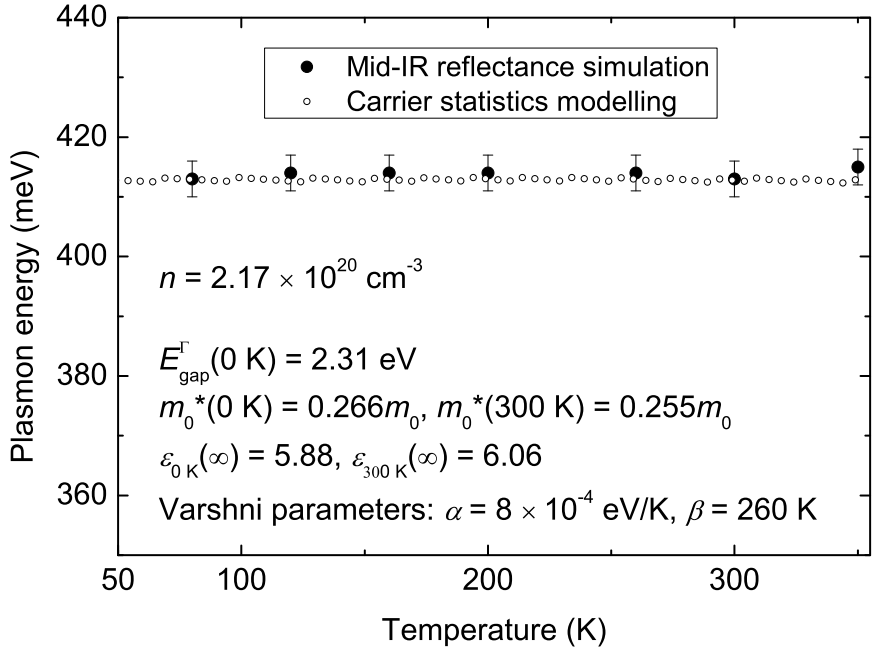

Figure 5.6: Plasmon energy as a function of temperature for a film with n=2.17×10^{20} cm^{-3}. The filled, and open circles are mid-IR reflectance simulation results, and model carrier statistics calculations, respectively. The band edge effective mass (high frequency dielectric constant) decreases (increases) with temperature keeping the plasmon energy unchanged over temperature variations. The values given for $E_{\rm gap}^{\Gamma}$, m_0^*, and $\epsilon(\infty)$ are in the limit of zero carrier density.

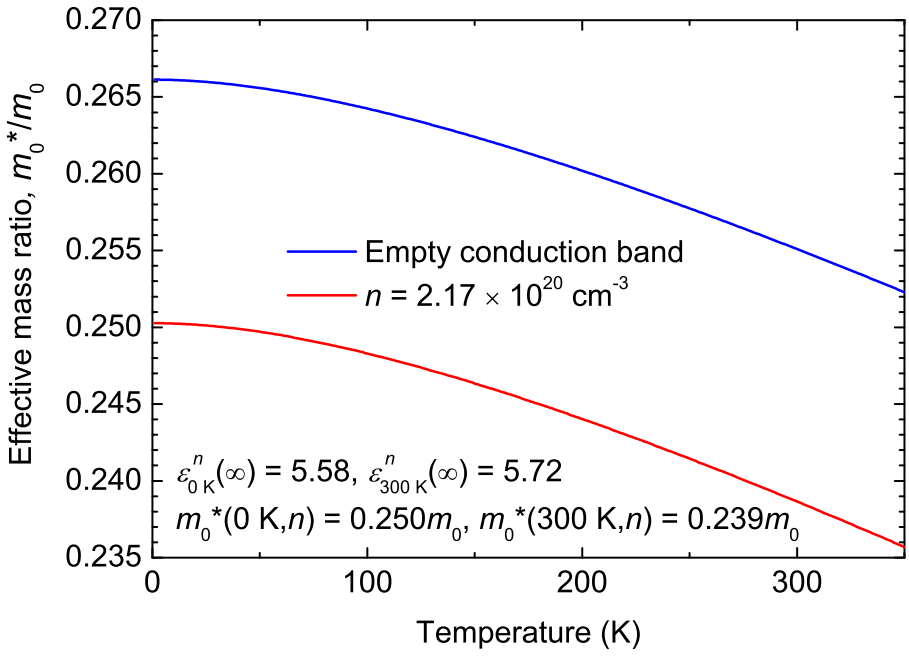

Figure 5.7: Band edge effective mass variations with temperature for an empty, and degenerate conduction band with n=2.17×10^{20} cm^{-3}; The band edge effective mass for the latter at 300 K drops to 0.239m$_0$ along with the effects of band gap renormalization.

flectance as a function of photon energy at different temperatures, and plasma resonant energy as a function of temperature. Reflectance spectra were measured in the range 50-1200 meV as a function of temperature. These data were simulated using a three-layer stratified system (vacuum/CdO/sapphire) with coherent interference. The factorized and classical Drude model of the complex dielectric function were utilized for the infrared-active lattice and carrier response, respectively. Figure 5.5 shows the spectra and model curves for a CdO sample with a carrier concentration of 2.17×10^{20} cm^{-3} at four different temperatures; the thickness of the film is 375±5 nm. These simulations were performed iteratively with model calculations of the temperature behavior of the plasma resonant energy, encompassing the same considerations as in the optical band gap modelling. Additionally, the high frequency dielectric constant and band edge effective mass variations with temperature and carrier concentration have been accounted for in the model; both type of variations have been calculated through the respective variations of the energy gap [72, 146]:

$$n' = \left(\frac{80}{E_{\mathrm{g}}^{\mathrm{opt}}}\right)^{1/4}, \tag{5.2}$$

$$\frac{m_0^*}{m_0} = \left(1 + \frac{E_P}{E_{\mathrm{g}}}\right)^{-1}, \tag{5.3}$$

where, n' is the refractive index (taking, $\epsilon(\infty)=n'^2$), $E_{\mathrm{g}}^{\mathrm{opt}}$ is the optical gap, E_{g} is the fundamental band gap, and E_P is the energy parameter of the momentum matrix element.

Figure 5.6 shows the plasmon energy plots as a function of temperature from mid-IR reflectance simulations and carrier statistics modelling for a film with a carrier concentration n=2.17×10^{20} cm^{-3}. The fundamental band gap, band edge effective mass, and high frequency dielectric constant values are shown for an empty conduction band. As can be seen in the figure, the band edge effective mass decreases with temperature while the high frequency dielectric constant increases. This compensation leads to an unchanged plasmon energy with respect to temperature for CdO.

The high frequency dielectric constant increases with temperature for an

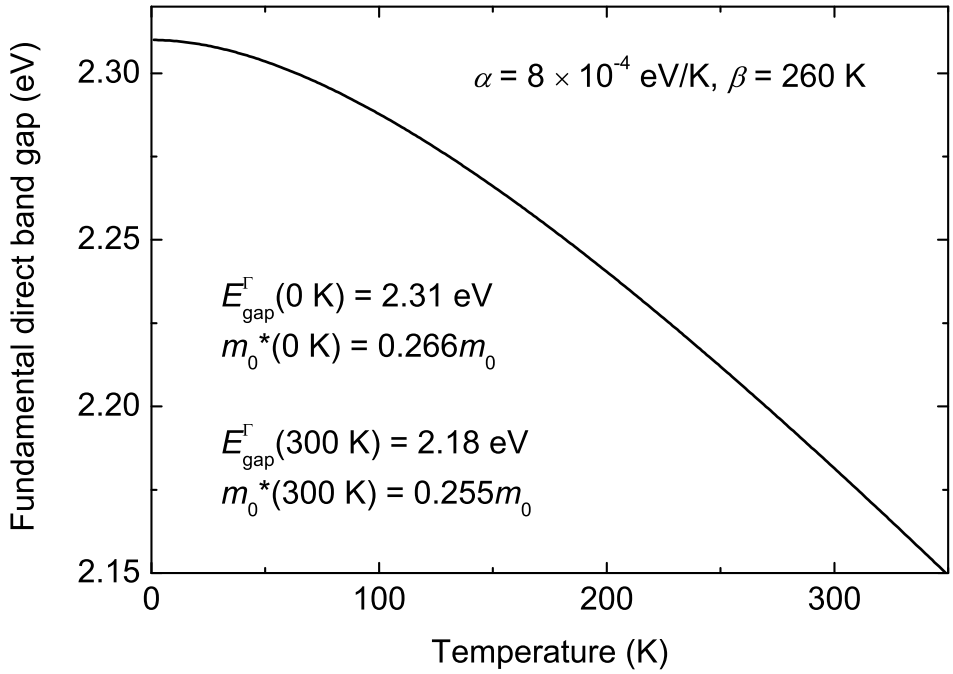

Figure 5.8: The calculated fundamental direct Γ-point band gap variation with temperature in CdO. The fundamental band gap and band edge effective mass at absolute zero are 2.31 eV and $0.266m_0$, respectively. The fundamental band gap (band edge effective mass) reduces to 2.18 eV ($0.255m_0$) at 300 K.

empty conduction band. It varies from 5.88 to 6.06 for temperatures between 0 and 300 K. This increase is due to the fact that the optical gap decreases with temperature as shown in Fig. 5.2. The change in the high frequency dielectric constant for occupied conduction bands is dependent on whether or not band filling will cause an overall optical gap broadening or narrowing considering the temperature variations of the fundamental band gap and the effects of band gap renormalization. This can be seen by comparing $\epsilon_{0\,\mathrm{K}}(\infty)$ and $\epsilon^{n}_{300\,\mathrm{K}}(\infty)$ in Figs. 5.6 and 5.7 where the optical gap has increased despite the band gap narrowing effects.

The simulation of data from several samples allowed the fundamental direct band gap and band edge effective mass variations with temperature to be determined. Fig. 5.8 shows the model curve deduced using the previously determined Varshni parameters for temperature variations of the band gap. The figure shows that the fundamental direct band gap of CdO at 0 K is 2.31±0.02 eV and shrinks to 2.18±0.02 eV at 300 K; the value at 100 K is in agreement with Koffyberg's result [93]. The corresponding 0 K band edge effective mass is $0.266m_0$ at 0 K

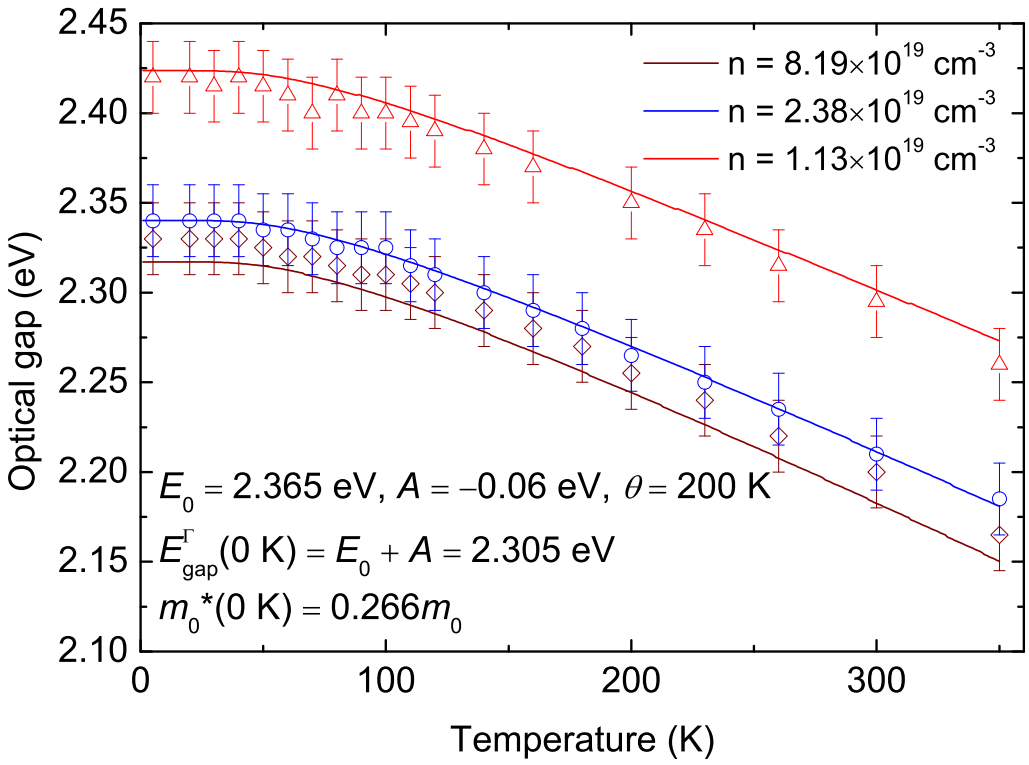

Figure 5.9: Modelling of the optical gap data regarding the Bose-Einstein type oscillators. The temperature-independence of the experimental optical gap values at low temperatures are well simulated by considering the Bose-Einstein phonon statistics. The fundamental band gap at 0 K obtained in this model, $E_g(0\,\mathrm{K}) = 2.305\,\mathrm{eV}$, is almost identical to that of the Varshni model, $E_g(0\,\mathrm{K}) = 2.31\,\mathrm{eV}$.

reducing to $0.255m_0$ at 300 K. Moreover, by applying these values to modelling a film at 300 K with a Fermi level of 0.45 eV above the CBM (corresponding to n=2.17×10^{20} cm^{-3}), it is found that the band edge effective mass further reduces to $0.239m_0$ due to a decrease in the fundamental band gap as a result of band gap renormalization (see Fig. 5.7). This is consistent with a previous study, where a constant band edge effective mass at RT was assumed and was determined to be $0.24m_0$ [94].

In spite of the Varshni description being the most commonly used model in temperature variations of the band gap, this approach predicts a quadratic temperature dependence of band gap at low temperatures which is generally not observed. Therefore, another analysis of the results based on the Bose-Einstein oscillator model will now be presented.

The absorption edge data shown in Fig. 5.2 are additionally modelled using

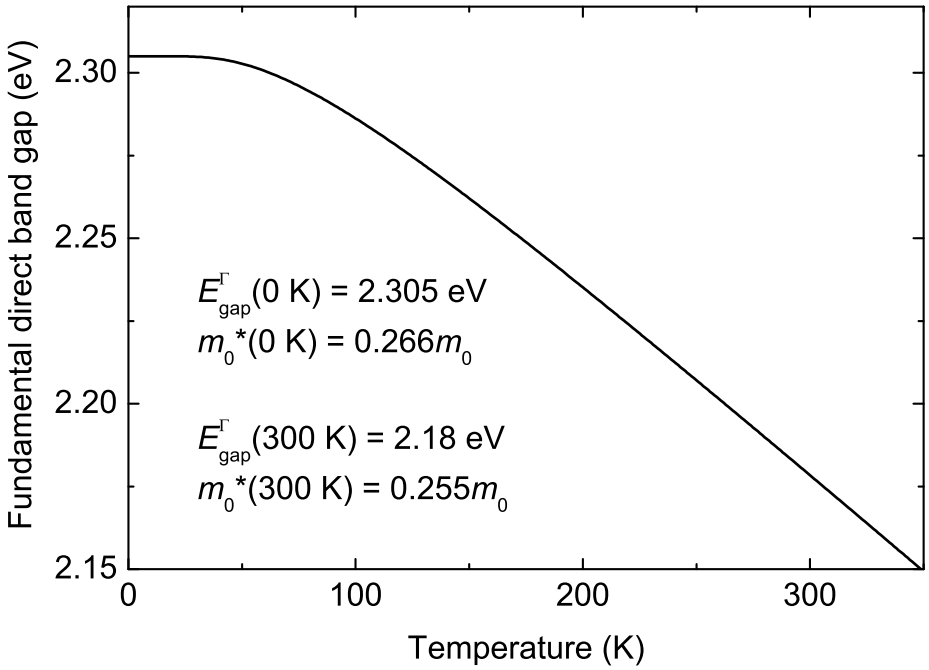

Figure 5.10: The calculated fundamental direct Γ-point band gap variation with temperature in CdO using Bose-Einstein type oscillators. The temperature independence of the fundamental band gap at low temperatures is apparent in this model. The set of band edge effective mass and the fundamental band gap values obtained from the two different models are almost identical (compare Figs. 5.8 and 5.10).

the equations [147, 148]:

$$E(T) = E_0 + A[2n_{\mathrm{BE}} + 1], \tag{5.4}$$

$$n_{\mathrm{BE}} = \frac{1}{\exp(\theta/T) - 1}, \tag{5.5}$$

where, E_0 is an energy parameter, A is a weight factor, n_{BE} is the Bose-Einstein statistics, and θ is the average temperature of the oscillators (phonons). A describes the strength of electron or exciton-phonon interactions and consequently the degree and type of band gap variations with temperature according to its sign. The Bose-Einstein distribution of phonons in this model resolves the low temperature issue existing in Varshni's model. This can be seen in Fig. 5.9 where both the data points and model curves remain unchanged at the low temperature range. The corresponding fundamental direct band gap variations with temperature is presented in Fig. 5.10 in which the same feature is clearly observed at low temperatures. The

parameters in this model are determined to be $E_0 = 2.365$ eV, $A = -0.06$ eV, and $\theta = 200$ K. Hence, the fundamental direct band gap at 0 K is $E_g^{\Gamma}(0\,\mathrm{K}) = E_0 + A = 2.305$ eV. This value is very close to that of the Varshni model; the discrepancy in other quantities such as the band edge effective mass is also negligible.

5.4 Summary and conclusions

Temperature-dependent optical absorption, Hall effect, and infrared reflectance measurements have been performed on as-grown and post-growth annealed CdO films grown by MOVPE on sapphire substrates. The fundamental direct Γ-point gap and band edge effective mass of CdO have been determined at 0 K. This has been implemented by modelling of the temperature variations of the absorption edge alongside an iterative modelling of the temperature variations of the CB plasmon energy and variable-temperature MIR reflectance as a function of the radiation energy. The temperature and carrier concentration variations of the band gap, band edge effective mass, high frequency dielectric constant and the Fermi level have been taken into account. The effects of the non-parabolicity of the CB, Burstein-Moss shift, and band gap renormalization have been considered in the band structure calculations.

Hall effect measurement results affirmed the degeneracy of the films. The Varshni approach as the most commonly used model describing the temperature variations of the band gap has been employed for the CdO films. The Varshni parameters were determined to be α=8×10^{-4} eV/K and β=260 K. However, as this model predicts a quadratic dependence at low temperatures which is not well in accordance with the real trend of data points in that range, an alternative model has also been presented which considers the phonon distribution within the Bose-Einstein statistics. This model shows that the band gap levels off to a constant value at low temperatures, consistent with the trend seen in the data points. The results of both models have been compared setting out almost the same numerical results. The fundamental direct band gap varies appreciably with temperature from 2.31 eV at 0 K to 2.18 eV at 300 K. The corresponding change in the band edge effective

mass is from $0.266m_0$ to $0.255m_0$. The high frequency dielectric constant varies with temperature, as a result of the optical gap variation, from 5.88 at 0 K to 6.06 at 300 K in the limit of zero carrier density. Additionally, the band edge effective mass of a CdO sample with $n = 2.17 \times 10^{20}$ cm^{-3} was calculated to be $0.239m_0$ at 300 K which is consistent with the corresponding value of $0.24m_0$ obtained in chapter 4.

In spite of the unvaried carrier concentration as a function of temperature, electron mobility changes were observed for lower carrier concentrations. The change is attributed to dislocation scattering for temperatures below $\sim$150 K where an increase in mobility is observed, and to phonon scattering for temperatures above that where lattice scattering dominantly reduces the electron mobility.

Chapter 6

Carrier transport properties in unintentionally-doped MBE-grown SnO_2

6.1 Introduction

Tin dioxide (SnO_2) is a group IV-VI oxide semiconductor which crystalizes in a rutile structure with a tetragonal unit cell in the space group $P4_2/mnm$. The SnO_2 crystal structure together with its first Brillouin zone is shown in Fig. 6.1. The lattice parameters are $a = b = 0.4738$ nm and $c = 0.3187$ nm [149], and the minimum direct allowed band to band transitions for nominally undoped SnO_2 films from some experimental studies [150–155] range between 3.3 and 4.3 eV. Different values were obtained within this range for the two crystallographic directions, i.e., $\boldsymbol{r} \perp \boldsymbol{c}$ and $\boldsymbol{r} \parallel \boldsymbol{c}$ due to the optical and electronic anisotropy of the SnO_2 structure. Many theoretical investigations have reported the minimum dipole-forbidden energy gap to range between 3 and 3.7 eV [29, 156, 157]. The energy of the $1\boldsymbol{S}$ exciton in SnO_2 from a two-photon absorption spectrum was deduced to be 3.563 eV at 4.5 K [158], as shown in Fig. 6.2(a). This value is consistent with the previously determined one-photon absorption values [159, 160] which gave a band gap of 3.597 eV at 1.8 K for SnO_2. A later two-photon absorption study [161] with the exciton energy of 3.56174 eV [shown in Fig. 6.2(b)] determined the band gap to be 3.596 eV at 7 K. This indicates that a fundamental direct band gap of 3.5 eV could be an appropriate value for undoped SnO_2 at room temperature. Having a high spectral range of transparency, a high conductivity has also been achieved as a result of both native defects and doping.

The electronic properties of oxide surfaces and heterointerfaces have become an extremely interesting area in materials science research, ranging from insulating [25] and semiconducting heterostructures [162] to interface engineering of

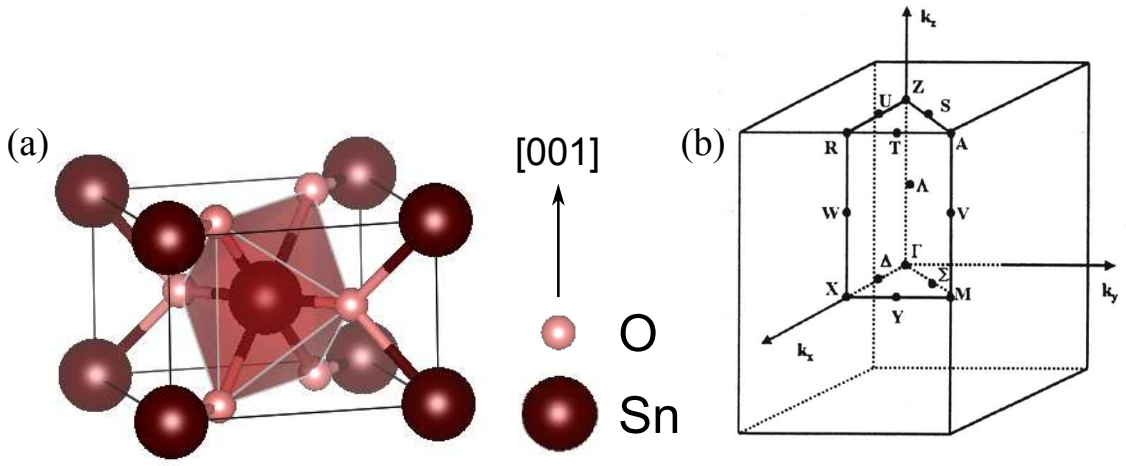

Figure 6.1: (a) Tetragonal unit cell of the rutile structure of SnO_2; (b) the corresponding first Brillouin zone. The coordination geometries of Sn and O atoms are octahedral and trigonal planar, respectively. The structural anisotropy of SnO_2 is clearly apparent.

systems for solid-state electronics [163, 164]. Interface-induced defects in lattice-mismatched heterostructures can significantly alter the electronic properties of the films. In heteroepitaxial systems with large lattice mismatch, the crystalline quality, transport, and electronic properties of the thin films are strongly dependent on film thickness due to the creation of strain relieving misfit and threading dislocations (TDs) originating at the interface. This directly impacts the mobility of the free carriers and the associated device performance. Moreover, as charged dislocations act as a source of free carriers, they make an additional contribution to the conductivity, therefore, the trade-off between carrier density enhancement and limited mobility by dislocations relies on understanding these mutual effects, charging and defect scattering, in heteroepitaxial semiconductor layers.

Several studies have investigated strain relaxation [165, 166], defect reduction [167–169], and the electrical properties of TDs in highly lattice-mismatched heteroepitaxial III-V materials, including III-nitrides. Indeed, cross-sectional TEM and XRD studies of epitaxial GaN [170, 171] have shown that dislocations originate at the interface and their density decreases with increasing layer thickness. Somewhat surprisingly, studies of the influence of dislocations on carrier transport properties almost invariably assume a uniform density of dislocations throughout the film. For example, theoretical and experimental work by Look *et al.* [53] and Weimann

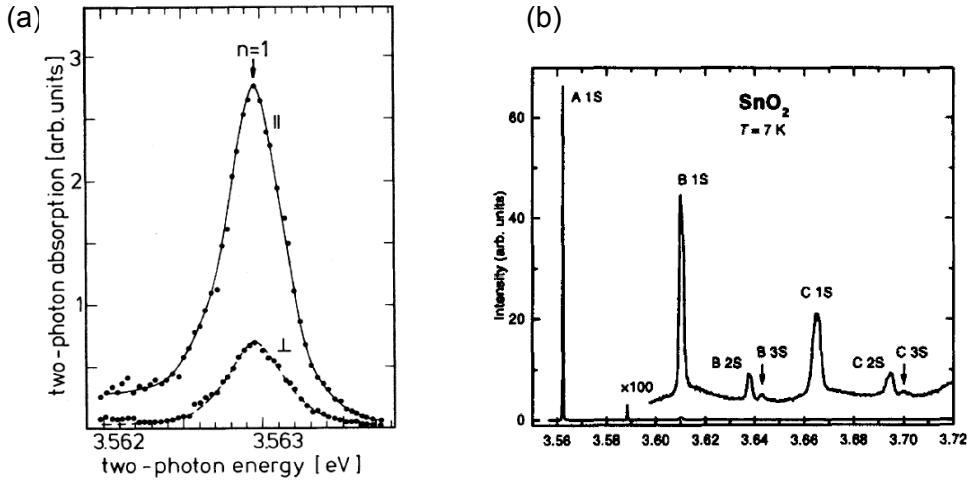

Figure 6.2: (a) Two-photon absorption spectra of the 1$\boldsymbol{S}$ exciton in SnO_2 at 4.5 K by Fröhlich, *et al.* [158]. $\parallel$ and $\perp$ denote different polarized light configurations. (b) The corresponding two-photon absorption spectra in SnO_2 at 7 K by Reimann and Steube. 'A 1$\boldsymbol{S}$' denotes the respective exciton of the uppermost valence band (from Ref. [161]).

et al. [52] investigating the mobility of carriers in GaN considered a uniform density of dislocations and concluded that the dislocations in GaN are negatively charged. In studies of highly lattice-mismatched MBE-grown InN on sapphire with a GaN buffer layer, dislocations were found to be positively charged, contributing to both the n-type conductivity [54, 172] and carrier scattering [173]. Modeling of the electrothermal transport data from InN by Miller *et al.* [174] supported the charged nature of the dislocations, as concluded by the previous studies [52, 53], however, they still took constant values for the dislocation density.

A recent multilayer analysis of MBE-grown InN using both Hall and Seebeck profiling [175] showed a strong depth-dependence of both the carrier concentration and mobility. In previous studies, a constant or average dislocation density and carrier concentration has been used for each sample. If charged-dislocation scattering is important, then carrier and dislocation density variations throughout the sample must be taken into account as the scattering strength and its variation across the layers for ionized defects are not the same as those for the dislocation deformation potential. Therefore, without a layer-by-layer mobility analysis, no accurate numerical modeling and recognition of the relative effectiveness of these scattering mechanisms would be possible.

In spite of their use as transparent conductors and potential for transparent electronics [176], relatively little is known about the intrinsic properties of the binary oxide semiconductors (ZnO, CdO, In_2O_3, Ga_2O_3, etc), and the interplay of transparency and conductivity. In particular, SnO_2 is an n-type transparent conducting oxide with a wide, direct fundamental band gap. It has a significant number of applications in solid-state gas sensing, transparent conducting contacts and electronics, display systems, and as an oxidation catalyst [177–180]. High-quality SnO_2 has only recently been available as heteroepitaxial films and is therefore subject to interface-induced extended defects.

In this chapter, the mobility of electrons in unintentionally doped, highly lattice-mismatched SnO_2/Al_2O_3 films has been modelled as a function of carrier concentration within the framework of a layer-by-layer analysis. The most probable scattering mechanisms, i.e., longitudinal polar-optical mode, acoustic deformation potential, ionised defect, acoustic piezoelectric, neutral impurity, and dislocation deformation potential scattering, are all taken into account and the dominant scattering mechanisms identified. The Mott transition, describes the transition from insulating to metallic behaviour of a material [181, 182]. In semiconductors this transition level can be reached by doping. For SnO_2, the Mott transition level corresponds to a carrier concentration $n = 10^{18}$ cm^{-3}. Here, this level has been taken to identify the degeneracy of the SnO_2 films. It is demonstrated that the TDs in MBE-grown SnO_2 on r-sapphire are positively charged. This charging and the effect of defect scattering, necessitates consideration of the dislocation density and the corresponding carrier concentration variation as a function of depth in the thin films for accurate carrier transport studies of highly lattice-mismatched semiconductor materials.

6.2 Experimental details

In this study, the samples used were high-quality, unintentionally doped SnO_2 (101) films, with a range of thicknesses, grown by plasma-assisted molecular-beam epitaxy (PAMBE) on r-plane ($10\bar{1}2$) sapphire [149] at the University of California

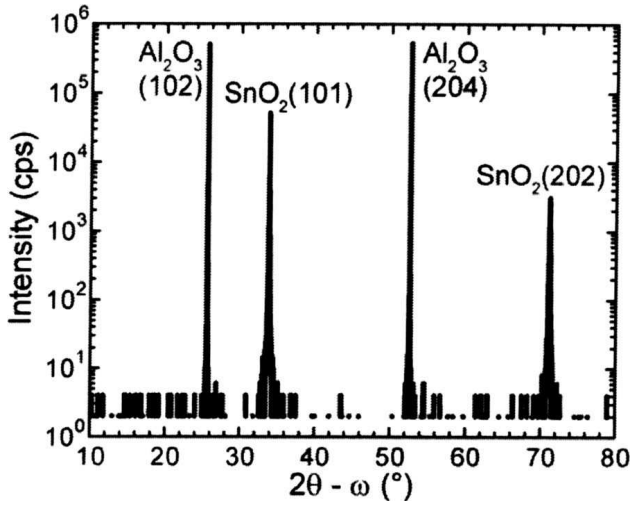

Figure 6.3: HRXRD 2θ-ω scan of SnO_2 on r-sapphire indicating a phase-pure $SnO_2(101)$ film. Within the sensitivity of the measurement, no other orientations of SnO_2 nor any SnO or Sn were observed in the films [149].

Santa Barbara, California, USA. A standard Knudsen effusion cell was used to evaporate liquid Sn and a Veeco UNI-Bulb radio-frequency plasma source to supply monatomic oxygen. The lattice mismatch of $SnO_2(101)/r$-sapphire samples is 0.4% and -11.3% along the <010> and <101> directions, respectively. A high resolution x-ray diffraction (HRXRD) 2θ-ω scan on a typical sample is shown in Fig. 6.3. The four peaks observed in the figure correspond to SnO_2 101 and 202, and sapphire $10\bar{1}2$ and $20\bar{2}4$ reflections which clearly indicate a phase-pure $SnO_2(101)$ as the epitaxial growth surface on r-sapphire; no other orientation from the SnO_2 crystal was observed in this and subsequent XRD measurement.

Optical reflectance measurements in the mid-infrared (MIR) region were performed using a Bruker Vertex 70v Fourier-transform infrared (FTIR) spectrometer to determine the thickness of the samples. Because SnO_2 is optically anisotropic, a zinc-selenide MIR polarizer was employed to attain s-polarized light. X-ray diffraction (XRD) measurements were performed using Agilent Technologies CCD diffractometer (GEMINI R model) which collects the X-ray diffraction intensities and has a built-in procedure to recognize the reciprocal lattice and define the corresponding basis vectors, a^*, b^*, c^*. It uses the Co K-α radiation with $\lambda = 1.54056$ Å. This radiation corresponds to the stronger absorption of the X-ray beam in the material for its relatively high wavelength. Hence, if an X-ray beam passes through a sample

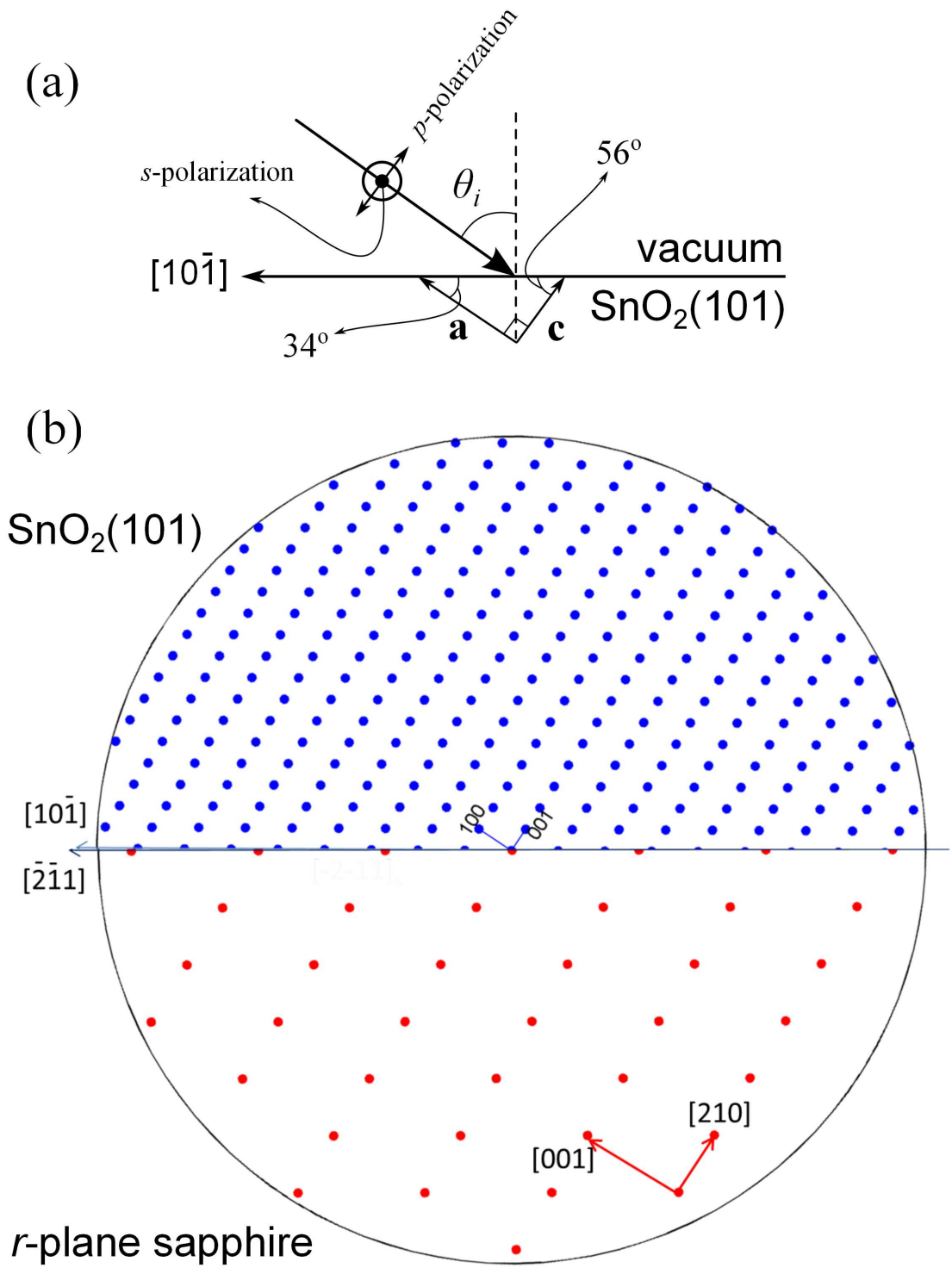

Figure 6.4: Schematic representation of polarized light incident on $SnO_2(101)$ and a specific view of certain crystallographic directions. (a) shows the configuration in which the condition $\boldsymbol{E}^s \perp \boldsymbol{c}$ is attained for $SnO_2(101)$, and (b) shows that the direction $[10\bar{1}]$ in SnO_2 is aligned with $[\bar{2}\bar{1}1]$ in sapphire and that the $\boldsymbol{c}$ axes, [001], of both layers lie in the same plane and being perpendicular to the s-polarized light under the condition shown in (a).

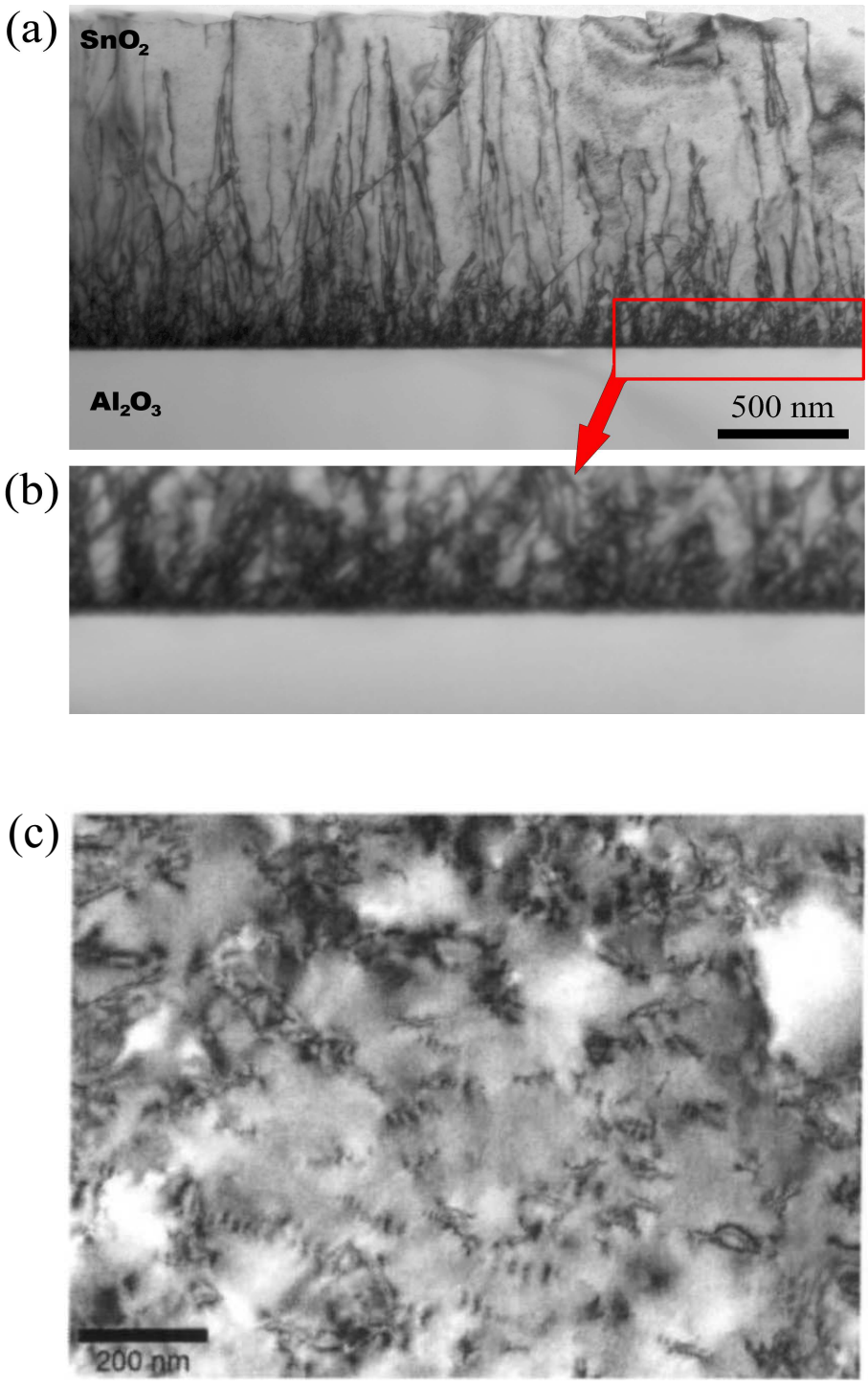

Figure 6.5: (a) Cross-sectional TEM image of MBE-grown SnO_2/r-sapphire showing the TDs formed at the interface and propagating through the layer. The expansion of the region outlined in red is shown in (b) demonstrating the extremely high dislocation density in the region less than 110 nm from the interface. (c) Typical plan-view TEM image [149] showing that the depth dependence of dislocation density determined by cross-sectional TEM is the same as the thickness dependence obtained from plan-view TEM images of the samples.

with thickness $t = 500$ nm and an attenuation coefficient μ (μ=1380 cm^{-1} for SnO_2), the intensity of the beam is $I = I_0 \exp(-\mu t) = 0.93$. This means that 7% of the beam will be absorbed in the SnO_2 layer. To maximize the absorption so that less beam reaches the substrate to get a weaker diffraction signal from sapphire, the measurements were performed at small incident angles. On average, 70 very strong and 40 very weak reflections were collected from the sapphire substrate and the SnO_2 films, respectively. This amount of reflection was enough to separate and reconstruct the lattices. X-ray diffraction was implemented to ascertain the $[10\bar{1}]$ direction in the SnO_2 films to align the s-polarized electric field, $\boldsymbol{E}$, perpendicular to the c axis. The crystallographic direction $[10\bar{1}]$ in SnO_2 is aligned with $[\bar{2}\bar{1}1]$ in sapphire. This ensures that by suitable rotation around the surface normal, s-polarized light is perpendicular to the c axis of SnO_2 and sapphire during the passage of light through the sample. This is illustrated in Fig. 6.4. Dislocation imaging was carried out in a JEOL 2000FX TEM. The dislocation density was determined from images acquired in 101 bright field conditions with the incident electron beam at $\sim 30^\circ$ relative to the interface plane. Cross-sectional images were used to determine both the number of dislocations and the depth at which they occur. These values were substantiated by plan-view TEM images in excellent agreement with the cross-sectional values for dislocation densities. Planar defects were also observed with much lower abundance and limited to areas close to the interface. Hall effect measurements based on the standard Van der Pauw geometry were carried out to determine the total sheet density and transport mobility of each sample. All measurements were performed at room temperature.

6.3 Dislocation density and carrier concentration variations

A cross-sectional TEM image of the thickest SnO_2/r-sapphire sample is shown in Figs. 6.5(a) and 6.5(b). High densities of TDs are observed originating from the interface propagating towards the surface of the film. This interfacial region is expanded in panel (b) showing TDs up to 110 nm from the interface. Dislocation densities as a function of depth (distance from the interface) were obtained from

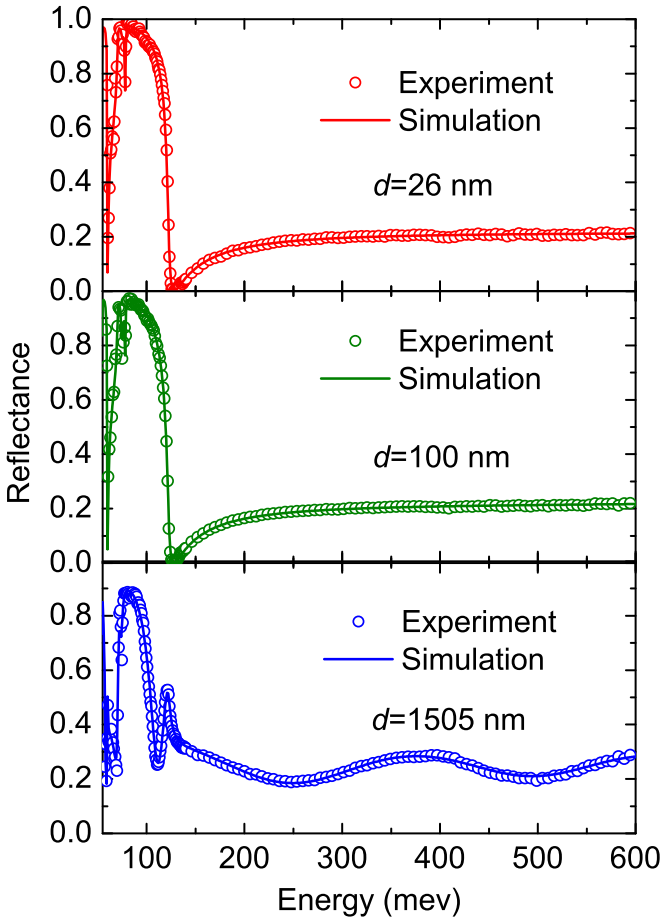

Figure 6.6: *s*-polarized reflectance data and simulation as a function of energy for three different SnO_2 films with different thicknesses. The thickness of the samples were determined to range between 26 and 1505 nm. The thicknesses were determined by fitting the interference pattern above ∼125 meV. In cases where no such pattern is observed, which happens for thinner films, the thickness is determined by the amount of reflection in the same regions. Films with different thicknesses show different plasma frequencies that is indicative of a varying carrier concentration throughout the layers of the films.

both cross-sectional and plan-view TEM images at specific thicknesses. These data with an exponential fit (solid line) are shown in Fig. 6.7(a). The data points clearly indicate the depth dependence of the dislocation density, although it becomes increasingly difficult to accurately assess close to the interface, as reflected in the error bars.

Mid-IR *s*-polarized reflectance measurements, satisfying the condition $\boldsymbol{E}\perp\boldsymbol{c}$, were performed at an incident angle of 56° with respect to the surface normal within the range of 50 to 600 meV, to determine the thickness of each sample. This is shown

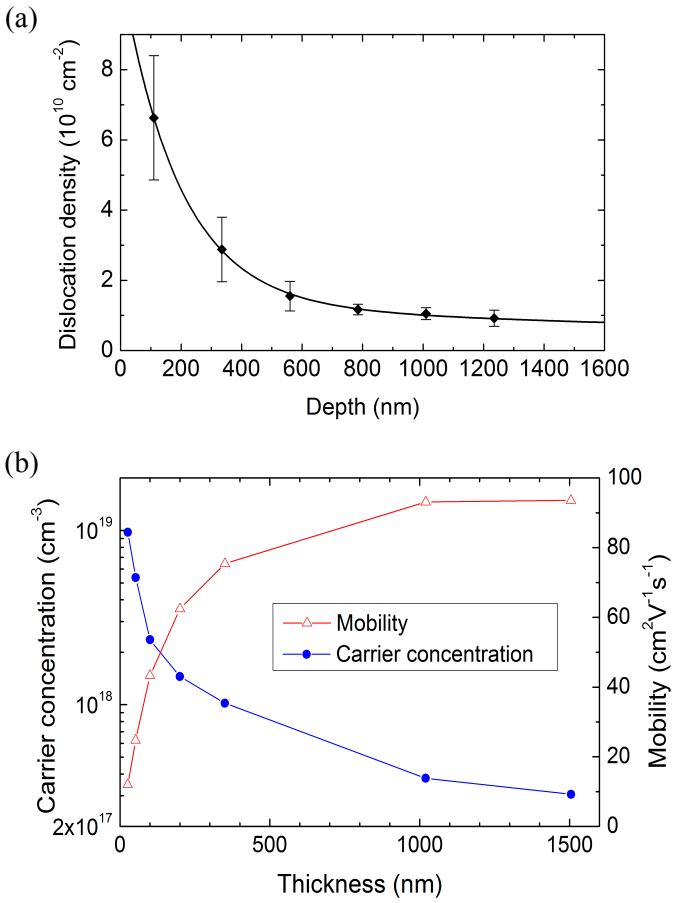

Figure 6.7: (a) Dislocation density profile as a function of depth (distance from the interface). The data points are obtained from TEM measurements. As the concentration of dislocations is highest close to the interface (see Fig. 6.5), there is a higher degree of error in the measured dislocation densities. The solid curve is the exponential fit to the data points. (b) Carrier concentration and mobility as a function of film thickness. The same trend in (a) is observed for the Hall carrier concentration as a function of thickness contrary to the Hall mobility, which increases with film thickness.

in Fig. 6.6 together with the calculated model curves (solid lines). The reflectance data were simulated using a 3-layer stratified medium, i.e., vacuum/SnO_2/sapphire with coherent interference. A complex dielectric function was used where the transverse and longitudinal polar-optical lattice modes were accounted for within the factorized model with Lorentzian broadening, and the carrier response by the classical Drude model:

$$\tilde{\epsilon}_{\perp}(\omega) = \epsilon_{\perp}(\infty) \prod_{i}^{l} \frac{\omega_{\mathrm{LO},\perp i}^2 - \omega^2 - i\omega\gamma_{\mathrm{LO},\perp i}}{\omega_{\mathrm{TO},\perp i}^2 - \omega^2 - i\omega\gamma_{\mathrm{TO},\perp i}} - \frac{\epsilon_{\perp}(\infty)\omega_{\mathrm{p},\perp}^2}{\omega(\omega + i\gamma_{\mathrm{p},\perp})}. \tag{6.1}$$

The sample thicknesses ranged from 26 to 1505 nm, determined by the oscillations

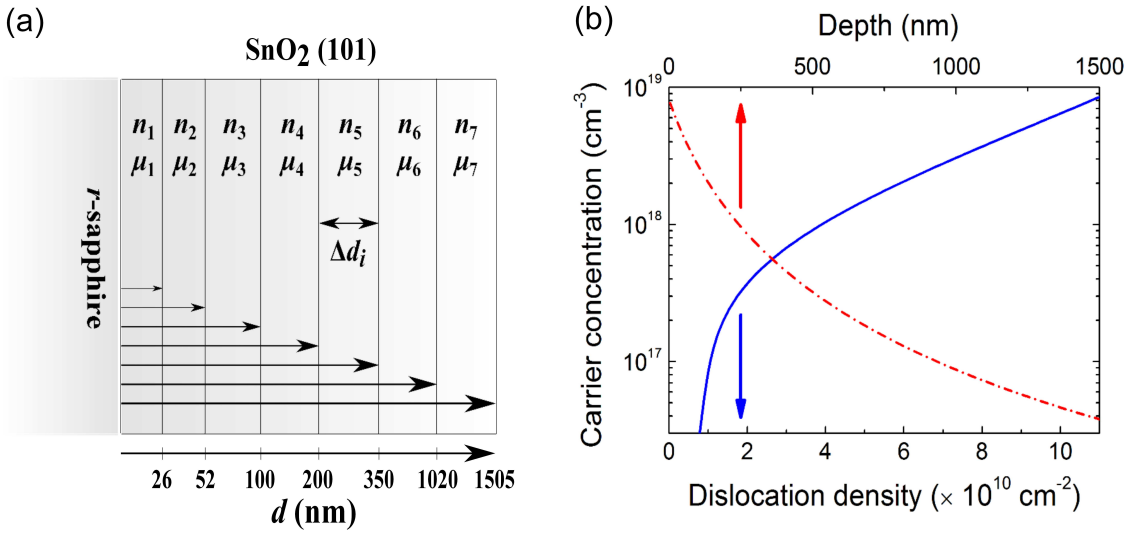

Figure 6.8: (a) Schematic representation of a 7 layer SnO_2 film on r-sapphire. The area delimited by the interface and every line designates each available sample. Δd_i is the thickness of each layer. (b) A layer-by-layer profile of carrier concentration as a function of dislocation density (solid line) and depth (dot-dashed line); data obtained using parallel conduction analysis together with dislocation density variations with depth. Carrier concentration decreases with distance from the interface, and increases with dislocation density.

occuring above the phonon/plasmon band. For thinner films where no oscillation is observed, the thickness influences the amount of reflection in the same region. The values obtained were consistent with those from scanning electron microscopy and TEM. The Hall carrier concentration for each sample was calculated via $n_{\mathrm{av}}^{\mathrm{3D}} = n_{\mathrm{H}}/t$, where n_{H} is the sheet density and t is the thickness of the film.

The Hall carrier concentration shows a significant decrease, and the mobility a comparable increase, with increasing sample thickness, as can be seen in Fig. 6.7(b); a similar trend can be seen for the SnO_2 films in Ref. [183]. The rapid decrease of carrier concentration with SnO_2 film thickness and dislocation density with depth implies that there exists a correlation between carrier concentration and dislocation density indicating the donor-like nature of the TDs. To further corroborate this, modelling of the electron mobility as a function of carrier concentration has been performed. However, the raw Hall data provide an "average" value of both quantities over the whole thickness of each sample. In order to correct for this effect, a parallel conduction analysis was performed to minimize the Hall-averaging error within the

layers [184].

6.4 Depth profiling and layer-by-layer mobility modelling

Figure 6.8 shows schematically the thickest sample assumed to consist of seven layers, wherein the distance between each line and the interface corresponds to each available sample with a certain thickness. The sheet density and mobility of each layer are derived according to the equations below [184, 185]:

$$n_i = \frac{\left(n_{\mathrm{H},i}\mu_{\mathrm{H},i} - \sum_{j=1}^{i-1} n_j\mu_j\right)^2}{n_{\mathrm{H},i}\mu_{\mathrm{H},i}^2 - \sum_{j=1}^{i-1} n_j\mu_j^2}, \tag{6.2}$$

$$\mu_i = \frac{n_{\mathrm{H},i}\mu_{\mathrm{H},i}^2 - \sum_{j=1}^{i-1} n_j\mu_j^2}{n_{\mathrm{H},i}\mu_{\mathrm{H},i} - \sum_{j=1}^{i-1} n_j\mu_j}, \tag{6.3}$$

where $n_{\mathrm{H},i}$ and $\mu_{\mathrm{H},i}$ are the Hall sheet density and mobility of each sample embracing i layers, and n_i and μ_i are the sheet density and mobility of the i^{th} layer, respectively. The carrier concentration of each layer is obtained via $n_{3\mathrm{D},i} = n_i/\Delta d_i$ where Δd_i is the thickness of each layer. As Δd_i still covers a distance within the sample, each calculated $n_{3\mathrm{D},i}$ is considered the value at the $\Delta d_i/2$ level of each layer. It is worthy of note that having more samples, particularly with closer thicknesses (smaller Δds), would have helped in the minimization of errors in the depth profiling. The mobility and carrier concentration of each layer are represented as $\mu\left(n_{3\mathrm{D}}\right)$ and shown in Fig. 6.10 (solid points).

Carrier concentration as a function of depth, $n_{3\mathrm{D}}\left(d\right)$, is determined by fitting a curve to the calculated data points; see Fig. 6.8(b). Using $n_{3\mathrm{D}}\left(d\right)$ in the exponential fit shown by the solid line in Fig. 6.7(a) allows the derivation of carrier concentration variations with dislocation density. This is shown in Fig. 6.8(b) which signifies the fact that the carrier concentration increases (decreases) with dislocation density (distance from the interface). Hence, a direct link between the dislocation density and carrier concentration is made via parallel conduction and depth analysis in the functional, $N_{\mathrm{dis}}\left(d\left(n_{3\mathrm{D}}\right)\right)$, throughout the SnO_2 layers and is used in the mobility modelling.

A layer-by-layer model of mobility versus carrier concentration, $\mu\left(n_{3\mathrm{D}}\right)$, has

been determined by accounting for the key scattering mechanisms, namely, acoustic deformation potential (ADP) [186], acoustic piezoelectric (AP) [187], longitudinal polar-optical mode (LPO) [186, 188], neutral impurity (NI) [189], ionized defect (ID) [119, 186], and dislocation deformation potential (DDP) scattering [190]. Table 6.1 shows the respective scattering-limited mobility relations used for the simulation of the carrier mobility data. Figure 6.10 shows the results of the model curves pertaining to successive inclusion of the dominant mobility-limiting scattering mechanisms using the standard Matthiessen rule:

$$\frac{1}{\mu_{\text{tot}}} = \sum_i \frac{1}{\mu_i}. \tag{6.4}$$

This rule has been employed while being aware of the possible error due to an extra term pertaining to possible interdependencies of the different scattering mechanisms. Nonetheless, as the modelling is performed at a single temperature, any discrepancy is expected to be only a constant offset of the entire mobility curve, leaving all reported trends intact.

As mentioned earlier, the treatment of optical properties is with respect to the condition that $\boldsymbol{E}\perp\boldsymbol{c}$, wherein the longitudinal optical (LO) modes propagate parallel to the surface as well as the carriers. All three LO modes used in mid-IR reflectance simulations have been considered for polar optical scattering. In respect of ionized defect scattering, model carrier statistics have been calculated to evaluate the Fermi level positions using a band gap and band edge effective mass of 3.5 eV [158, 161] and $0.27m_0$ [193] (an average value according to the optical and electronic anisotropy of SnO_2), both at room temperature, respectively. As the Fermi-level positions corresponding to the layer carrier concentrations range between -0.08 and 0.04 eV with respect to the conduction band minimum (CBM), and the charge neutrality level (CNL) of SnO_2 lies 0.5 eV above the CBM [194], the density of ionized defects has been approximated by that of ionized donors. That is, it has been assumed that the acceptor density is negligible. Moreover, referencing to the calculated Fermi-level positions being near the CBM, it has been deduced from the formation energies of native defects and impurities by first-principles density

Table 6.1: Mobility functions for different scattering mechanisms

Scattering mechanism	Scattering-limited mobility function ($cm^2V^{-1}s^{-1}$)
ADP [186]	$\frac{2(2\pi)^{1/2}}{3}\frac{\rho v_s^2\hbar^4}{E_c^2 <m^*>^{5/2} (K_BT)^{3/2}}$ (6.5)
AP [187]	$\frac{16(2\pi)^{1/2}}{3}\frac{\hbar^2\epsilon(0)\epsilon_0}{<m^*>^{3/2} e^2K^2(K_BT)^{1/2}}$ (6.6)
LPO [186, 188]	$\frac{\hbar}{2\alpha_{LO}E_{LO}m_p}\frac{f(\alpha_{LO})}{[1+(\alpha_{LO}/6)]^2}[\exp(E_{LO}/K_BT)-1]$ (6.7)
	$\alpha_{LO} = \frac{1}{4\pi\epsilon_0}\frac{e^2}{\hbar}\left(\frac{<m^*>}{2E_{LO}}\right)^{1/2}\left(\frac{\epsilon(0)-\epsilon(\infty)}{\epsilon(0)\epsilon(\infty)}\right)$
	$m_p = <m^*> (1+\alpha_{LO}/6)$
	$\mu_{LO} = \left(\sum_i 1/\mu_{LO,i}\right)^{-1}$ [191]
NI [189]	$\frac{<m^*> e^2}{20N_{NI}\epsilon(0)\epsilon_0\hbar^3}$ (6.8)
$ID_{non-deg}$ [186]	$2^7(2\pi)^{1/2}\frac{(\epsilon(0)\epsilon_0)^2(K_BT)^{3/2}}{e^4<m^*>^{1/2} Z^2N_i}\left[\mathrm{Ln}(1+y)-\frac{y}{(1+y)}\right]^{-1}$ (6.9)
	$y = \frac{24\epsilon(0)\epsilon_0 <m^*> (K_BT)^2}{n\hbar^2e^2}$
ID_{deg} [119]	$\frac{24\pi^3(\epsilon(0)\epsilon_0)^2\hbar^3n}{e^4<m^*>^2 Z^2N_i}\left[\mathrm{Ln}(1+y)-\frac{y}{(1+y)}\right]^{-1}$ (6.10)
	$y = \frac{2(3n\pi^8)^{1/3}\hbar^2\epsilon(0)\epsilon_0}{e^2<m^*>}$
DDP [190]	$\frac{32K_BT\hbar}{3\pi E_D^2l^2<m^*>N_{dis}}\left(\frac{1-\nu}{1-2\nu}\right)^2$ (6.11)

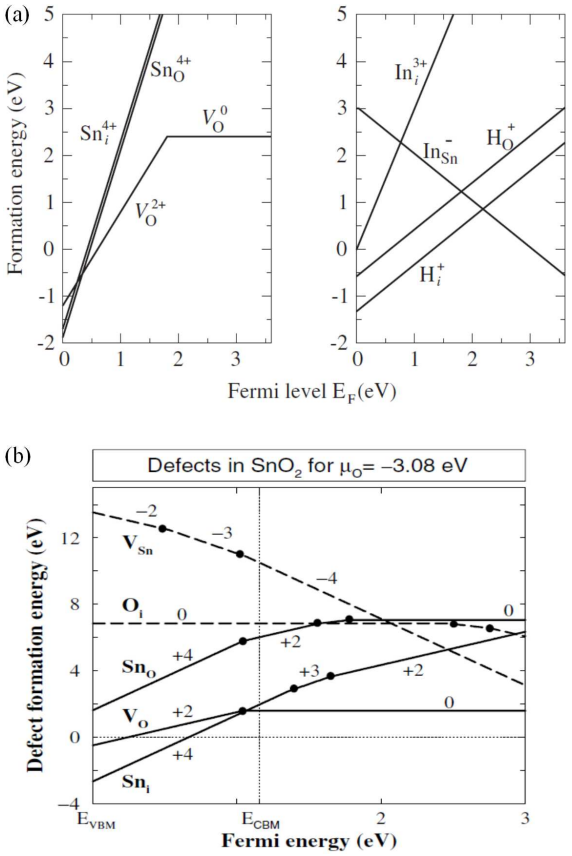

Figure 6.9: DFT calculated formation energies as a function of the Fermi level referenced to the valence band maximum within (a) the generalized gradient approximation (GGA) of the intrinsic donor-type defects and impurities by Singh, *et al.* [46], and (b) the local density approximation (LDA) of native point defects by Çetin Kılıç and Alex Zunger [192]. For the Fermi levels in the vicinity of the CBM ($E_g = 3.6$ eV) in (a), hydrogen impurities as H_i^+ and H_O^+ are the most likely donors to be incorporated in the crystal, and V_O is stable only in the neutral charge state. From (b), Sn_i^{4+} is the most energetically favourable native donor to form for the Fermi energies near the CBM. Its transition to Sn_i^{3+} occurs at $E_{CBM} + 203$ meV which is above the highest Fermi energy in the layers. Here, V_O^{2+} could be a possible donor state in SnO_2 films.

functional theory (DFT) calculations in SnO_2 [46, 192] that hydrogen impurities (H_i^+, H_O^+) together with oxygen vacancy (V_O^{2+}) and tin interstitial (Sn_i^{4+}) native defects are the most probable charged centres to form. The formation energy of different defects and impurities in SnO_2 as a function of the Fermi level is shown in Fig. 6.9. All the three possible charge states have been considered in modelling the respective scattering mechanisms.

As the dependence of carrier concentration on dislocation density is set according to the analyses above, dislocation scattering is treated as a dual mechanism, due to the charged centres and the deformation potential generated by their pres-

ence in the lattice. In order to distinguish the relative importance and effectiveness, different expressions have been used for these two mechanisms, contrary to previous works where a single expression has been used for charged-dislocation scattering [52, 53, 195]. The scattering by positively charged defects along the dislocations has been accounted for using the Brooks-Herring (BH) formula [186] for carrier concentrations below the Mott transition level for SnO_2, $n = 10^{18}$ cm^{-3}, and the degenerate form of the BH formula [119] for carrier concentrations above the Mott level. At this level, the Fermi energy and the CBM nearly coincide in the SnO_2 films. Additionally, the following relation has been utilized for DDP scattering-limited mobility which explicitly takes into account relevant characteristic parameters such as Poisson's ratio and DDP of the lattice [190],

$$\mu_{\mathrm{DDP}} = \frac{32 K_{\mathrm{B}} T \hbar e}{3\pi E_{\mathrm{D}}^2 l^2 <m^*> N_{\mathrm{dis}}} \left(\frac{1-\nu}{1-2\nu}\right)^2, \tag{6.12}$$

where ν is the Poisson ratio which is 0.29 for SnO_2 [196], m^* is the effective mass, l is the unit slip distance, and E_{D} is the characteristic energy pertaining to the scattering potential; a value of E=7 eV has been used for SnO_2 which lies within the range of the determined values for other materials. The other quantities have their usual meanings. As the lattice mismatch of $SnO_2(101)/r$-sapphire is 0.4% and 11.3% along the <010> and <101> directions, respectively, the majority of dislocations are formed with reference to the <101> direction. This has been reflected in the unit slip distance (l).

Previous attempts at modelling charged-dislocation scattering [52, 53, 195] explain the increase of the mobility for increasing carrier concentrations up to 10^{17}–10^{18} cm^{-3} as being the result of screened negatively-charged-dislocation scattering in GaN. This increase in mobility is not seen in the case of SnO_2 as the dislocations are positively charged (as shown here). As a result, the screening of positively-charged defects along the dislocations can be treated similarly to that of positively-charged defects in the bulk region within the Brooks-Herring model. This allows a distinctive approach to be employed of independently weighing the dual scattering effect associated with dislocations in heteroepitaxial SnO_2, the deformation potential

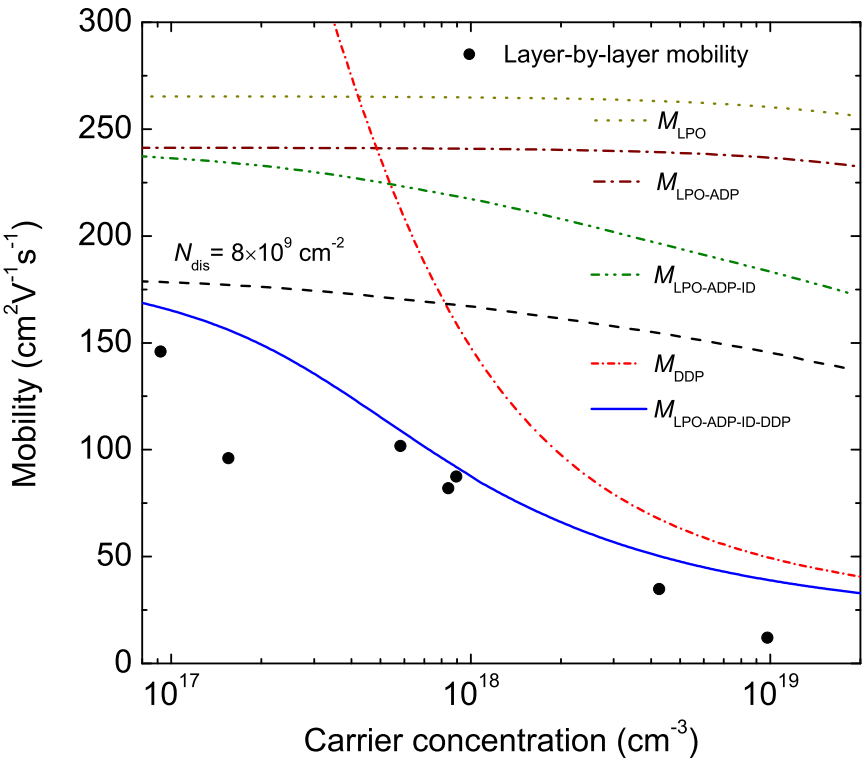

Figure 6.10: Layer-by-layer mobility versus carrier concentration data and simulation. The model curves resulting from successive addition of the dominant scattering mechanisms using Matthiessen's rule are represented. LPO, ADP, ID, and DDP stand for longitudinal polar-optical mode, acoustic deformation potential, ionized defect, and dislocation deformation potential scattering, respectively. The individual effects of LPO and DDP scattering-limited mobility can be seen in the figure. The dashed line shows the resultant mobility model curve regarding a constant value of $N_{\rm dis} = 8 \times 10^9 {\rm cm}^{-2}$ from the interface to the surface while the solid curve accounts for the dislocation density variations throughout the layers. The large difference in the mobility between these two approaches is apparent, specifically, for higher carrier concentrations.

scattering and the ionized defect scattering associated with the positively-charged defects along the dislocations.

From the simulation and analysis of layer-by-layer mobility versus carrier concentration, the highest energy LPO phonon mode is found to interact most strongly with the mobile electrons. As can be seen in Fig. 6.10, the addition of ADP scattering discernably reduces the mobility. The resultant model curve for LPO and ADP scattering is consistent with a mobility of 240 $\rm cm^2V^{-1}s^{-1}$ for a sample with carrier concentration, 8.6×10^{16} $\rm cm^{-3}$ at 300 K, reported by Fonstad and Rediker [186] for single-crystal bulk SnO_2. The contribution of ID scattering increases at higher

carrier concentrations. If a constant dislocation density is assumed at all depths (the value measured for the surface of the thickest sample, $N_{\mathrm{dis}} = 8 \times 10^9\ \mathrm{cm}^{-2}$), the resultant mobility model curve (see the dashed curve in Fig. 6.10) clearly fails to reproduce the observed decreasing trend of mobility with carrier concentration. Therefore, the effect of the individual DDP scattering-limited mobility model curve, having taken into account the charged-dislocation variations with depth, is plotted representing the drastic mobility change with depth. In this respect, the functional, $N_{\mathrm{dis}}\left(d\left(n_{\mathrm{3D}}\right)\right)$, correlating the depth-dependent carrier concentration and dislocation density, has been substituted for N_{dis} in Eq. (3). The resulting model curve closely reproduces the data points, calculated by parallel conduction analysis using experimental results, emphasizing the need to include depth-dependent dislocation density as well as carrier concentration variations in transport studies of MBE-grown SnO_2/r-sapphire. Neutral impurity scattering was found to be negligible, and acoustic piezoelectric scattering was found to have only a minor effect on the carriers. This is reasonable given that the rutile SnO_2 lattice possesses an inversion symmetry and so does not show piezoelectricity; in cases where the ionic positions in a crystal are centres of inversion symmetry, the oscillation amplitude of the neighbouring ions are identical which results in no polarization field in the lattice.

In conditions where the CNL is well into the conduction band, as in InN, CdO, and SnO_2, the semiconductor tends to be n type as acceptor-type defects are less likely to form due to their higher formation energies. Nevertheless, it has been found that self-compensation in InN does take place even for the respective high formation energies [197]. Therefore, if there were some acceptor compensation in the SnO_2 samples (which we have assumed to be negligible), it would bring the model curve more towards the data points. Additionally, as the planar defects evidently have much lower abundance in the films and are limited to regions close to the interface, their scattering effect was not considered in the model. This would otherwise improve the model especially towards the high carrier density-tail which corresponds to scattering in the lower layers.

As can be seen in Fig. 6.10, at carrier concentrations below the Mott transition

level of SnO_2, polar optical mode scattering is the dominant mobility-limiting mechanism. Above this level, lattice and ionized defect scattering are all obscured by DDP scattering. Hence, the transport properties are essentially the same for either the singly or doubly charged states of the ionized defects. In highly lattice-mismatched heteroepitaxial materials with charged dislocations and/or grain boundaries, reduction in the screening length due to background doping affecting the mobility of carriers may also be depth dependent.

6.5 Summary and conclusions

In this chapter, the depth dependence of carrier concentration and mobility has been introduced for unintentionally doped heteroepitaxial SnO_2 films with different thicknesses grown on r-sapphire. The thickness of the films were determined by modelling the MIR-reflectance data taking into account the optical anisotropy of the SnO_2 films through XRD analysis. Simulation of the bulk mobility of the films with respect to their bulk carrier concentrations, directly obtained from the Hall effect measurements, appeared impossible. Cross-sectional TEM measurements showed that the dislocation density within the films vary significantly with distance from the interface, a similar trend that was observed for the bulk carrier concentration variations relative to the film thickness among the samples.

Plan-view TEM measurements indicated that the dislocation densities at the surface of the samples coincide with those at similar depths of the thicker samples obtained from cross-sectional measurements. This allowed for the parallel conduction analysis of the films which resulted in different carrier concentrations and mobilities for each layer within the samples. More samples with closer thicknesses would of course result in a more accurate determination of these values. The carrier concentrations of the different layers together with the exponential dislocation density variation with depth was used to determine the dislocation density variations with respect to carrier concentration indicating that the depth dependence of carrier concentration was due to the TDs in unintentionally doped MBE-grown SnO_2/r-sapphire. Additionally, it implied that dislocations are positively charged

and a source of donors as higher dislocation densities corresponded to higher carrier concentrations.

The significance of the dislocation density variations away from the interface towards the surface in respect of electron mobility has also been identified. Below the Mott transition level for SnO_2, $n = 10^{18}$ cm^{-3}, the scattering mechanisms were shown to be dominated by polar optical mode scattering. The lowering and steep downward trend of mobility toward the SnO_2/r-sapphire interface was well simulated by the dominant effect of DDP scattering as a function of carrier concentration. This observation strongly supports the need to undertake a layer-by-layer analysis and consider the variation of charged-dislocation density with depth in carrier mobility studies of highly lattice-mismatched heteroepitaxial semiconductors.

Chapter 7

Surface electronic properties of SnO_2 films grown by PAMBE

7.1 Introduction

In materials with symmetric crystal structures, the perfect periodicity is broken at the surface which this introduces surface states with complex Bloch wave vectors. This means that surface states are evanescent and localized within the surface layer of the material (they decay exponentially into the vacuum and into the bulk). The generation of surface states is similar at a metal/semiconductor interface at which the wavefunctions of the metal can tunnel into the semiconductor and form states in the band gap [198]. At a free semiconductor surface, donor (acceptor) defects and impurities are ionized when the respective surface states are unoccupied (occupied) which results in a downward (upward) band bending in case of carrier accumulation (see Fig. 2.2).

As semiconductor interfaces involving Schottky contacts and $p-n$ junctions play an integral role in optoelectronic devices, the existence of surface charged states and band bending become an important factor in designing microelectronic and optoelectronic devices. Among the III-V semiconductors, InAs [199] and InN [200] are known to have surface electron accumulation layers. Most binary oxides that have attracted intensive research into their optical and electronic properties, namely, In_2O_3 [201], CdO [202, 203], ZnO [203–205], and SnO_2 [206], all have been shown to have surface electron accumulation as the CNL in these materials lies above the CBM. Additionally, SnO_2 is well known as a gas sensing semiconductor for its surface conductivity variations upon gas exposure. However, very little is known about the electronic properties of surface layers in SnO_2 films, because until recently high quality thin films were not available. Nagata, *et al.* [206] have investigated the

surface band bending of unintentionally-, Sb-, and In-doped SnO_2 films using XPS measurements of the binding energy of the core Sn 3*d* electrons and found a downward band bending at the surface of the films. In this chapter, Hall effect, XPS and ECV techniques together with theoretical modelling of the bulk electronic structure and the Mott-Schottky layer have been adopted to quantitatively investigate the band bending and carrier concentration variations as a function of depth in UiD and Sb-doped SnO_2(101) films grown on *r*-sapphire by PAMBE.

7.2 Experimental techniques

In this study, the samples used were UiD and antimony (Sb)-doped SnO_2(101) films grown on *r*-sapphire as the substrate by plasma-assisted MBE (PAMBE). The Sn and maximum Sb source cell temperature was 1270° and 600°, respectively. Further description on the growth process can be found in chapter 6 and Ref. [183]. The UiD samples were grown in a range of thicknesses and were determined in chapter 6 to range between 26 and 1505 nm. The Sb-doped samples were grown at a fixed thickness of around 550 nm on a UiD film of thickness ∼480 nm as an intermediate layer. Secondary ion mass spectroscopy (SIMS) was used to determine the Sb concentration in the samples which ranged between 9.83×10^{17} and 2.82×10^{20} cm^{-3} [183]. MIR reflectance and Hall effect measurements were carried out to determine the thickness, carrier concentration, and mobility of the films. ECV and XPS measurements were performed to investigate the electronic properties at the surface of the SnO_2 films. The electrolyte used for the ECV measurements was $SnCl_2$ 1 molar diluted in deionised water. Detailed description of the ECV and XPS measurements are given in chapter 3.

7.3 IR reflectance, Hall effect and XPS measurements

To determine the carrier concentration of the Sb-doped samples, the reflectance spectra measured at an incident light angle of 56° were simulated for a 4-layer stratified medium (vacuum/SnO_2:Sb/SnO_2/sapphire) to acquire the thickness, *d*, of each film. This is shown in Fig. 7.1 for two selective samples. The carrier

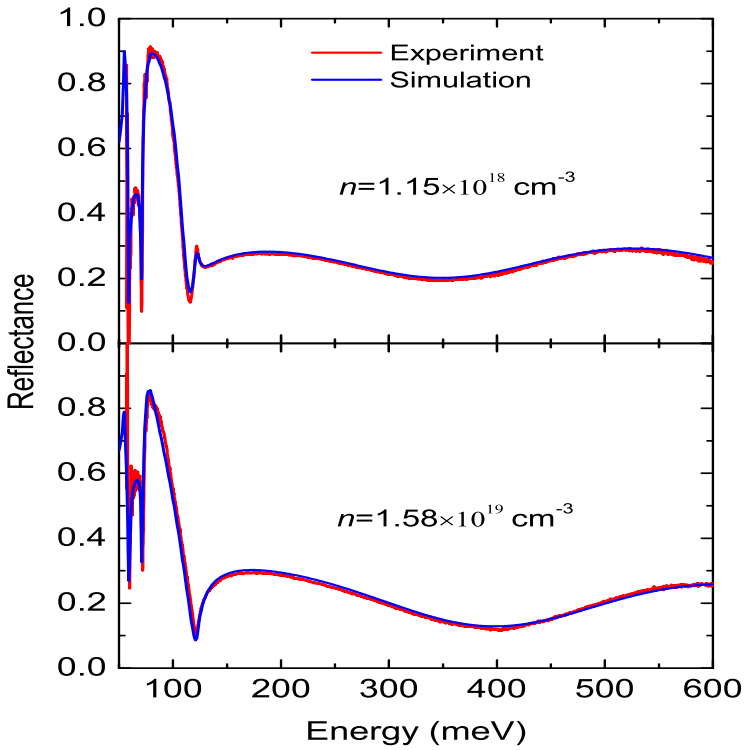

Figure 7.1: MIR reflectance data and simulation for two Sb-doped SnO_2 samples between 50 and 600 meV. The SnO_2 films have different Sb concentrations. $n = 1.15 \times 10^{18}$ and 1.58×10^{19} cm^{-3} correspond to Sb concentrations of $n_{Sb} = 9.83 \times 10^{17}$ and 2.08×10^{19} cm^{-3}, respectively.

concentration of the SnO_2:Sb samples, n, were calculated using the sheet carrier concentration, n_s, from the Hall effect measurements according to $n_b = n_s/d$. The values range between $n = 1.58 \times 10^{19}$ and $n = 2.6 \times 10^{19}$ cm^{-3}. The corresponding Sb-doping levels for each carrier concentration in given in table 7.1. The carrier concentrations of the UiD films with different thicknesses were obtained previously in chapter 6. As the thickness of the SnO_2:Sb films were determined to be ~550 nm and the Sb content is distributed homogeneously within the films, the carrier concentration is

Table 7.1: The electron and corresponding Sb concentrations for each sample, all having the same thickness.

Carrier concentration (cm^{-3})	Sb concentration (cm^{-3})
1.15×10^{18}	9.83×10^{17}
3.46×10^{18}	4.52×10^{18}
1.58×10^{19}	2.08×10^{19}
2.6×10^{19}	3.47×10^{19}

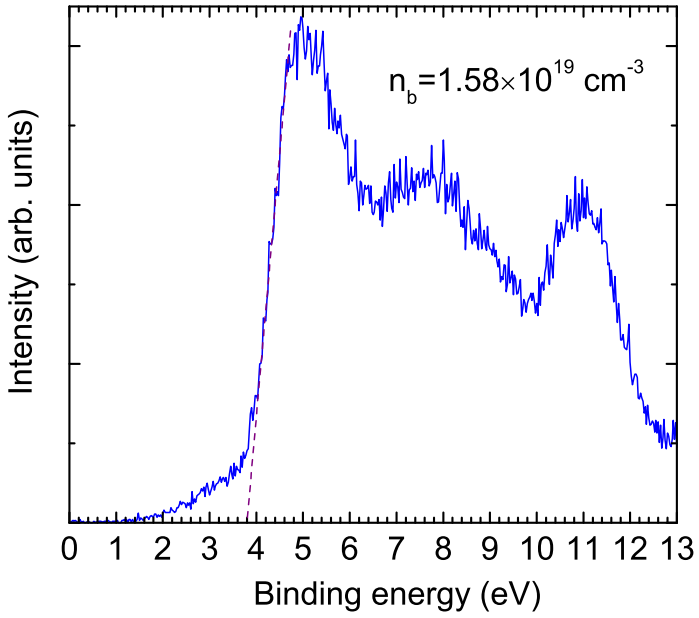

Figure 7.2: XPS valence band spectrum of a film with a bulk carrier concentration $n_{\mathrm{b}} = 1.58 \times 10^{19}$ cm^{-3}. The binding energy, V_{BE}, of the electrons at the VBM was determined to be 3.8 eV by the extrapolation of the sharp linear onset of the intensity.

taken as the bulk value, n_{b}.

XPS measurements were performed on the films to obtain the binding energy of the electrons at the VBM. A typical spectrum pertaining to a sample with $n_{\mathrm{b}} = 1.58 \times 10^{19}$ cm^{-3} is shown in Fig. 7.2. The binding energies were determined by the extrapolation of the sharp linear onset of the intensity. Carrier statistics calculations were performed within the 2-band $\boldsymbol{k}.\boldsymbol{p}$ model to obtain the bulk Fermi level, E_{F}, of the films. The surface band bending, V_{bb}, was evaluated using the equation:

$$V_{\mathrm{bb}} = V_{\mathrm{BE}} - E_{\mathrm{g}} \pm E_{\mathrm{F}}, \tag{7.1}$$

where, V_{BE} is the energy difference between the VBM and the Fermi level at the surface, E_{F} was calculated with respect to the CBM in the bulk, and the plus (minus) sign for the E_{F} corresponds to the E_{F} being below (above) the CBM. The values for both the UiD and Sb-doped samples is shown in table 7.2. Since the band bending is determined relative to the band extrema in the bulk, the negative sign signifies the accumulation of the electrons at the surface where there exists a downward band bending. Concerning the UiD samples, there is no uniform distribution of carrier

Table 7.2: Surface band bending, V_{bb} (eV), and corresponding bulk carrier concentration from the Hall effect measurements, n_b (cm^{-3}), of the UiD and Sb-doped SnO_2 films.

UiD SnO_2		Sb-doped SnO_2	
V_{bb}	n_b	V_{bb}	n_b
-0.263	3.06×10^{17}	-0.327	1.15×10^{18}
-0.258	3.78×10^{17}	-0.293	3.46×10^{18}
-0.231	1.02×10^{18}	-0.226	1.58×10^{19}
-0.220	1.45×10^{18}	-0.192	2.6×10^{19}
-0.206	2.36×10^{18}		

concentration for the regions below the surface layer towards the interface due to the depth-dependent charged-dislocation density discussed in chapter 6. This implies that a definite Fermi energy could not be calculated for the region below the surface layer. Hence, the modelling of the surface band bending and electron concentration as a function of depth was not feasible for the UiD SnO_2 films grown on r-sapphire. This issue is highlighted in table 7.2 by comparing the degree of band bending and the corresponding carrier concentration between the UiD and Sb-doped SnO_2 films in conjunction with Fig. 7.3 which illustrates the band bending variations with respect to the bulk Fermi level. The surface band bending is expected to decrease as the bulk carrier concentration increases which moves the bulk Fermi level closer to the CNL, but higher band bending is observed for the Sb-doped films that have the same carrier concentration as the UiD samples. For the Sb-doped film, the electron

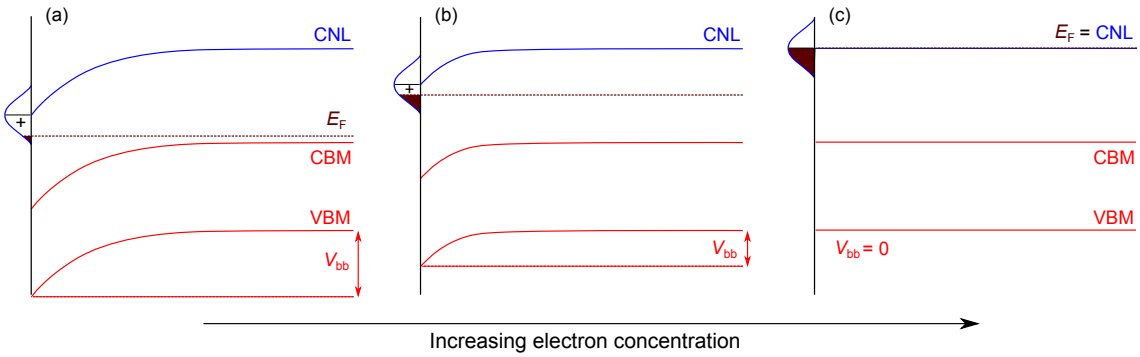

Figure 7.3: Schematic representation of the decrease in downward band bending, V_{bb}, as the bulk Fermi level moves up towards the CNL, (a) to (c). As the carrier concentration increases due to n-type doping of the bulk, a reduction in the density of unoccupied surface states is observed until the bulk and surface Fermi levels stabilize at the CNL (c).

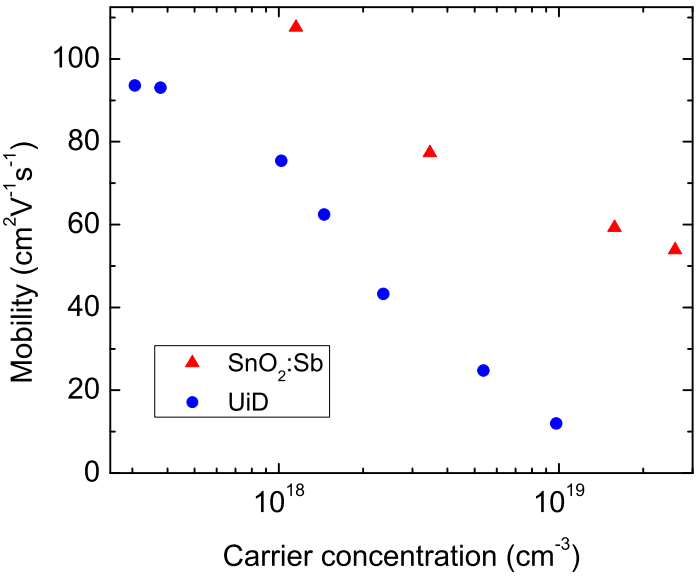

Figure 7.4: Comparison between the UiD and Sb-doped SnO_2 films in respect of carrier mobility as a function of carrier concentration. The UiD SnO_2 films were grown directly on *r*-sapphire which showed a high density of charged dislocations, while the Sb-doped films were grown on an intermediate UiD layer. It is apparent that the mobility of the Sb-doped films is much higher than in the UiD films in terms of carrier concentration. This clearly illustrates the significant reduction in dislocation scattering in the Sb-doped films.

concentration increases with Sb concentration indicating that Sb is a donor in SnO_2. As the Sb-doped SnO_2 films were grown on an intermediate layer of UiD SnO_2, the lattice mismatch has significantly decreased leading to a considerable reduction in the overall dislocation density. This is confirmed by a significant decrease in the dislocation scattering as compared with the UiD films in Fig. 7.4. Consequently, the main source of electrons are the Sb dopants which are distributed homogeneously throughout the films [183]. This implies that calculation of the bulk Fermi level is feasible for the Sb-doped SnO_2 films.

7.4 ECV measurements and space charge calculations

Potential variations at the surface of the SnO_2 films were studied through capacitance variations as a function of applied bias in a $SnO_2/SnCl_4$ electrochemical cell. As mentioned before, the major contribution to the overall capacity of this system comes from the capacity of the surface layer of the semiconducting film, thus making it possible to achieve the Mott-Schottky plots of the SnO_2 films. Fig-

ure 7.5 (a) shows the capacitance-voltage data in the form of Mott-Schottky plots ($1/C^2$ as a function of the applied bias) for four SnO_2:Sb films. The positive slope of the plots indicates the n-type character of the films. The magnitude of $1/C^2$ decreases with bulk carrier concentration of the films implying that the electron concentration at the surface increases with Sb concentration. The shallow gradient region at lower bias for each sample indicates the depletion of the surface electron accumulation, and the steeper region at higher bias is indicative of lower net space charge in the bulk.

The surface band bending and electron concentration as a function of depth were calculated through the modelling of the $C-V$ characteristics of the Mott-Schottky layer. Hence, the Poisson equation was solved assuming a negligible amount of acceptor defects or impurities:

$$\frac{d^2V}{dz^2} = -\frac{e}{\epsilon_s \epsilon_0}\left[N_D^+ - n(z)\right], \tag{7.2}$$

where the boundary conditions were applied according to the expressions 2.33 and 2.34. The band gap of SnO_2 was taken to be 3.5 eV [158, 161]. According to the optical and electronic anisotropy of SnO_2, the band edge effective mass and the dielectric constants were calculated via:

$$m_0^* = \left(m_{0,\perp}^{*2} m_{0,\parallel}^*\right)^{1/3}, \tag{7.3}$$

$$\epsilon = \frac{2\times\epsilon_\perp + \epsilon_\parallel}{3}. \tag{7.4}$$

$m_{0,\perp}^*$ ($0.3m_0$), $m_{0,\parallel}^*$ ($0.23m_0$) [193], $\epsilon_\perp(0)$ (13.5), and $\epsilon_\parallel(0)$ (9.58) [207] give an average band edge effective mass and static dielectric constant values of $0.27m_0$ and 12.2, respectively. Using the bulk Fermi level, obtained by carrier statistics calculations, and the degree of surface band bending described in the previous section, the Mott-Schottky plots of two samples with the lowest and highest bulk carrier concentrations were simulated as shown in Fig. 7.5 (b). The details of the simulation are briefly described in sections 2.2 and 3.3.1. Modelling of the Mott-Schottky curves enabled the calculation of the carrier concentration and band bending as a function of depth at the surface of the Sb-doped SnO_2 films. This is shown in Fig. 7.6 for the lowest

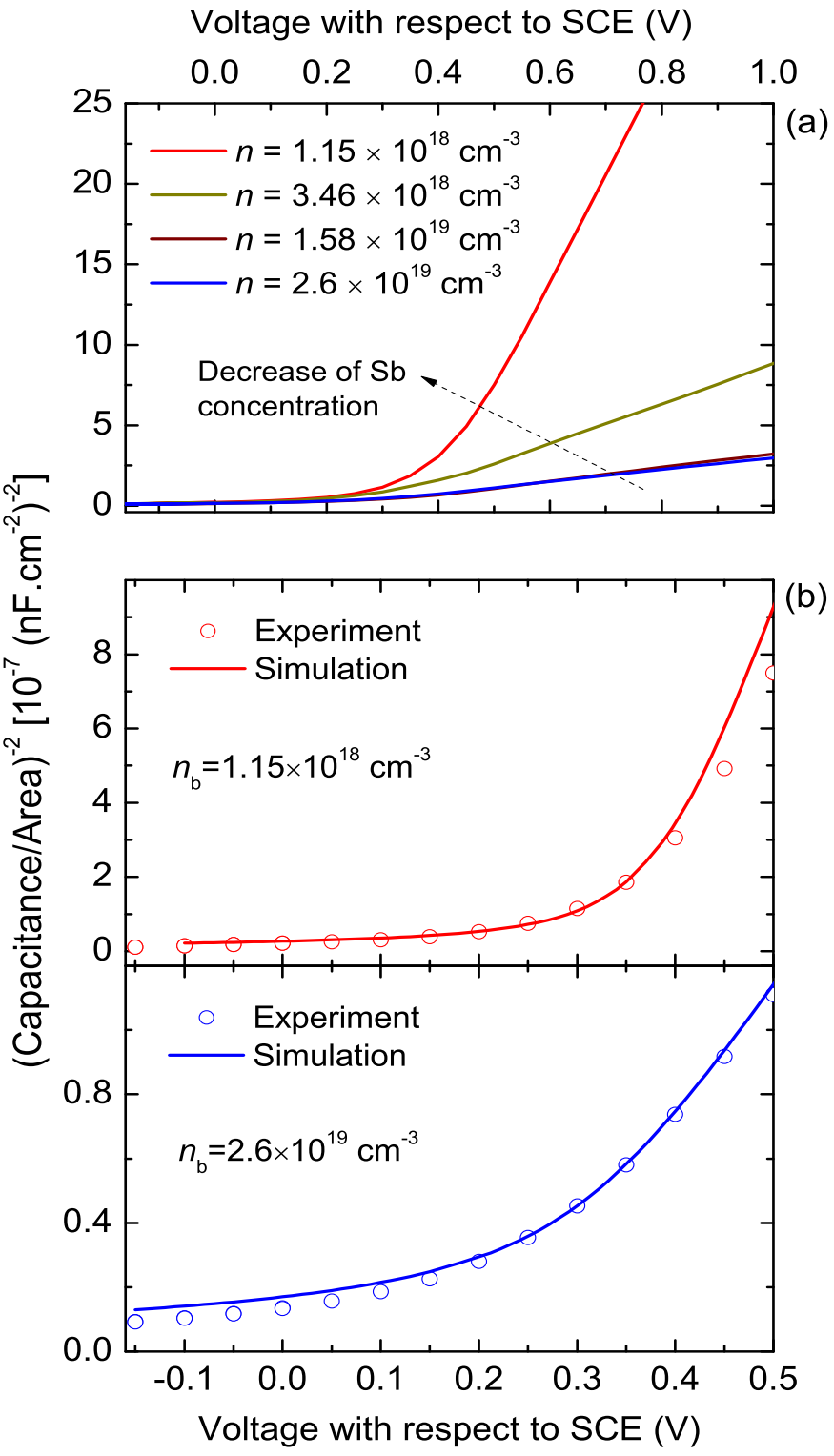

Figure 7.5: ECV data and simulation of the Mott-Schottky curves in SnO_2:Sb films. (a) Experimental data of the four investigated samples. The magnitude of $1/C^2$ decreases with bulk carrier concentration of the films implying that the electron concentration at the surface increases with Sb concentration. The shallow gradient region at lower bias for each sample indicates the depletion of the surface electron accumulation and the steeper region at higher bias is indicative of lower net space charge in the bulk. (b) shows the Mott-Schottky plots with respective simulations of the samples with the lowest and highest bulk carrier concentrations, respectively.

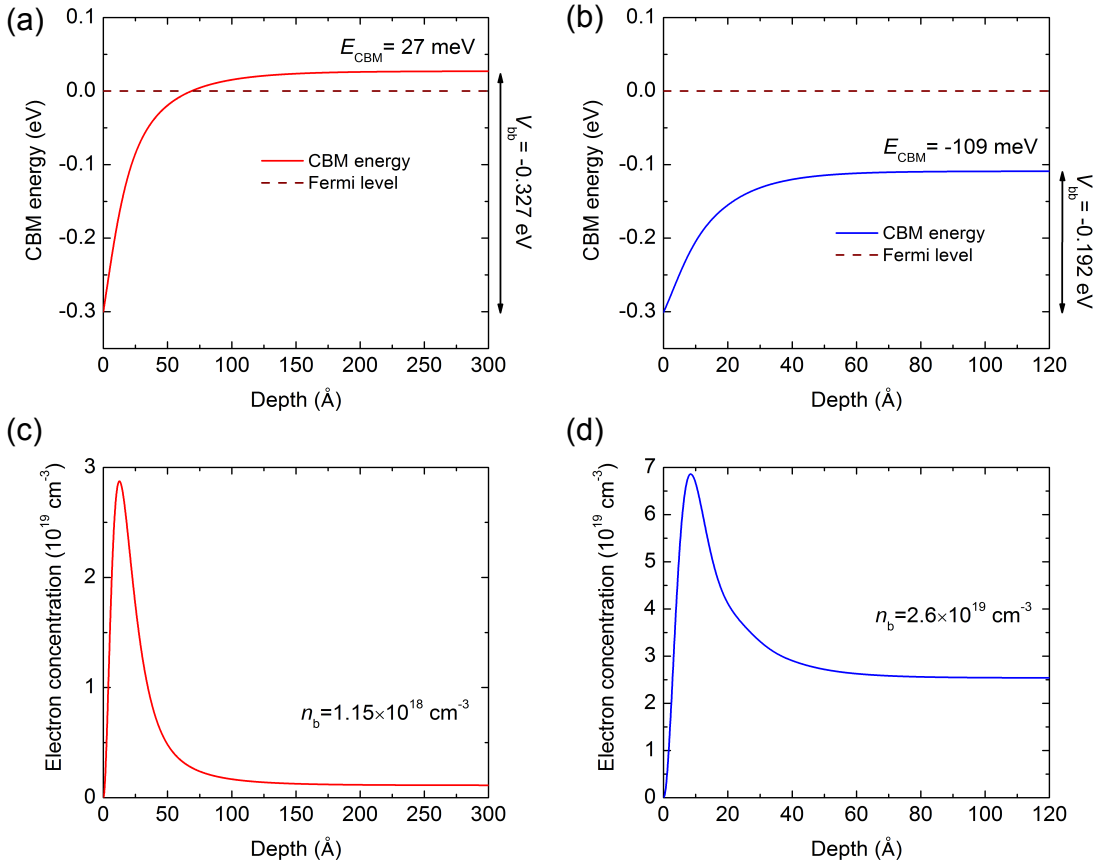

Figure 7.6: The calculated surface band bending, $V_{\rm bb}$, and electron concentration, n, as a function of depth for two SnO_2:Sb samples. (a) and (c) show the $V_{\rm bb}$ and n as a function of depth for the film with the lowest Sb concentration and $n_{\rm b} = 1.1\times10^{18}$ cm^{-3}; (b) and (d) show the corresponding plots for the film with the highest Sb concentration and $n_{\rm b} = 2.6\times10^{19}$ cm^{-3}. The reduction in the surface band bending along with the increase in the surface electron concentration is apparent as the bulk Fermi level moves to higher energies in the conduction band.

and highest Sb-doped SnO_2 films. The surface band bending in the film with a lower bulk electron concentration was larger and the corresponding Mott-Schottky layer wider compared to those of the film with a higher electron concentration [see Figs. 7.6(a) and (b)]. As can be seen in Fig. 7.6(a), the bulk Fermi level for the sample with the lowest Sb concentration, namely, 9.83×10^{17} cm^{-3}, lies in the band gap while an Sb concentration of 3.47×10^{19} cm^{-3} moves the bulk Fermi level up into the conduction band [see Fig. 7.6(b)]. In both conditions, electron accumulation at the surface of the films is apparent as the surface Fermi level lies in the conduction band. This is further demonstrated by Figs. 7.6(c) and (d).

7.5 Summary and conclusions

The surface electronic properties of $SnO_2(101)$ films grown on r-sapphire by PAMBE have been studied by Hall effect, XPS, and ECV measurements. XPS measurements were performed to determine the binding energies of the VB electrons. The Fermi level in the bulk region of the films was an input quantity for the determination of the surface band bending. As discussed in chapter 6, the UiD SnO_2 films contained a high density of charged dislocations originating at the interface and propogating towards the surface with varying density. Therefore, a constant bulk Fermi level could not calculated for the bulk region below the surface layer in these films.

As the SnO_2:Sb films were grown on an intermediate UiD SnO_2 layer, the lattice mismatch was considerably decreased resulting in a large reduction in the density of threading dislocations. Hence, the main source of donors in the films were the Sb dopants. Even distribution of Sb in the films allowed for the calculation of the bulk Fermi level. ECV measurements were performed to acquire the C–V spectra of the samples. The band bending and carrier concentration as a function of depth were obtained by space charge calculations in the Mott-Schottky layer. It was demonstrated quantitatively that SnO_2 films have downward band bending and surface electron accumulation. Both the surface band bending and the width of the accumulation region decrease with increasing Sb concentration. Among the investigated samples, the largest band bending was determined to be -0.327 eV for a film with Sb and bulk electron concentration of $n_{\mathrm{Sb}} = 9.83 \times 10^{17}$ and $n_{\mathrm{b}} = 1.1 \times 10^{18}$ cm^{-3}, respectively.

Chapter 8

Summary and general conclusions

The conduction band edge effective mass of electrons in CdO was determined using Hall effect, MIR reflectance, and optical absorption spectroscopy measurements. Optoelectronic quantities such as the plasmon energy and lifetime of several degenerate as-grown CdO samples were determined by the modelling of the reflectance data. Simulation of the plasmon energy and the optical gap as a function of electron concentration by carrier statistics calculations, considering the non-parabolicity of the conduction band, the Burstein-Moss shift, and band gap renormalisation, revealed the conduction band edge effective mass value of $0.24m_0$ at room temperature.

The conduction band edge effective mass was used to investigate the electron mobility in the CdO films at room temperature. The optical mobilities were obtained using the plasmon lifetimes as a function of electron concentration. The values ranged from ∼209 to 1116 $cm^2V^{-1}s^{-1}$ for carrier concentrations ranging between 2.5×10^{20} and 2.6×10^{19} cm^{-3}. The optical mobility showed a decreasing trend with increasing electron concentration. This was a result of the simultaneous increase in defects or impurities (possibly hydrogen) and electron concentration. Modelling of the optical mobility revealed the dominant effect of ionized defect/impurity scattering in degenerate CdO. However, optical mobility values were shown to be confined to the coherence length of the films. The transport mobility values measured by the Hall effect ranged between ∼20 and 124 $cm^2V^{-1}s^{-1}$ correspondingly which showed a significant decrease relative to the optical mobility values. The commonly used models of grain boundary scattering for simulation of the transport mobility were not applicable to CdO as they are all based on depletion layers at the grain boundaries. Surface electron accumulation in CdO implies that there should exist an electron accumulationn at the grain boundaries. Modelling of the transport mobility regarding

the intra-grain scattering revealed that ∼95% of the electrons get reflected at the grain boundaries. The analysis showed that grain boundary scattering is the prevailing scattering mechanism in electron transport in epitaxial CdO. Calculation of the conductivity showed that if the grain size of the CdO layers could be increased, electron transport would be significantly improved, leading to better conduction in transparent electrode applications.

Due to the degeneracy of CdO films, the exact fundamental band gap of this material was in a state of uncertainty. In chapter 5, variable temperature Hall effect, MIR reflectance and optical absorption have been utilized to determine the fundamental band gap of CdO at 0 K. The modelling of the experimental data was implemented by taking into account the band properties in chapter 4 plus the temperature and carrier concentration dependence of the fundamental band gap, band edge effective mass, high frequency dielectric constant and the Fermi level. Both the Varshni model and the model involving the Bose-Einstein statistics for phonon distribution have been used. The analysis revealed the fundamental band gap value of 2.31 eV at 0 K in the limit of zero carrier concentration. This value reduces significantly to 2.18 eV at room temperature. The associated Varshni parameters were determined to be $\alpha = 8 \times 10^{-4}$ eV/K and $\beta = 260$ K.

In chapter 6, the carrier mobility of epitaxial unintentionally-doped $SnO_2(101)$ grown on r-sapphire was investigated. Due to the large lattice mismatch of -11.3% between the SnO_2 films and the substrate, dislocations were observed by cross sectional TEM having an exponential increase towards the interface. Parallel conduction analysis revealed the positively-charged nature of dislocations in SnO_2. Modelling of the electron mobility in these undoped SnO_2 films was not possible without taking the positively-charged nature of dislocations into account and variations in the charge and dislocation density throughout the films. Hence, a layer-by-layer model was proposed to find out the dominant scattering mechanisms in the films. Longitudinal polar-optical scattering was the dominant scattering effect for carrier concentrations below the Mott transition level of SnO_2, namely, 1×10^{18} cm^{-3}, while the prevailing dislocation deformation potential scattering above that level ob-

scured all the other scattering mechanism including the polar-optical mode, ionized defects/impurity, and acoustic deformation potential scattering. Neutral impurity and piezoelectric scattering had minor effects on the electron mobility.

XPS studies on the surface electronic properties were undertaken towards the end of this work and hence a thorough qualitative analysis has yet to be performed on the series of SnO_2 films. In chapter 7, Hall effect measurements together with XPS and ECV characterisation were adopted to quantitatively investigate the electronic band structure and carrier concentration as a function of depth and composition at the surface of semiconducting SnO_2. In Sb-doped SnO_2 films, Sb atoms were distributed evenly throughout the films and were the main ionised donors. This is corroborated by comparing the electron mobilities between the unintentionally-doped and SnO_2:Sb films. The latter shows much higher mobility values as they had been grown on an intermediate unintentionally-doped layer by which the lattice mismatch has considerably reduced. Hence, a bulk region below the surface could be regarded for the SnO_2:Sb film. This allows for the determination of the bulk Fermi level which was used in the band bending calculations. By contrast, for the positively charged dislocation variations in the unintentionally-doped films (discussed in chapter 6) a bulk Fermi level could not be defined in these films. The discrepancy resulting from this issue is set out by comparing the respective band bending results with those of the Sb-doped films. Modelling of the Mott-Schottky plots for the SnO_2:Sb samples, obtained from the ECV measurements, revealed a downward band bending and surface electron accumulation in the films. A band bending of -0.327 eV was obtained for a film with the lowest Sb and bulk electron concentration of $n_{\mathrm{Sb}} = 9.83 \times 10^{17}$ and $n_{\mathrm{b}} = 1.1 \times 10^{18}$ cm^{-3}, respectively. The width of the surface layer and the band bending decreased with Sb doping levels.

Indium has shown to be a deep acceptor in SnO_2, thus, compensating the unintentionally-doped electrons. The mobility of the charge carriers as a function of carrier concentration and temperature will be investigated to find out why the mobility decreases with increasing In doping levels.

Since the theoretical values reported for the CNL of SnO_2 are not consistent,

e.g., 0.3 and 0.5 eV above the CBM, an experimental study is deemed necessary on high quality SnO_2 films. Hence, ion irradiation will be carried out to investigate the Fermi level stabilization in SnO_2 as well as the nature of energetically favourable native defects. However, measurements on some unintentionally doped samples irradiated by 1 MeV He particles showed a decrease in the sheet concentration and mobility of the films. Therefore, doping and/or self-ion implantation will be perfomed to investigate the CNL and intrinsic defects in SnO_2.

Bibliography

[1] A. Porch, D. V. Morgan, R. M. Perks, M. O. Jones, and P. P. Edwards, J. Appl. Phys. **95**, 4734 (2004).

[2] A. Porch, D. V. Morgan, R. M. Perks, M. O. Jones, and P. P. Edwards, J. Appl. Phys. **96**, 4211 (2004).

[3] A. N. Tiwari, G. Khrypunov, F. Kurdzesau, D. L. Bätzner, A. Romeo, and H. Zogg, Prog. Photovolt: Res. Appl. **12**, 33 (2004).

[4] G. S. Chae, Jpn. J. Appl. Phys. **40**, 1282 (2001).

[5] I. Chambouleyron and E. Saucedo, Sol. Energ. Mater. **1**, 299 (1979).

[6] V. K. Jain and A. P. Kulshreshtha, Sol. Energ. Mater. **4**, 151 (1981).

[7] C. M. Lampert, Sol. Energ. Mater. **6**, 1 (1981).

[8] G. Frank, E. Kauer, and H. Köstlin, Thin Solid Films **77**, 107 (1981).

[9] B. S. Tosun, R. K. Feist, S. A. Campbell, and E. S. Aydil, J. Vac. Sci. Technol. A **30**, 04D101 (2012).

[10] L. Dong, J. Hansen, P. Xu, M. L. Ackerman, S. D. Barber, J. K. Schoelz, D. Qi, and P. M. Thibado, Appl. Phys. Lett. **101**, 061601 (2012).

[11] S. Semancik and R. E. Cavicchi, Thin Solid Films **206**, 81 (1991).

[12] R. W. J. Scott, S. M. Yang, N. Coombs, G. A. Ozin, and D. E. Williams, Adv. Funct. Mater. **13**, 225 (2003).

[13] K. Durose, P. R. Edwards, and D. P. Halliday, J. Cryst. Growth **197**, 733 (1999).

[14] N. Romeo, A. Bosio, V. Canevari, and A. Podestà, Solar Energy **77**, 795 (2004).

[15] A. Gupta and A. D. Compaan, Appl. Phys. Lett. **85**, 684 (2004).

[16] K. Badeker, Ann. Phys. (Leipzig) **22**, 749 (1907).

[17] T. N. Theis and P. M. Solomon, Science **327**, 1600 (2010).

[18] K. Nomura, H. Ohta, K. Ueda, T. Kamiya, M. Hirano, and H. Hosono, Science **300**, 1269 (2003).

[19] A. P. Ramirez, Science **315**, 1377 (2007).

[20] J. Mannhart and D. G. Schlom, Science **327**, 1607 (2010).

[21] H. Takagi and H. Y. Hwang, Science **327**, 1601 (2010).

[22] D. C. Tsui, H. L. Stormer, and A. C. Gossard, Phys. Rev. Lett. **48**, 1559 (1982).

[23] A. Tsukazaki, A. Ohtomo, T. Kita, Y. Ohno, H. Ohno, and M. Kawasaki, Science **315**, 1388 (2007).

[24] A. Tsukazaki, S. Akasaka, K. Nakahara, Y. Ohno, H. Ohno, D. Maryenko, A. Ohtomo, and M. Kawasaki, Nature Mater. **9**, 889 (2010).

[25] A. Ohtomo and H. Y. Hwang, Nature (London) **427**, 423 (2004).

[26] S. Samson and C. G. Fonstad, J. Appl. Phys. **44**, 4618 (1973).

[27] A. Schleife, F. Fuchs, J. Furthmüller, and F. Bechstedt, Phys. Rev. B **73**, 245212 (2006).

[28] A. Janotti and C. G. Van de Walle, Phys. Rev. B **75**, 121201(R) (2007).

[29] A. Schleife, J. B. Varley, F. Fuchs, C. Rödl, F. Bechstedt, P. Rinke, A. Janotti, and C. G. Van de Walle, Phys. Rev. B **83**, 035116 (2011).

[30] E. Mollwo, Z. Phys. **138**, 478 (1954).

[31] D. G. Thomas and J. J. Lander, J. Chem. Phys. **25**, 1136 (1956).

[32] J. I. Pankove and N. M. Johnson, editors, *Hydrogen in Semiconductors, Semiconductors and Semimetals*, Academic Press, Boston, Vol. 34, 1991.

[33] L. Pavesi and P. Giannozzi, Phys. Rev. B **46**, 4621 (1992).

[34] C. G. Van de Walle, Phys. Rev. Lett. **85**, 1012 (2000).

[35] A. Janotti and C. G. Van de Walle, Nature Mater. **6**, 44 (2007).

[36] Çetin Kılıç and Alex Zunger, Appl. Phys. Lett. **81**, 73 (2002).

[37] S. F. J. Cox, E. A. Davis, S. P. Cottrell, P. J. C. King, J. S. Lord, J. M. Gil, H. V. Alberto, R. C. Vilão, J. P. Duarte, N. Ayres de Campos, A. Weidinger, R. L. Lichti, and S. J. C. Irvine, Phys. Rev. Lett. **86**, 2601 (2001).

[38] J. M. Gil, H. V. Alberto, R. C. Vilão, J. P. Duarte, N. Ayres de Campos, A. Weidinger, J. Krauser, E. A. Davis, S. P. Cottrell, and S. F. J. Cox, Phys. Rev. B **64**, 075205 (2001).

[39] D. M. Hofmann, A. Hofstaetter, F. Leiter, H. Zhou, F. Henecker, B. K. Meyer, S. B. Orlinskii, J. Schmidt, and P. G. Baranov, Phys. Rev. Lett. **88**, 045504 (2002).

[40] M. D. McCluskey, J. Appl. Phys. **87**, 3593 (2000).

[41] M. D. McCluskey, S. J. Jokela, K. K. Zhuravlev, P. J. Simpson, and K. G. Lynn, Appl. Phys. Lett. **81**, 3807 (2002).

[42] E. V. Lavrov, J. Weber, F. Börrnert, C. G. Van de Walle, and R. Helbig, Phys. Rev. B **66**, 165205 (2002).

[43] S. J. Jokela, M. D. McCluskey, and K. G. Lynn, Physica B **340-342**, 221 (2003).

[44] W. M. Hlaing Oo et al., Phys. Rev. B **82**, 193201 (2010).

[45] C. G. Van de Walle and J. Neugebauer, Nature **423**, 626 (2003).

[46] A. K. Singh, A. Janotti, M. Scheffler, and C. G. Van de Walle, Phys. Rev. Lett. **101**, 055502 (2008).

[47] M. Burbano, D. O. Scanlon, and G. W. Watson, J. Am. Chem. Soc. **133**, 15065 (2011).

[48] B. R. Nag, *Electron Transport in Compound Semiconductors*, Springer-Verlag, 1980.

[49] W. A. Harrison, Phys. Rev. **104**, 1281 (1956).

[50] M. Born and K. Huang, *Dynamical Theory of Crystal Lattices*, Oxford University Press, Oxford, 1988.

[51] P. Y. Yu and M. Cardona, *Fundamentals of Semiconductors*, Springer-Verlag, 1999.

[52] N. G. Weimann, L. F. Eastman, D. Doppalapudi, H. M. Ng, and T. D. Moustakas, J. Appl. Phys. **83**, 3656 (1998).

[53] D. C. Look and J. R. Sizelove, Phys. Rev. Lett. **82**, 1237 (1999).

[54] L. F. J. Piper, T. D. Veal, C. F. McConville, H. Lu, and W. J. Schaff, Appl. Phys. Lett. **88**, 252109 (2006).

[55] S. K. Vasheghani Farahani, T. D. Veal, A. M. Sanchez, O. Bierwagen, M. E. White, S. Gorfman, P. A. Thomas, J. S. Speck, and C. F. McConville, Phys. Rev. B **86**, 245315 (2012).

[56] B. K. Ridley, *Quantum Processes in Semiconductors*, Oxford University Press, 1993.

[57] E. O. Kane, J. Phys. Chem. Solids **1**, 249 (1957).

[58] N. W. Ashcroft and N. D. Mermin, *Solid State Physics*, Brooks/Cole, Cengage Learning, 1976.

[59] S. L. Chuang and C. S. Chang, Phys. Rev. B **54**, 2491 (1996).

[60] M. Suzuki and T. Uenoyama, Jpn. J. Appl. Phys. **35**, 543 (1996).

[61] D. K. Ferry, *Semiconductor Transport*, Taylor & Francis, 2000.

[62] K. F. Berggren and B. E. Sernelius, Phys. Rev. B **24**, 1971 (1981).

[63] W. Mönch, *Semiconductor Surfaces and Interfaces*, Springer-Verlag, 2001.

[64] G. Paasch and H. Übensee, Phys. Stat. Sol. B **113**, 165 (1982).

[65] J.-P. Zöllner, H. Übensee, G. Paasch, T. Fiedler, and G. Gobsch, Phys. Stat. Sol. B **134**, 837 (1986).

[66] H. Übensee, G. Paasch, and J.-P. Zöllner, Phys. Rev. B **39**, 1955 (1989).

[67] K. H. Rieder, M. Ishigame, and L. Genzel, Phys. Rev. B **6**, 3804 (1972).

[68] M. H. Brodsky, G. Lucovsky, M. F. Chen, and T. S. Plaskett, Phys. Rev. B **2**, 3303 (1970).

[69] A. Kasic, M. Schubert, S. Einfeldt, D. Hommel, and T. E. Tiwald, Phys. Rev. B **62**, 7365 (2000).

[70] M. Born and E. Wolf, *Principles of Optics*, Pergamon Press, 1975.

[71] C. C. Katsidis and D. I. Siapkas, Appl. Opt. **41**, 3978 (2002).

[72] T. S. Moss, *Optical Properties of Semi-Conductors*, Butterworths, 1961.

[73] J. I. Pankove, *Optical Processes in Semiconductors*, Dover Publications, 1971.

[74] A. M. Fox, *Optical Properties of Solids*, Oxford University Press, 2001.

[75] L. J. Van de Pauw, Philips Research Reports **13**, 1 (1958).

[76] P. Blood, Semicond. Sci. Technol. **1**, 7 (1986).

[77] P. J. Holmes, editor, *The Electrochemistry of Semiconductors*, Academic Press, 1962.

[78] T. Ambridge, C. R. Elliott, and M. M. Faktor, J. Appl. Electrochem. **3**, 1 (1973).

[79] T. Ambridge and M. M. Faktor, J. Appl. Electrochem. **4**, 135 (1974).

[80] A. J. Bard and L. R. Faulkner, *Electrochemical Methods: Fundamentals and Applications*, John Wiley & Sons, Inc., 2001.

[81] A. Yamashita, H. Araki, and T. Aoki, Jpn. J. Appl. Phys. **11**, 908 (1972).

[82] C. N. Berglund and W. E. Spicer, Phys. Rev. **136**, A1044 (1964).

[83] S. Hüfner, *Photoelectron Spectroscopy: Principles and Applications*, Springer, Berlin, 1995.

[84] S. Tanuma, C. J. Powell, and D. R. Penn, Surf. Interface Anal. **21**, 165 (1994).

[85] A. D. Capewell, *Novel Grading of Silicon Germanium for High Quality Virtual Substrates*, PhD thesis, University of Warwick, 2002.

[86] A. W. Agar, R. H. Alderson, and D. Chescoe, *Principles and practice of electron microscope operation*, Practical methods in electron microscopy, North-Holland Pub. Co., 1974.

[87] J. Zúñiga-Pérez, C. Munuera, C. Ocal, and V. Muñoz-Sanjosé, J. Cryst. Growth **271**, 223 (2004).

[88] J. E. Jaffe, R. Pandey, and A. B. Kunz, Phys. Rev. B **43**, 14030 (1991).

[89] K. Maschke and U. Rössler, Phys. Stat. Sol. **28**, 577 (1968).

[90] M. Altwein, H. Finkenrath, Č. Koňák, J. Stuke, and G. Zimmerer, Phys. Stat. Sol. **29**, 203 (1968).

[91] A. Breeze and P. Perkins, Solid State Commun. **13**, 1031 (1973).

[92] S. Tewari, Solid State Commun. **12**, 437 (1973).

[93] F. P. Koffyberg, Phys. Rev. B **13**, 4470 (1976).

[94] S. K. Vasheghani Farahani, T. D. Veal, P. D. C. King, J. Zúñiga-Pérez, V. Muñoz-Sanjosé, and C. F. McConville, J. Appl. Phys. **109**, 073712 (2011).

[95] F. P. Koffyberg, J. Sol. Stat. Chem. **2**, 176 (1970).

[96] D. T. Speaks, M. A. Mayer, K. M. Yu, S. S. Mao, E. E. Haller, and W. Walukiewicz, J. Appl. Phys. **107**, 113706 (2010).

[97] M. Yan, M. Lane, C. R. Kannewurf, and R. P. H. Chang, Appl. Phys. Lett. **78**, 2342 (2001).

[98] S. Ghosh, A. Sarkar, S. Chaudhuri, and A. Pal, Thin Solid Films **205**, 64 (1991).

[99] M. W. J. Prins, K.-O. Grosse-Holz, J. F. M. Cillessen, and L. F. Feiner, J. Appl. Phys. **83**, 888 (1998).

[100] D. H. Zhang and H. L. Ma, Appl. Phys. A **62**, 487 (1996).

[101] J. Bruneaux, H. Cachet, M. Froment, and A. Messad, Thin Solid Films **197**, 129 (1991).

[102] J. Y. W. Seto, J. Appl. Phys. **46**, 5247 (1975).

[103] P. D. C. King, T. D. Veal, P. H. Jefferson, J. Zúñiga-Pérez, V. Muñoz-Sanjosé, and C. F. McConville, Phys. Rev. B **79**, 035203 (2009).

[104] K. Fuchs, Mathematical Proceedings of the Cambridge Philosophical Society **34**, 100 (1938).

[105] E. H. Sondheimer, Adv. Phys. **50**, 499 (2001).

[106] A. F. Mayadas and M. Shatzkes, Phys. Rev. B **1**, 1382 (1970).

[107] J. Zúñiga-Pérez, *Crystal Growth and Characterization of II-VI Oxides Thin Films*, PhD thesis, University of Valencia, 2005.

[108] D. K. Bowen and B. K. Tanner, *High Resolution X-ray Diffractometry and Topography*, Taylor & Francis, London, 1998.

[109] A. Piqué, R. C. Y. Auyeung, S. B. Qadri, H. Kim, B. L. Justus, and A. L. Huston, Thin Solid Films **377-378**, 803 (2000).

[110] M. Schubert, T. E. Tiwald, and C. M. Herzinger, Phys. Rev. B **61**, 8187 (2000).

[111] H. Finkenrath, *Physics of II-VI and I-VII Compounds, Semi-Magnetic Semiconductors, Landolt-Börnstein: Numerical Data and Functional Relationships in Science and Technology. Group III: Crystal and Solid State Physics*, volume 17B, Springer, Berlin, 1982.

[112] S. G. Choi, J. Zúñiga-Pérez, V. Muñoz-Sanjosé, A. G. Norman, C. L. Perkins, and D. H. Levi, J. Vac. Sci. Technol. B **28**, 1120 (2010).

[113] G. Yu, N. L. Rowell, and D. J. Lockwood, J. Vac. Sci. Technol. A **22**, 1110 (2004).

[114] L. F. J. Piper, A. DeMasi, K. E. Smith, A. Schleife, F. Fuchs, F. Bechstedt, J. Zúñiga-Pérez, and V. Muñoz-Sanjosé, Phys. Rev. B **77**, 125204 (2008).

[115] P. H. Jefferson, S. A. Hatfield, T. D. Veal, P. D. C. King, C. F. McConville, J. Zúñiga-Pérez, and V. Muñoz-Sanjosé, Appl. Phys. Lett. **92**, 022101 (2008).

[116] H. Brooks, Phys. Rev. **83**, 879 (1951).

[117] H. Brooks, *Advances in Electronics and Electron Physics*, volume 7, Academic Press, New York, 1955.

[118] D. Chattopadhyay and H. J. Queisser, Rev. Mod. Phys. **53**, 745 (1981).

[119] D. C. Look, H. Lu, W. J. Schaff, J. Jasinski, and Z. Liliental-Weber, Appl. Phys. Lett. **80**, 258 (2002).

[120] J. Steinhauser, S. Faÿ, N. Oliveira, E. Vallat-Sauvain, and C. Ballif, Appl. Phys. Lett. **90**, 142107 (2007).

[121] T. D. Veal, C. F. McConville, and W. J. Schaff, editors, *Indium Nitride and Related Alloys*, CRC Press, Taylor & Francis, 2009.

[122] L. Hsu, R. E. Jones, S. X. Li, K. M. Yu, and W. Walukiewicz, J. Appl. Phys. **102**, 073705 (2007).

[123] T. L. Chu and S. S. Chu, J. Electron. Mater. **19**, 1003 (1990).

[124] Q. Zhou, Z. Ji, B. Hu, C. Chen, L. Zhao, and C. Wang, Mater. Lett. **61**, 531 (2007).

[125] G. Phatak and R. Lal, Thin Solid Films **209**, 240 (1992).

[126] K. Gurumurugan, D. Mangalaraj, and S. A. K. Narayandass, J. Electron. Mater. **25**, 765 (1996).

[127] Z. Zhao, D. L. Morel, and C. S. Ferekides, Thin Solid Films **413**, 203 (2002).

[128] T. K. Lakshmanan, J. Electrochem. Soc. **110**, 548 (1963).

[129] Y. Yang, S. Jin, J. E. Medvedeva, J. R. Ireland, A. W. Metz, J. Ni, M. C. Hersam, A. J. Freeman, and T. J. Marks, J. Am. Chem. Soc. **127**, 8796 (2005).

[130] R. Maity and K. K. Chattopadhyay, Sol. Energ. Mat. Sol. Cells **90**, 597 (2006).

[131] S. Jin, Y. Yang, J. E. Medvedeva, L. Wang, S. Li, N. Cortes, J. R. Ireland, A. W. Metz, J. Ni, M. C. Hersam, A. J. Freeman, and T. J. Marks, Chem. Mater. **20**, 220 (2008).

[132] J. Santos-Cruz, G. Torres-Delgado, R. Castanedo-Perez, C. I. Zúñiga-Romero, and O. Zelaya-Angel, Thin Solid Films **515**, 5381 (2007).

[133] P. K. Ghosh, R. Maity, and K. K. Chattopadhyay, Sol. Energy Mater. Sol. Cells **81**, 279 (2004).

[134] Y. Natsume and H. Sakata, Thin Solid Films **372**, 30 (2000).

[135] G. Xiong, J. Wilkinson, B. Mischuck, S. Tüzemen, K. B. Ucer, and R. T. Williams, Appl. Phys. Lett. **80**, 1195 (2002).

[136] G. Z. Xing, B. Yao, C. X. Cong, T. Yang, Y. P. Xie, B. H. Li, and D. Z. Shen, J. Alloy. Compd. **457**, 36 (2008).

[137] S. Noguchi and H. Sakata, J. Phys. D: Appl. Phys. **13**, 1129 (1980).

[138] K. M. Yu, M. A. Mayer, D. T. Speaks, H. He, R. Zhao, L. Hsu, S. S. Mao, E. E. Haller, and W. Walukiewicz, J. Appl. Phys. **111**, 123505 (2012).

[139] R. W. Wright and J. A. Bastin, Proc. Phys. Soc. **71**, 109 (1958).

[140] A. Wang, J. R. Babcock, N. L. Edleman, A. W. Metz, M. A. Lane, R. Asahi, V. P. Dravid, C. R. Kannewurf, A. J. Freeman, and T. J. Marks, PNAS **98**, 7113 (2001).

[141] N. Ueda, H. Maeda, H. Hosono, and H. Kawazoe, J. Appl. Phys. **84**, 6174 (1998).

[142] A. Segura, J. F. Sánchez-Royo, B. García-Domene, and G. Almonacid, Appl. Phys. Lett. **99**, 151907 (2011).

[143] I. N. Demchenko, J. D. Denlinger, M. Chernyshova, K. M. Yu, D. T. Speaks, P. Olalde-Velasco, O. Hemmers, W. Walukiewicz, A. Derkachova, and K. Lawniczak-Jablonska, Phys. Rev. B **82**, 075107 (2010).

[144] A. Janotti, D. Segev, and C. G. Van de Walle, Phys. Rev. B **74**, 045202 (2006).

[145] Y. P. Varshni, Physica **34**, 149 (1967).

[146] I. Vurgaftman, J. R. Meyer, and L. R. Ram-Mohan, J. Appl. Phys. **89**, 5815 (2001).

[147] K. P. O'Donnell and X. Chen, Appl. Phys. Lett. **58**, 2924 (1991).

[148] J. Bhosale, A. K. Ramdas, A. Burger, A. Muñoz, A. H. Romero, M. Cardona, R. Lauck, and R. K. Kremer, Phys. Rev. B **86**, 195208 (2012).

[149] M. E. White, M. Y. Tsai, F. Wu, and J. S. Speck, J. Vac. Sci. Technol. A **26**, 1300 (2008).

[150] T. Arai, J. Phys. Soc. Jpn **15**, 916 (1960).

[151] R. Summitt, J. A. Marley, and N. F. Borrelli, J. Phys. Chem. Solids **25**, 1465 (1964).

[152] W. Spence, J. Appl. Phys. **38**, 3767 (1967).

[153] M. Nagasawa and S. Shionoya, Solid State Commun. **7**, 1731 (1969).

[154] M. Nagasawa and S. Shionoya, Jpn. J. Appl. Phys. **10**, 727 (1971).

[155] R. J. Choudhary, S. B. Ogale, S. R. Shinde, V. N. Kulkarni, T. Venkatesan, K. S. Harshavardhan, M. Strikovski, and B. Hannoyer, Appl. Phys. Lett. **84**, 1483 (2004).

[156] F. J. Arlinghaus, J. Phys. Chem. Solids **35**, 931 (1974).

[157] A. Svane and E. Antoncik, J. Phys. Chem. Solids **48**, 171 (1987).

[158] D. Fröhlich, R. Kenklies, and R. Helbig, Phys. Rev. Lett. **41**, 1750 (1978).

[159] M. Nagasawa and S. Shionoya, Phys. Rev. Lett. **21**, 1070 (1968).

[160] M. Nagasawa and S. Shionoya, J. Phys. Soc. Jpn. **30**, 158 (1971).

[161] K. Reimann and M. Steube, Solid State Commun. **105**, 649 (1998).

[162] B. Höffling, A. Schleife, C. Rödl, and F. Bechstedt, Phys. Rev. B **85**, 035305 (2012).

[163] R. A. McKee, F. J. Walker, and M. F. Chisholm, Science **293**, 468 (2001).

[164] H. W. Jang, D. A. Felker, C. W. Bark, Y. Wang, M. K. Niranjan, C. T. Nelson, Y. Zhang, D. Su, C. M. Folkman, S. H. Baek, S. Lee, K. Janicka, Y. Zhu, X. Q. Pan, D. D. Fong, E. Y. Tsymbal, M. S. Rzchowski, and C. B. Eom, Science **331**, 886 (2011).

[165] J. G. Belk, J. L. Sudijono, X. M. Zhang, J. H. Neave, T. S. Jones, and B. A. Joyce, Phys. Rev. Lett. **78**, 475 (1997).

[166] A. Ohtake, M. Ozeki, and J. Nakamura, Phys. Rev. Lett. **84**, 4665 (2000).

[167] P. Vennéguès, Semicond. Sci. Technol. **27**, 024004 (2012).

[168] M. D. Craven, S. H. Lim, F. Wu, J. S. Speck, and S. P. DenBaars, phys. stat. sol. (a) **194**, 541 (2002).

[169] P. Gibart, Rep. Prog. Phys. **67**, 667 (2004).

[170] J. Jasinski and Z. Liliental-Weber, J. Electron. Mater. **31**, 429 (2002).

[171] A. Reiher, J. Bläsing, A. Dadgar, and A. Krost, Appl. Phys. Lett. **84**, 3537 (2004).

[172] V. Cimalla, V. Lebedev, F. M. Morales, R. Goldhahn, and O. Ambacher, Appl. Phys. Lett. **89**, 172109 (2006).

[173] P. D. C. King, T. D. Veal, and C. F. McConville, J. Phys.: Condens. Matter **21**, 174201 (2009).

[174] N. Miller, E. E. Haller, G. Koblmüller, C. Gallinat, J. S. Speck, W. J. Schaff, M. E. Hawkridge, K. M. Yu, and J. W. Ager, Phys. Rev. B **84**, 075315 (2011).

[175] O. Bierwagen, S. Choi, and J. S. Speck, Phys. Rev. B **84**, 235302 (2011).

[176] J. F. Wagner, Science **300**, 1245 (2003).

[177] E. R. Leite, I. T. Weber, E. Longo, and J. A. Varela, Adv. Mater. **12**, 965 (2000).

[178] A. Goetzberger and C. Hebling, Sol. Energy Mater. Sol. Cells **62**, 1 (2000).

[179] H. Kim, J. S. Horwitz, G. P. Kushto, Z. H. Kafafi, and D. B. Chrisey, Appl. Phys. Lett. **79**, 284 (2001).

[180] M. Batzill and U. Diebold, Prog. Surf. Sci. **79**, 47 (2005).

[181] N. F. Mott, Proc. Phys. Soc. **A62**, 416 (1949).

[182] N. F. Mott, Rev. Mod. Phys. **40**, 677 (1968).

[183] M. E. White, O. Bierwagen, M. Y. Tsai, and J. S. Speck, J. Appl. Phys. **106**, 093704 (2009).

[184] R. L. Petritz, Phys. Rev. **110**, 1254 (1958).

[185] R. E. Jones, K. M. Yu, S. X. Li, W. Walukiewicz, J. W. Ager, E. E. Haller, H. Lu, and W. J. Schaff, Phys. Rev. Lett. **96**, 125505 (2006).

[186] C. G. Fonstad and R. H. Rediker, J. Appl. Phys. **42**, 2911 (1971).

[187] H. T. Grahn, *Introduction to Semiconductor Physics*, World Scientific, 1999.

[188] J. A. Marley and R. C. Dockerty, Phys. Rev. **140**, A304 (1965).

[189] P. P. Debye and E. M. Conwell, Phys. Rev. **93**, 693 (1954).

[190] D. L. Dexter and F. Seitz, Phys. Rev. **86**, 964 (1952).

[191] D. M. Eagles, J. Phys. Chem. Solids **25**, 1243 (1964).

[192] Ç. Kılıç and A. Zunger, Phys. Rev. Lett. **88**, 095501 (2002).

[193] K. J. Button, C. G. Fonstad, and W. Dreybrodt, Phys. Rev. B **4**, 4539 (1971).

[194] J. Robertson and S. J. Clark, Phys. Rev. B **83**, 075205 (2011).

[195] H. M. Ng, D. Doppalapudi, T. D. Moustakas, N. G. Weimann, and L. F. Eastman, Appl. Phys. Lett. **73**, 821 (1998).

[196] M. W. Barsoum, E. N. Hoffman, R. D. Doherty, S. Gupta, and A. Zavaliangos, Phys. Rev. Lett. **93**, 206104 (2004).

[197] C. Rauch et al., Appl. Phys. Lett. **101**, 011903 (2012).

[198] V. Heine, Phys. Rev. **138**, A1689 (1965).

[199] L. F. J. Piper, T. D. Veal, M. J. Lowe, and C. F. McConville, Phys. Rev. B **73**, 195321 (2006).

[200] I. Mahboob, T. D. Veal, C. F. McConville, H. Lu, and W. J. Schaff, Phys. Rev. Lett. **92**, 036804 (2004).

[201] P. D. C. King, T. D. Veal, D. J. Payne, A. Bourlange, R. G. Egdell, and C. F. McConville, Phys. Rev. Lett. **101**, 116808 (2008).

[202] L. F. J. Piper, L. Colakerol, P. D. C. King, A. Schleife, J. Zúñiga-Pérez, Per-Anders Glans, T. Learmonth, A. Federov, T. D. Veal, F. Fuchs, V. Muñoz-Sanjosé, F. Bechstedt, C. F. McConville, and K. E. Smith, Phys. Rev. B **78**, 165127 (2008).

[203] A. Schleife, F. Fuchs, C. Rdl, J. Furthmller, and F. Bechstedt, Appl. Phys. Lett. **94**, 012104 (2009).

[204] D. Eger, A. Many, and Y. Goldstein, Surf. Sci. **58**, 18 (1976).

[205] M. W. Allen, C. H. Swartz, T. H. Myers, T. D. Veal, C. F. McConville, and S. M. Durbin, Phys. Rev. B **81**, 075211 (2010).

[206] T. Nagata, O. Bierwagen, M. E. White, M. Y. Tsai, Y. Yamashita, H. Yoshikawa, N. Ohashi, K. Kobayashi, T. Chikyow, and J. S. Speck, Appl. Phys. Lett. **98**, 232107 (2011).

[207] Z. M. Jarzebski and J. P. Marton, J. Electrochem. Soc. **123**, 333 (1976).